Ray-Tracing through the Millennium Simulation

Stefan Johannes Hilbert

München, 2007

Ray-Tracing through the Millennium Simulation

Stefan Johannes Hilbert

Dissertation
an der Fakultät für Physik
der Ludwig-Maximilians-Universität München

vorgelegt von
Stefan Johannes Hilbert
aus Strausberg

München, 18. Dezember 2007

Erstgutachter: Prof. Simon D. M. White Ph.D.
Zweitgutachter: apl. Prof. Dr. Gerhard Börner
Tag der mündlichen Prüfung: 2. April 2008

Diese Arbeit ist
meinen Großeltern und Eltern,
meinen Geschwistern
und insbesondere Annette
gewidment.

Contents

Zusammenfassung

In dieser Arbeit wird der Gravitationslinseneffekt im ΛCDM-Modell, dem derzeitigen Standardmodell der Kosmologie, untersucht. Hierzu wird die gravitative Ablenkung und Verzerrung von Lichtstrahlbündeln durch die kosmische Materieverteilung simuliert. Die Materieverteilung wird mit Hilfe der Millennium Simulation, einer N-Körper-Simulation der kosmischen Strukturbildung, erstellt. Die verwendete Ray-Tracing-Methode stellt eine erhebliche Weiterentwicklung früherer auf der Linsenebenen-Näherung basierender Ray-Tracing-Methoden dar.

Der starke Gravitationslinseneffekt wird anhand einer Monte-Carlo-Stichprobe von Lichtstrahlbündeln durch die Millennium Simulation untersucht. Insbesondere werden die Wahrscheinlichkeiten dafür berechnet, dass das Bild einer kleinen weit entfernten Lichtquelle stark vergrößert, stark verzerrt oder eines von mehreren Bildern einer Quelle ist. Aus der Stichprobe ergibt sich, dass diese Wahrscheinlichkeiten mit steigender Quellenrotverschiebung stark zunehmen. In fast allen Fällen werden die starken Gravitationslinseneffekte primär durch einzelne massereiche Objekte hervorgerufen. Eine Analyse der statistischen Verteilung der Massen und Rotverschiebungen dieser Gravitationslinsen zeigt, dass die untere Grenze des für starke Gravitationslinseneffekte relevanten Massenbereichs niedriger ist als in früheren Studien, welche auf Simulationen mit geringerer räumlicher Auflösung und Massenauflösung basieren. Außerdem wird der Einfluss von Materiestrukturen im Vorder- bzw. Hintergrund von Gravitationslinsen diskutiert. Zwar führen Lichtstrahlbündel, welche vom starken Gravitationslinseneffekt betroffen sind, im Mittel durch überdichte Regionen. Diese zusätzliche Materie trägt jedoch im Vergleich zur primären Linse nur wenig zur projizierten Massendichte bei.

Des Weiteren wird eingehend untersucht, inwieweit die stellare Materie in Galaxien den starken Gravitationslinseneffekt im ΛCDM-Modell beeinflusst. Dazu werden Gravitationslinseneffekte auf zwei verschiedene Arten simuliert. Die erste Variante berücksichtigt bei der kosmischen Materieverteilung nur die Dunkle Materie. Bei der zweiten Variante werden auch die Sterne in Galaxien mit einbezogen. Die Verteilung der Dunklen Materie wird direkt aus der Teilchenverteilung der Millennium Simulation erzeugt, während die Verteilung der stellaren Materie mit Hilfe von semi-analytischen Modellen zur Galaxienentstehung generiert wird. Es zeigt sich, dass die Berücksichtigung der sichtbare Materie zu wesentlich größeren optischen Tiefen für starke Gravitationslinseneffekte führt. Zum einen vergrößert die stellare Materie signifikant die Wirkungsquerschnitte von Gruppen- und Haufen-Halos. Zum anderen führt die Einbeziehung der stellaren Materie zu starken Gravitationslinseneffekten bei kleineren Halos, welche ohne die Sterne keine solchen Effekte hervorrufen würden. Selbst wenn nur Mehrfachbilder mit Abständen von mindestens zehn Bogensekunden berücksichtigt werden, kann die sichtbare Materie immer noch zu einer Verdopplung der optischen Tiefen führen.

Außerdem wird die Möglichkeit diskutiert, mit Hilfe zukünftiger Radioteleskope die kosmische Materieverteilung detailliert zu kartieren. Für eine Reihe idealisierter Beobachtungsprogramme werden große Karten der projizierten Massenverteilung mit den dafür zu erwartenden Werten für das Rauschen, die Auflösung und die Rotverschiebungsgewichtung simuliert. Es wird gezeigt, dass man mit einem ausreichend großen Radioteleskop die Gravitationslinseneffekte in Karten der 21-cm-Strahlung aus der Epoche der Reionisierung messen und damit ein extrem genaues Bild der kosmischen Massenverteilung erstellen könnte. In solchen Massenkarten könnte man die Dunklen Halos von Galaxien direkt beobachten, was zu einem wesentlich besseren Verständnis der Beziehung zwischen sichtbarer und Dunkler Materie beitragen würde. Diese Karten wären viel genauer als jene, welche aus den Bildverzerrungen entfernter Galaxien erstellt werden können.

Abstract

In this thesis, gravitational lensing in the concordance ΛCDM cosmology is investigated by carrying out ray-tracing along past light cones through the Millennium Simulation, a very large N-body simulation of cosmic structure formation. The method used for tracing light rays substantially extends previous ray-tracing methods that are based on the Multiple-Lens-Plane approximation.

Strong lensing is investigated by shooting random light rays through the Millennium Simulation. The probability is evaluated that an image of a small distant light source will be highly magnified, will be highly elongated or will be one of a set of multiple images. It is found that these probabilities increase strongly with increasing source redshift. It is shown that strong-lensing events can almost always be traced to a single dominant lensing object, and the mass and redshift distribution of these primary lenses is studied. The observed lens-mass range extends to lower masses than those found in earlier studies using simulations with lower spatial and mass resolution. Furthermore, effects of additional material along the line-of-sight are investigated. Although strong-lensing lines-of-sight are indeed biased towards higher than average mean densities, this additional matter typically contributes only a few percent of the total surface density.

The influence of stellar mass in galaxies on strong lensing is investigated by comparing the results obtained for lensing by dark matter alone to those obtained by also including the luminous matter. The dark-matter component of the lensing matter is constructed directly from the dark-matter particle distribution of the Millennium Simulation, while the luminous component is inferred from semi-analytic galaxy-formation models implemented within the evolving dark-matter distribution of the simulation. It is found that the inclusion of the stellar mass strongly enhances the probability for strong lensing compared to a 'dark-matter only' universe. The identification of the lenses associated with strong-lensing events reveals that the stellar mass of galaxies (i) significantly enhances the strong-lensing cross-sections of group and cluster halos, and (ii) gives rise to strong lensing in smaller halos, which would not produce noticeable effects in the absence of the stars. Even if only image splittings $\gtrsim 10\,\mathrm{arcsec}$ are considered, the luminous matter can still enhance the strong-lensing optical depths by up to a factor of two.

Finally, the potential capabilities of future radio telescopes for imaging the cosmic matter distribution are discussed. The Millennium Simulation is used to simulate large-area maps of the lensing convergence with the noise, resolution and redshift-weighting achievable with a variety of idealised surveys. It is shown that by observing lensing of 21-cm emission during reionization with a sufficiently large radio telescope, an image of the matter distribution could be obtained whose signal-to-noise far exceeds that of any map made using galaxy lensing. These mass images would allow the dark-matter halos of individual galaxies to be viewed directly, giving a wealth of statistical and morphological

information about the relative distributions of mass and light. For telescopes like the planned Square Kilometre Array, mass imaging may be possible near the resolution limit of the core array of the telescope.

1 Introduction

1.1 Gravitational lensing

Light is subject to gravity. Already Newton (1704) suspected that massive bodies could bend light rays by their gravitation.[1] However, this effect was first observed only two hundred years later when, during the solar eclipse of 1919, two expeditions measured the apparent positions of stars close to the solar limb (Dyson et al. 1920). These observations did not only confirm that the light of distant stars is indeed deflected by the gravitational field of the sun. They also revealed that the measured light-deflection angles were twice as large as predicted by Newtonian gravity (Cavendish ca. 1784; Soldner 1801) or early attempts at General Relativity (Einstein 1911), but in accordance with Einstein's 'full' General Theory of Relativity (Einstein 1915). Later, Fomalont and Sramek (1976) could measure the gravitational light deflection by the sun with much higher accuracy using radio interferometry, which imposed strong constraints on possible deviations from General Relativity on solar-system scales.

Perhaps due to Logdge (1919),[2] the diverse phenomena related to gravitational light deflection have become known as 'gravitational lensing' in astronomy.[3] Observations of gravitational light deflection by the sun have the advantage that one can measure the deflection by observing the apparent position of the light source in presence *and* in absence of the deflector.[4] In general, this is not possible for deflectors outside the solar system. However, the light deflection angle varies strongly across a field of view that contains a sufficiently compact and massive object as deflector. As a result, highly magnified or strongly distorted images of distant sources might be observed, and even multiple images of the same source may occur. Such phenomena are referred to as '*strong* gravitational lensing'. Soon after 1919, scientist became interested in strong lensing of stars by stars (Eddington 1920; Chwolson 1924; Einstein 1936). Zwicky (1937a,b) considered strong lensing of galaxies by galaxies and galaxy clusters, and concluded that such events would (i) provide further tests for General Relativity, (ii) allow one to see galaxies at larger distance due to the magnification effect, and (iii) provide a mass estimate for the galaxy or cluster acting as lens. Later, Klimov (1963), Liebes (1964), and Refsdal (1964b,a) reopened the subject. Refsdal (1964a) pointed out the possibility

[1] A short historical review on the science of gravitational light deflection can be found in the textbook on Gravitational Lenses by Schneider et al. (1992).

[2] who opined that the sun's gravitational field does *not* act like a lens

[3] See Schneider et al. (2006) for a recent review on gravitational lensing.

[4] The image position of the source is determined from two different positions in the earth's orbit around the sun.

to use the time delay between multiple images of a variable source for a determination of the Hubble constant.

Strong lensing was first observed by the discovery of quasars that were multiply imaged by a massive galaxy in the foreground (Walsh et al. 1979; Weymann et al. 1980). Today, a growing number of multiply imaged quasars has been discovered thanks to large surveys (see, e.g., Inada et al. 2008). Very elongated and curved images of galaxies, so-called giant arcs, were first discovered by Lynds and Petrosian (1986) and Soucail et al. (1987) in galaxy clusters. Today giant arcs and multiply imaged galaxies have been observed in the centres of many rich galaxy clusters. Prominent examples are the clusters Abell 1689 (Broadhurst et al. 2005) and Abell 2218 (Kneib et al. 1996). Highly distorted images of radio sources were first discovered by Hewitt et al. (1988) and Langston et al. (1989). Several galaxies at high redshift have been discovered thanks to the magnifying effect of massive galaxy clusters (e.g. Franx et al. 1997; Egami et al. 2005).

Objects with masses much smaller than galaxies, e.g. single stars, cannot produce multiple images that are apart far enough to be resolved in observations. Such objects can, however, noticeably change the image magnification when passing close to the line-of-sight to the source. This '*micro*lensing' (Chang and Refsdal 1979, 1984; Gott 1981; Young 1981; Nityananda and Ostriker 1984; Paczynski 1986a,b; Kayser et al. 1986; Schneider and Weiss 1987; Mao and Paczynski 1991) was first detected through uncorrelated brightness variations in the images of a quasar that is strongly lensed by a galaxy (Irwin et al. 1989; Vanderriest et al. 1989). Microlensing of stars in nearby galaxies has been used to constrain the abundance of compact massive objects in the Galactic halo (Tisserand et al. 2007). Several extrasolar planets have been detected so far by microlensing of stars in our Galaxy (Bond et al. 2004; Udalski et al. 2005; Beaulieu et al. 2006; Gould et al. 2006; Gaudi 2007).

Most light sources seen on our sky are not affected by strong lensing. However, the gravitational light deflection by matter inhomogeneities induces small distortions in practically all images of distant light sources. This is called '*weak* gravitational lensing'. Early works (Zel'Dovich 1964a; Dashevskii and Zel'Dovich 1964; Dashevskii and Slysh 1965; Gunn 1967a,b; Kantowski 1969; Dyer and Roeder 1972, 1973, 1974) considered effects on the determination of cosmological distances. Weak lensing introduces an additional scatter in the apparent size and magnitude of sources that are used as standard rods or standard candles, e.g. type-Ia supernovae (Riess et al. 1998; Perlmutter et al. 1999; Riess et al. 2004; Barris et al. 2004). Moreover, if distant sources are observed mainly through underdense foregrounds, they appear smaller and dimmer on average than predicted from a simple cosmological model without matter inhomogeneities. These effects are small compared to other uncertainties for current supernova samples (Wambsganss et al. 1997; Holz 1998; Riess et al. 1998; Valageas 2000; Amanullah et al. 2003; Knop et al. 2003; Barris et al. 2004; Riess et al. 2004; Hilbert et al. 2007b), but they may be significant in future supernova surveys that yield larger samples and probe higher redshifts (Dodelson and Vallinotto 2006; Munshi and Valageas 2006).

The image distortions induced by matter inhomogeneities between source and observer may be too small to be seen in individual images, but if the distortions are coherent on sufficiently large angular scales, they can be detected statistically by 'averaging' the image shapes over small patches of the sky. The weak distortion was first detected by

Tyson et al. (1990) in the images of distant faint blue galaxies around clusters. Due to improvements in observational equipment and data analysis (Blandford et al. 1991; Kaiser and Squires 1993; Kaiser et al. 1995), weak lensing could be detected around ensembles of galaxies (Brainerd et al. 1996). Later, even the weak lensing effects of the large-scale matter distribution, known as 'cosmic shear', have been detected (Bacon et al. 2000; Kaiser et al. 2000; Van Waerbeke et al. 2000; Wittman et al. 2000).

As mentioned above, strong and weak gravitational lensing can be used in various ways to study astronomical objects and our Universe. Relative time-delay measurements between multiple images of strongly lensed variable sources can be used to constrain the Hubble constant. As a 'natural telescope', strong lensing can assist the observation of objects at very high redshift. Furthermore, lensing can be used to constrain the matter distribution in galaxies, clusters, and the large-scale structure. If gravitational light deflection is correctly described by General Relativity, the light deflection depends only on the mass distribution of the deflecting matter, but not on its internal state or composition. This property constitutes a great advantage over other methods of mass determination that are based on, e.g., the velocity dispersion of internal components, X-ray emission, or assumed mass-to-light ratios (Voit 2005).

1.2 Constraining the cosmology with gravitational lensing

When Hubble (1929) noticed that galaxies move apart on large scales, it became apparent that our Universe is expanding. Since Zwicky (1933) realised that unseen material is needed to explain the dynamics of galaxy clusters, many observations have indicated that most matter in our Universe is in some form of dark matter. When Riess et al. (1998) and Perlmutter et al. (1999) found evidence for an accelerated expansion of the Universe in the brightness of distant supernovae, the idea gained general acceptance that there is a cosmological constant or some other form of 'dark energy' that drives the acceleration. The now widely accepted model of cosmic structure formation is based on cold dark matter (CDM) and a cosmological constant (Λ).[5] This ΛCDM model provides a consistent explanation for a wide variety of observations of galaxies, galaxy clusters and galaxy clustering, of the structure of the intergalactic medium, of the brightness of distant supernovae, of the abundance of light elements, and, most notably, of the temperature fluctuations in the cosmic microwave background.

The parameters of the ΛCDM model are already highly constrained by these observations (Spergel et al. 2007). Further tests and constraints of this concordance model are provided by measurements of gravitational-lensing effects. Today, numerical simulations of the cosmic structure formation provide detailed predictions about the matter distribution in a ΛCDM universe (Springel et al. 2006). Many recent observations of the gravitational-lensing effects around galaxies (Hoekstra et al. 2002; Seljak et al. 2005; Mandelbaum et al. 2006b; Simon et al. 2007), as well as in and around galaxy clusters (Bradač et al. 2005; Clowe et al. 2006; Comerford et al. 2006; Mandelbaum et al. 2006a; Natarajan et al. 2007; Limousin et al. 2007) are well explained by the dark-matter structures predicted from the simulations. Large surveys measuring the weak lensing effects

[5] See Springel et al. (2006) for a recent review.

of the matter distribution as a whole (e.g. Hoekstra et al. 2006; Semboloni et al. 2006; Benjamin et al. 2007; Hetterscheidt et al. 2007; Massey et al. 2007b; Simon et al. 2007) are very promising for further constraining the model parameters.

There are, however, some observations whose compatibility with the ΛCDM model has been doubted. For example, the flux ratios between the multiple images of many strongly lensed sources may indicate a larger amount of substructure in lens-galaxy halos than that found in numerical simulations (Mao and Schneider 1998; Dalal and Kochanek 2002; Metcalf and Zhao 2002; Keeton 2003; Evans and Witt 2003; Bradač et al. 2004; Amara et al. 2006; Macciò et al. 2006; Sugai et al. 2007). Another unsolved question is whether the observed frequency of giant arcs (Luppino et al. 1999; Zaritsky and Gonzalez 2003; Gladders et al. 2003) is consistent with predictions based on the ΛCDM model with parameters favoured by other observations (Bartelmann et al. 1998; Meneghetti et al. 2000, 2005, 2007; Oguri et al. 2003; Dalal et al. 2004; Wambsganss et al. 2004; Horesh et al. 2005; Li et al. 2005, 2006; Wu and Chiueh 2006). It is unclear, in how far these discrepancies are real evidence for shortcomings of the ΛCDM model, and what must be attributed to deficiencies in the methods that were employed for the observations and predictions.

1.3 Ray-tracing through the Millennium Simulation

Substantial efforts are currently underway to improve the measurements of gravitational-lensing effects. The observational improvements need to be matched by a comparable improvement in the theoretical predictions. Early predictions for the lensing properties of the ΛCDM model were based on analytic models for nonlinear structure (e.g. Vietri and Ostriker 1983; Turner et al. 1984; Subramanian et al. 1987; Narayan and White 1988; Blandford et al. 1991). As was recognised later, reliable predictions require numerical simulation (Bartelmann et al. 1998; Jain et al. 2000). The now commonly used approach, ray-tracing through numerical simulations of structure formation, consists of several steps (see, e.g., Bartelmann and Weiss 1994; Jain et al. 2000; Vale and White 2003; Wambsganss et al. 2004; Li et al. 2005). In a first step, the (nonlinear) structure formation in a region of the model universe is simulated numerically (for simulation techniques, see, e.g., Bertschinger 1998; Frenk et al. 1999; Springel 2005; Norman et al. 2007, and references therein). Depending on the scope of the study, the simulated region may contain a galaxy, a cluster, or a very large cosmological volume. In a second step, the matter structure that has formed in the simulation is projected onto one or several 'lens planes'. Using the (multiple-)lens-plane approximation (Bourassa and Kantowski 1975; Blandford and Narayan 1986; Schneider et al. 1992), virtual light rays are traced from an observer through the lens plane(s) back to their source at a given redshift. The information of the light rays is then used to calculate the image properties. In a final step, the calculated properties are subjected to a statistical analysis.

The accuracy of the ray-tracing method depends critically on the quality of the underlying structure-formation simulation. Currently, the largest high-resolution simulation available is the Millennium Simulation (Springel et al. 2005). This N-body simulation

was carried out by the Virgo Consortium[6] on 512 processors of an IBM p690 parallel computer at the Max-Planck-Rechenzentrum in Garching, Germany, with a customised parallel TreePM (Xu 1995) version of GADGET-2 (Springel 2005). The simulation follows the matter evolution in a cubic region of 685 Mpc side length within the ΛCDM cosmology from redshift $z = 127$ to the present. Due to its large volume and high resolution, the simulation provides excellent statistical predictions for the matter distribution on scales ranging from individual dark-matter halos of galaxies to galaxy clusters and the large-scale structure. The Millennium Simulation has been used as basis for various studies of, e.g., the formation and evolution of galaxies, their central black holes, and their dark-matter environment (Gao et al. 2005; Croton et al. 2006; De Lucia et al. 2006; De Lucia and Blaizot 2007).

In this PhD thesis, I investigate gravitational lensing in the concordance ΛCDM cosmology by carrying out ray-tracing through the Millennium Simulation. In order to take full advantage of the large volume and the excellent spatial and mass resolution of the simulation, I developed a flexible, parallel, I/O-optimised ray-tracing code, which substantially extends previous light-ray-tracing methods based on the multiple-lens-plane approach. This ray-tracing code is suitable for simulating strong and weak lensing. In addition to the dark matter, the ray-tracing code takes into account the luminous matter in galaxies as inferred from semi-analytic galaxy-formation models implemented within the evolving dark-matter distribution of the simulation (e.g. De Lucia and Blaizot 2007). Furthermore, the morphology and luminosity information of the galaxies can be added to simulate galaxy lensing surveys with given selection functions.

In Chapter 2, gravitational lensing is investigated by shooting random light rays through the Millennium Simulation. First, the method for tracing representative light rays through the simulation is briefly described. Then, results for the magnification distribution and strong-lensing optical depths as a function of source redshift are discussed. It is shown that strong lensing events are almost always caused by a single dominant lensing object, and the mass and redshift distribution of these primary lenses are studied. Furthermore, the effect of material in front of or behind the primary lens is investigated.

The methods discussed in Chapter 2 are extended in Chapter 3 to investigate the influence of stellar mass in galaxies on strong lensing. The results obtained for lensing by dark matter alone are compared to those obtained by also including the stellar mass components predicted from the galaxy-formation models of De Lucia and Blaizot (2007). The stellar mass is much more concentrated than the dark matter and therefore leads to higher masses in the very centres of galaxies. Thus the stellar mass gives rise to strong lensing near the centres of many galaxies, which greatly enhances the probability for strong lensing compared to a 'dark matter only' universe. Strong lensing at larger distance from the centres of galaxies (corresponding to image splittings >10 arcseconds) is, however, not significantly affected by the stellar mass.

In Chapter 4, the potential capabilities of future radio telescopes for imaging the cosmic matter distribution are discussed. Ray-tracing through the Millennium Simulation is used to simulate large-area maps of the lensing convergence with the noise, resolution, and redshift-weighting achievable with a variety of idealised observation programmes. It

[6] a collaboration of British, German, Canadian, and US astrophysicists (see http://www.virgo.dur.ac.uk)

is shown that by observing lensing of 21-cm emission during reionization with a sufficiently large radio telescope, an image of the matter distribution could be obtained that allows the dark-matter halos of individual galaxies to be viewed directly, giving a wealth of statistical and morphological information about the relative distributions of mass and light. For telescopes like the planned Square Kilometre Array, mass imaging may be possible with comparable resolution, but much higher signal-to-noise ratio than could be obtained by galaxy lensing.

A summary of the work presented in this thesis together with suggestions for possible future research is given in Chapter 5.

The work discussed in Chapters 2-4 has been or will be published as regular articles in a peer-reviewed journal. The article reference is given at the beginning of each chapter. These chapters closely follow the language style and structure of the corresponding article as closely as possible.

2 Strong-lensing optical depths in a ΛCDM universe

Stefan Hilbert, Simon D.M. White, Jan Hartlap, and Peter Schneider, 2007: MNRAS, 382, 121

Abstract

We investigate strong gravitational lensing in the concordance ΛCDM cosmology by carrying out ray-tracing along past light cones through the Millennium Simulation, the largest simulation of cosmic structure formation ever carried out. We extend previous ray-tracing methods in order to take full advantage of the large volume and the excellent spatial and mass resolution of the simulation. As a function of source redshift we evaluate the probability that an image will be highly magnified, will be highly elongated or will be one of a set of multiple images. We show that such strong-lensing events can almost always be traced to a single dominant lensing object and we study the mass and redshift distribution of these primary lenses. We fit analytic models to the simulated dark halos in order to study how our optical depth measurements are affected by the limited resolution of the simulation and of the lensing planes that we construct from it. We conclude that such effects lead us to underestimate total strong-lensing cross-sections by about 15%. This is smaller than the effects expected from our neglect of the baryonic components of galaxies. Finally we investigate whether strong lensing is enhanced by material in front of or behind the primary lens. Although strong lensing lines-of-sight are indeed biased towards higher than average mean densities, this additional matter typically contributes only a few percent of the total surface density.

Key words: gravitational lensing – dark matter – large-scale structure of the Universe – cosmology: theory – methods: numerical

2.1 Introduction

Gravitational lensing was first discovered through strong lensing effects which can produce multiple images of distant quasars (Walsh et al. 1979) and highly distorted images of distant extended objects such as galaxies (Lynds and Petrosian 1986; Soucail et al. 1987) and radio sources (Hewitt et al. 1988). Such effects occur when the surface mass density of an individual object (the 'lens') is comparable to that across the Universe as a whole, and as a result they are generated only by the most massive and most concentrated structures. In contrast, weak lensing, detected through the small but coherent distortion of the images of distant galaxies in the same direction on the sky (Tyson et al. 1990), is sensitive to the abundance and structure of typical nonlinear objects, so-called

dark matter halos, and is now beginning to measure the statistics of the cosmic mass distribution also in the quasilinear regime (Semboloni et al. 2006; Hoekstra et al. 2006; Hetterscheidt et al. 2007; Massey et al. 2007b). Thus gravitational lensing complements microwave background, large-scale structure, and Lyα forest studies, which provide information primarily in the quasilinear and linear regimes (for recent reviews on strong and weak lensing, see Kochanek 2006; Schneider 2006b). Combining all these measures to constrain theories for the origin of structure requires a reliable model for the nonlinear phases of evolution.

The current standard model of cosmological structure formation is based on cold dark matter and a cosmological constant. This ΛCDM model has been shown to fit a wide variety of observations of galaxies and their dark halos, of galaxy clusters and galaxy clustering, of the structure of the intergalactic medium out to redshift 6, and, most notably, of the detailed pattern of temperature fluctuations in the cosmic microwave background. The parameters of the model are already highly constrained (Spergel et al. 2007). Early predictions for its lensing properties were based on analytic models for nonlinear structure (e.g. Turner et al. 1984; Subramanian et al. 1987; Narayan and White 1988), but reliable predictions require numerical simulation (e.g. Bartelmann et al. 1998; Jain et al. 2000; Wambsganss et al. 2004). Recent gravitational lensing work has confirmed the dark halo structure predicted by these simulations for galaxies (Hoekstra et al. 2002; Seljak et al. 2005; Mandelbaum et al. 2006b; Simon et al. 2007) and clusters (Comerford et al. 2006; Mandelbaum et al. 2006a; Natarajan et al. 2007) as well as for the ensemble properties of the dark halo population (Semboloni et al. 2006; Hoekstra et al. 2006). Substantial efforts are currently underway to improve all these measurements, and these will need to be matched by a comparable improvement in the theoretical predictions.

Additional tests and constraints may be obtained from observations of gravitational lensing effects. For example, foreground matter inhomogeneities may (de-)magnify images of distant sources thus changing their apparent magnitude. Although expected to be small for current type Ia supernova samples (Wambsganss et al. 1997; Holz 1998; Riess et al. 1998; Valageas 2000; Amanullah et al. 2003; Knop et al. 2003; Barris et al. 2004; Riess et al. 2004), some evidence for lensing effects on the observed luminosity distribution may be present in higher-redshift samples (Wang 2005; Jönsson et al. 2006). For future supernova surveys, one should be able to detect such effects with higher statistical significance (Metcalf 1999; Metcalf and Silk 1999; Minty et al. 2002; Munshi and Valageas 2006). This will then provide a further test of the standard structure formation model.

Sufficiently massive and concentrated structures along the line-of-sight can give rise to multiple images, to strongly magnified images and to highly distorted images, so-called giant arcs. The number of such strong-lensing events depends on the abundance of massive objects and on their detailed internal structure, both of which are sensitive to the background cosmology. Currently a much-debated question is whether the observed frequency of giant arcs (Luppino et al. 1999; Zaritsky and Gonzalez 2003; Gladders et al. 2003) is too high compared to predictions based on ΛCDM models with parameters favoured by other observations (Bartelmann et al. 1998; Meneghetti et al. 2000; Oguri et al. 2003; Dalal et al. 2004; Wambsganss et al. 2004; Li et al. 2005; Horesh et al. 2005;

Li et al. 2006; Wu and Chiueh 2006; Meneghetti et al. 2007). The problem appears particularly pressing at higher redshift, but available simulation results are not good enough to establish a clear discrepancy.

In this paper, we will study the optical depth for a variety of strong lensing effects as a function of source redshift in the standard ΛCDM cosmology. In particular, we will estimate the fraction of images that are highly magnified by gravitational lensing, that have a large length-to-width ratio, or that belong to multiply imaged sources. In addition, we compare the effect of foreground and background matter to that of the primary lens in generating these optical depths.

The results presented here were obtained by shooting random rays through a series of lens planes created from the Millennium Simulation (Springel et al. 2005). This very large N-body simulation of cosmic structure formation covers a volume comparable to the largest current surveys with substantially better resolution than previous simulations used for ray-tracing studies. Our set of lens planes represents the entire mass distribution between source and observer, allowing us to quantify the effects of foreground and background matter. In addition we have ensured that our ray-tracing techniques take full advantage both of the statistical power offered by the large volume of the simulation, and of its high spatial and mass resolution. This allows us to make more precise statements about model expectations than has previously been possible.

Our paper is organised as follows. In Sec. 2.2, we describe how we trace representative rays through the Millennium Simulation. Results for the magnification distribution as a function of source redshift are presented in Sec. 2.3.1. Strong-lensing optical depths are then discussed in Sec. 2.3.2. In Sec. 2.3.3, the mass and redshift distribution of the objects which cause strong lensing are examined, and we demonstrate that the errors induced by the finite volume and resolution of the simulation are relatively small. Biases induced by additional structure in front of or behind the principal lens are examined in Sec. 2.3.4 and are also found to be small. The paper concludes with a summary and outlook in Sec. 2.4.

2.2 Methods

2.2.1 The multiple-lens-plane approximation

In the multiple-lens-plane approximation (see, e.g., Blandford and Narayan 1986; Schneider et al. 1992), a finite number of planes are introduced along the line of sight, onto which the matter inhomogeneities in the backward light cone of the observer are projected. Between these lens planes, light is assumed to travel on straight lines. Light rays are deflected only when passing through a lens plane. The deflection angles may be calculated from the gradient of a lensing potential, which is connected to the projected matter distribution on the lens planes via a Poisson equation.

A light ray reaching the observer from a given angular position $\boldsymbol{\theta}$ can then be traced back to the angular position $\boldsymbol{\beta}$ of its source at given redshift z^{S}, thereby defining the lensing map

$$\mathrm{L}: \ \mathbb{P}^{\mathrm{I}} \rightarrow \mathbb{P}^{\mathrm{S}}: \ \boldsymbol{\theta} \mapsto \boldsymbol{\beta} \tag{2.1}$$

from the image plane $\mathbb{P}^{\mathrm{I}}$ to the source plane $\mathbb{P}^{\mathrm{S}}$. The distortion matrix $\mathbf{A} = \frac{\partial \boldsymbol{\beta}}{\partial \boldsymbol{\theta}}$, i.e. the Jacobian of the map, quantifies the magnification and distortion of images of small sources induced by gravitational lensing. The (signed) magnification μ of an image is given by the inverse determinant of the distortion matrix:

$$\mu = (\det \mathbf{A})^{-1} \,. \tag{2.2}$$

The decomposition (Schneider et al. 1992)

$$\mathbf{A} = \begin{pmatrix} \cos\varphi & \sin\varphi \\ -\sin\varphi & \cos\varphi \end{pmatrix} \begin{pmatrix} 1-\kappa-\gamma_1 & -\gamma_2 \\ -\gamma_2 & 1-\kappa+\gamma_1 \end{pmatrix} \tag{2.3}$$

of the distortion matrix defines the image rotation angle φ, the convergence κ, and the complex shear $\gamma = \gamma_1 + \mathrm{i}\gamma_2$. The reduced shear $g = \gamma/(1-\kappa)$ determines the major-to-minor axis ratio

$$r = \left| \frac{1+|g|}{1-|g|} \right| \tag{2.4}$$

of the elliptical images of sufficiently small circular sources. The determinant and trace of the distortion matrix may be used to categorise images (Schneider et al. 1992):[1]

- type I: $\det \mathbf{A} > 0$ and $\operatorname{tr} \mathbf{A} > 0$,
- type II: $\det \mathbf{A} < 0$,
- type III: $\det \mathbf{A} > 0$ and $\operatorname{tr} \mathbf{A} < 0$.

In all situations relevant for this work, images of type II and type III belong to sources that have multiple images. In the following, we will often consider type II and III images together as

- type II $\vee$ III: $\det \mathbf{A} < 0$ or $\operatorname{tr} \mathbf{A} < 0$.

In this paper, we want to study how often one can expect to observe images with certain lensing properties, e.g. highly magnified or strongly distorted images. In order to quantify the frequency of rays with a given property p, we define the optical depth

$$\tau_p^{\mathrm{I}} = \frac{\int_{\mathbb{P}^{\mathrm{I}}} \mathrm{d}^2\boldsymbol{\theta}\, 1_p(\boldsymbol{\theta})}{\int_{\mathbb{P}^{\mathrm{I}}} \mathrm{d}^2\boldsymbol{\theta}}, \tag{2.5}$$

where

$$1_p(\boldsymbol{\theta}) = \begin{cases} 1 & \text{if ray}(\boldsymbol{\theta}) \text{ has property } p, \text{ or} \\ 0 & \text{otherwise.} \end{cases}$$

For a uniform distribution of images in the image plane, τ_p^{I} estimates the fraction of images of sufficiently small sources that have the property p. Furthermore, we define the optical depth

$$\tau_p^{\mathrm{S}} = \frac{\int_{\mathbb{P}^{\mathrm{I}}} \mathrm{d}^2\boldsymbol{\theta}\; |\mu(\boldsymbol{\theta})|^{-1}\, 1_p(\boldsymbol{\theta})}{\int_{\mathbb{P}^{\mathrm{I}}} \mathrm{d}^2\boldsymbol{\theta}\; |\mu(\boldsymbol{\theta})|^{-1}} \tag{2.6}$$

[1] In Schneider et al. (1992), the trace and determinant of the symmetric part [i.e. second factor on the r.h.s. of Eq.(2.3)] of the distortion matrix $\mathbf{A}$ have been used. However, the determinant and the sign of the trace of $\mathbf{A}$ and its symmetric part are identical for $|\varphi| < \pi/2$.

to estimate the average fraction of images with properties p for a uniform distribution of sources in the source plane. These optical depths (assumed to be smooth) will be used to define corresponding probability density functions (pdf) for the magnification:

$$\mathrm{pdf}^{\mathrm{I/S}}(\mu') = \frac{\mathrm{d}}{\mathrm{d}\mu'} \tau^{\mathrm{I/S}}_{\mu(\boldsymbol{\theta})\leq\mu'} \,. \tag{2.7}$$

Compared to τ_p^{I}, the optical depth τ_p^{S} takes into account that areas in the image plane with higher magnification map to smaller areas in the source plane. This aspect of magnification bias leads to a lower image density in areas of higher magnification for volume-limited surveys. In magnitude-limited surveys, however, magnification can push images that would otherwise be too faint to be observed above the detection threshold. This aspect of magnification bias counteracts the previous one, but will not be discussed in this paper since it depends sensitively on the luminosity distribution of the source population.

Note that τ_p^{I} and τ_p^{S} differ from the optical depths

$$\tilde{\tau}_p^{\mathrm{S}} = \frac{\int_{\mathbb{P}^{\mathrm{S}}} \mathrm{d}^2\boldsymbol{\beta}\, 1_p(\boldsymbol{\beta})}{\int_{\mathbb{P}^{\mathrm{S}}} \mathrm{d}^2\boldsymbol{\beta}}. \tag{2.8}$$

discussed, e.g., by Schneider et al. (1992), which quantify the fraction of sources whose images have certain properties. The methods used in this paper do not yield enough information to deduce $\tilde{\tau}_p^{\mathrm{S}}$ in general. We will therefore restrict our discussion to τ_p^{I} and τ_p^{S}.

Roughly speaking, τ_p^{I} weights lensing events by their area on the sky, τ_p^{S} weights by the number of images, and $\tilde{\tau}_p^{\mathrm{S}}$ weights by the number of sources. In the absence of multiple images, τ_p^{S} and $\tilde{\tau}_p^{\mathrm{S}}$ would be identical. For strongly lensed properties such as considered in this paper, they can be significantly different: For τ_p^{S}, each of the multiple images of a source contributes individually, whereas all images of the same source contribute a single event event to $\tilde{\tau}_p^{\mathrm{S}}$. Consequently, for a given number N^S of uniformly distributed sources in the source plane, $N^S\tau_p^{\mathrm{S}}$ is the expected number of images with property p, whereas $N^S\tilde{\tau}_p^{\mathrm{S}}$ gives the expected number of sources. Obviously, the number of images is easier to count in observations than the number of sources.

2.2.2 The lens planes

Our methods for reconstructing the observer's backward light cone, for splitting it into a series of lens planes, and for calculating the matter distribution and deflection angles on these planes are generally similar to those used by Jain et al. (2000). They differ, however, in a number of important details which reflect our wish to take full advantage of the unprecedented statistical power offered by the large volume and high spatial and mass resolution of the Millennium Simulation. Here, we give a brief outline of our algorithms, reserving a detailed description for Hilbert et al. (in preparation).

The Millennium Simulation (Springel et al. 2005) is an N-body simulation of cosmological structure formation in a flat ΛCDM universe with a matter density of $\Omega_{\mathrm{M}} = 0.25$ (in terms of the critical density), a cosmological constant with $\Omega_\Lambda = 0.75$, a Hubble

constant $h = 0.73$ in units of $100\,\mathrm{km s^{-1} Mpc^{-1}}$, a primordial spectral index $n = 1$ and a normalisation parameter $\sigma_8 = 0.9$ for the linear density power spectrum. The simulation followed $N \approx 10^{10}$ particles of mass $m_\mathrm{p} = 8.6 \times 10^8 h^{-1}\,\mathrm{M}_\odot$ in a cubic region of comoving side $L = 500 h^{-1}\,\mathrm{Mpc}$ (assuming periodic boundary conditions) from redshift $z = 127$ to the present using a TreePM version of GADGET-2 (Springel 2005). The force softening length was chosen to be $5h^{-1}\,\mathrm{kpc}$ comoving. Snapshots of the simulation were stored on disk at 64 output times spaced approximately logarithmically in expansion factor for $z \geq 1$ and at roughly 200 Myr intervals after $z = 1$.

Since the fundamental cube of the simulation is too small to trace rays back to high redshift in a single replication, we have to make use of the periodicity to construct our light cones. In order to reduce the repetition of structure along long lines-of-sight (LOS) through this lattice-periodic matter distribution, we chose the LOS to be in the direction $\boldsymbol{n} = (1, 3, 10)$. This results in a comoving period of $5.24 h^{-1}\,\mathrm{Gpc}$ along the LOS, giving the first image of the origin at $z = 3.87$. It also allows us to maintain periodicity perpendicular to the LOS with a rectangular unit cell of dimension $1.58 h^{-1} \times 1.66 h^{-1}\,\mathrm{Gpc}^2$ comoving. This periodicity allows us to use Fast-Fourier-Transform (FFT) methods (e.g., Cooley and Tukey 1965; Frigo and Johnson 2005) to obtain the lensing potential and its derivatives on the lens planes.

To construct the matter distribution in the observer's backward light cone, we partitioned space into a series of redshift slices, each perpendicular to our chosen LOS and containing the part of the light cone closer to one of the snapshot redshifts than to its neighbours. The matter distribution within each such slice was then approximated by the stored particle data at the time of the corresponding snapshot, was projected onto the lens plane, and was placed at the comoving distance corresponding to the snapshot's redshift. In order to reduce the shot noise from individual particles, we employed an adaptive smoothing scheme. Each particle was smeared out into a cloud with projected surface mass density

$$\Sigma_\mathrm{p}(\boldsymbol{x}) = \begin{cases} \frac{3m_\mathrm{p}}{\pi r_\mathrm{p}^2}\left(1 - \frac{|\boldsymbol{x}-\boldsymbol{x}_\mathrm{p}|^2}{r_\mathrm{p}^2}\right)^2, & |\boldsymbol{x} - \boldsymbol{x}_\mathrm{p}| < r_\mathrm{p}, \\ 0, & |\boldsymbol{x} - \boldsymbol{x}_\mathrm{p}| \geq r_\mathrm{p}, \end{cases} \tag{2.9}$$

where $\boldsymbol{x}$ denotes comoving position on the lens plane, $\boldsymbol{x}_\mathrm{p}$ is the projected comoving particle position, and r_p denotes the comoving distance to the 64th nearest neighbour particle in *three* dimensions (i.e. before projection).

To calculate the lensing potential from the projected matter density, we used a particle-mesh particle-mesh (PMPM) method. The effective spatial resolution of the Millennium Simulation is about $5h^{-1}\,\mathrm{kpc}$ comoving in dense regions, where the particles' smoothing lengths become comparable to softening length of the simulation, i.e. $r_\mathrm{p} \sim 5h^{-1}\,\mathrm{kpc}$. Hence, a mesh spacing of $2.5h^{-1}\,\mathrm{kpc}$ comoving is required to exploit the numerical data without degradation. A single mesh of this spacing covering the whole periodic area of the lens plane (i.e. $1.58h^{-1} \times 1.66h^{-12}\,\mathrm{Gpc}^2$ comoving) would, however, be too demanding both to compute and to store. We therefore split the lensing potential Ψ into long-range

and short-range parts defined in Fourier space by:

$$\Psi_{\rm long}(\boldsymbol{k}) = \Psi(\boldsymbol{k}) \exp\left(-l_{\rm split}^2 \boldsymbol{k}^2\right), \text{ and} \tag{2.10a}$$

$$\Psi_{\rm short}(\boldsymbol{k}) = \Psi(\boldsymbol{k}) \left[1 - \exp\left(-l_{\rm split}^2 \boldsymbol{k}^2\right)\right]. \tag{2.10b}$$

The comoving splitting length $l_{\rm split} = 0.175 h^{-1}\,\mathrm{Mpc}$ characterises the spatial scale of the split. We use a 16384×16384 mesh covering the whole periodic area of the lens plane to calculate $\Psi_{\rm long}$ from the projected surface mass density by an FFT (Frigo and Johnson 2005) method. The long-range potential is calculated once and then stored on disk for each of the lens planes. To calculate $\Psi_{\rm short}$, a fine mesh with $2.5 h^{-1}\,\mathrm{kpc}$ spacing is used. This mesh only need cover a relatively small area around regions where the potential is required, i.e. where light rays intersect the lens plane. Because of the short range of $\Psi_{\rm short}$, periodic boundary conditions can be used on the fine mesh, provided points close to its boundary are excluded from subsequent analysis. Therefore, FFT methods can used without 'zero padding' to calculate $\Psi_{\rm short}$ on the fine mesh. The long- and short-range contributions to the deflection angles and shear matrices (i.e. the second derivatives of the lensing potential) are calculated on the two meshes by finite differencing of the potentials. The values between mesh points are obtained by bilinear interpolation. The resulting deflection angles and shear matrices at ray positions can then be used to advance the rays and their associated distortion matrices from one plane to the next.

2.2.3 Ray sampling

In order to estimate optical depths and magnification distributions, we shoot random rays through our set of lens planes. In doing this, we neglect correlations between the matter distributions on different lens planes. This allows us to pick random points on each lens plane as we propagate rays back in time, significantly simplifying and accelerating our code. Since the comoving separation between the lens planes is large ($\sim 100 h^{-1}\,\mathrm{Mpc}$), and the shear matrices are dominated by small-scale structure ($\lesssim 1 h^{-1}\,\mathrm{Mpc}$), this assumption is very well justified for the purposes of the current paper.

On each lens plane, 40 fields of about $40 h^{-1} \times 40 h^{-1}\,\mathrm{Mpc}^2$ comoving were selected at random. Within each of these fields, the shear matrix was calculated at 16 million random positions by our PMPM algorithm. The resulting 6.4×10^8 shear matrices for each plane were then stored on disk together with the positions at which each had been computed.

The shear matrices from all lens planes were next combined at random to produce 640 million simulated LOS from the observer back to high redshift. Imagining a small circular source at the position where each of these LOS intersects a particular lens plane, we can combine the shear matrices of the ray from all lower redshift planes to obtain the trace $\mathrm{tr}\,\mathbf{A}$ of the distortion matrix, the magnification $\mu = (\det \mathbf{A})^{-1}$, and the length-to-width ratio r of the source's image. The measured fractions of rays with certain properties, e.g. a large magnification, can then be used to estimate the corresponding optical depth to the redshift of the chosen plane.

This sampling method assumes that the rays are uniformly distributed in the image plane. The observed number N_p of rays with a particular property p, when compared

to the total number of rays N, is thus a straightforward Monte-Carlo estimate (without importance sampling) of the optical depth τ_p^{I}:

$$\tau_p^{\mathrm{I}} \approx \frac{N_p}{N} \; . \tag{2.11a}$$

The calculation of the corresponding optical depth τ_p^{S} requires using the individual magnifications $\mu(i)$ of the rays $i = 1, \ldots, N$ as statistical weights:

$$\tau_p^{\mathrm{S}} \approx \frac{\sum_{i=1}^{N} \left|\mu^{-1}(i)\right| 1_p(i)}{\sum_{i=1}^{N} \left|\mu^{-1}(i)\right|} \; . \tag{2.11b}$$

The matter distribution on our lens planes is guaranteed to be periodic, smooth and non-singular as a result of the adaptive smoothing we use. Furthermore, a large and random area of the image plane is mapped onto an equally large area in the source plane by our lensing map (2.1). Thus a representative ray sample should satisfy [see Eq. (2.15) in Appendix 2.5]:

$$1 \approx \frac{1}{N} \sum_{i=1}^{N} \mu^{-1}(i) \; . \tag{2.12}$$

For our ray sample, we find this relation to be satisfied to quite high precision; for all source planes the deviation is smaller than 0.003.

Our ray sampling technique neglects correlations between the structure on different lens planes. The effects of the lens environment on scales smaller than $100h^{-1}\,\mathrm{Mpc}$ comoving should be correctly represented, however, and the effects of uncorrelated fluctuations in the density of foreground and background matter are also included properly. This simple procedure should thus give accurate results in the context where we use it, but we note that it does not allow the construction of extended images of extended sources. This can be done by relatively straightforward extensions of our methods which we reserve for future papers.

2.3 Results

2.3.1 The magnification distribution

From the magnifications of our random rays, we have estimated the probability density functions $\mathrm{pdf}^{\mathrm{I}}(\mu)$ and $\mathrm{pdf}^{\mathrm{S}}(\mu)$. These are compared for a source redshift $z^{\mathrm{S}} = 2.1$ in Fig. 2.1a. One can readily see the stronger fall-off to high magnification for $\mathrm{pdf}^{\mathrm{S}}(\mu)$, which is a consequence of the relation $\mathrm{pdf}^{\mathrm{S}}(\mu) \approx |\mu|^{-1}\mathrm{pdf}^{\mathrm{I}}(\mu)$ [see Eq. (2.16) in the Appendix]. The asymptotic behaviour predicted from catastrophe theory (Schneider et al. 1992), i.e. $\mathrm{pdf}^{\mathrm{I}}(\mu) \propto \mu^{-2}$ and $\mathrm{pdf}^{\mathrm{S}}(\mu) \propto \mu^{-3}$, is reached for magnifications $\mu \gtrsim 20$.

Probability density functions $\mathrm{pdf}^{\mathrm{S}}(\mu)$ for different source redshifts z^{S} are shown in Fig. 2.1b. With increasing z^{S}, the peak of the distribution broadens and moves to lower μ, whereas the high-μ tail increases in amplitude. The peak positions and the widths of the pdfs, i.e. their modes μ_{peak} and full-widths-at-half-maximum FWHM, are plotted as functions of source redshift in Fig. 2.2. The shift of the peak with increasing redshift

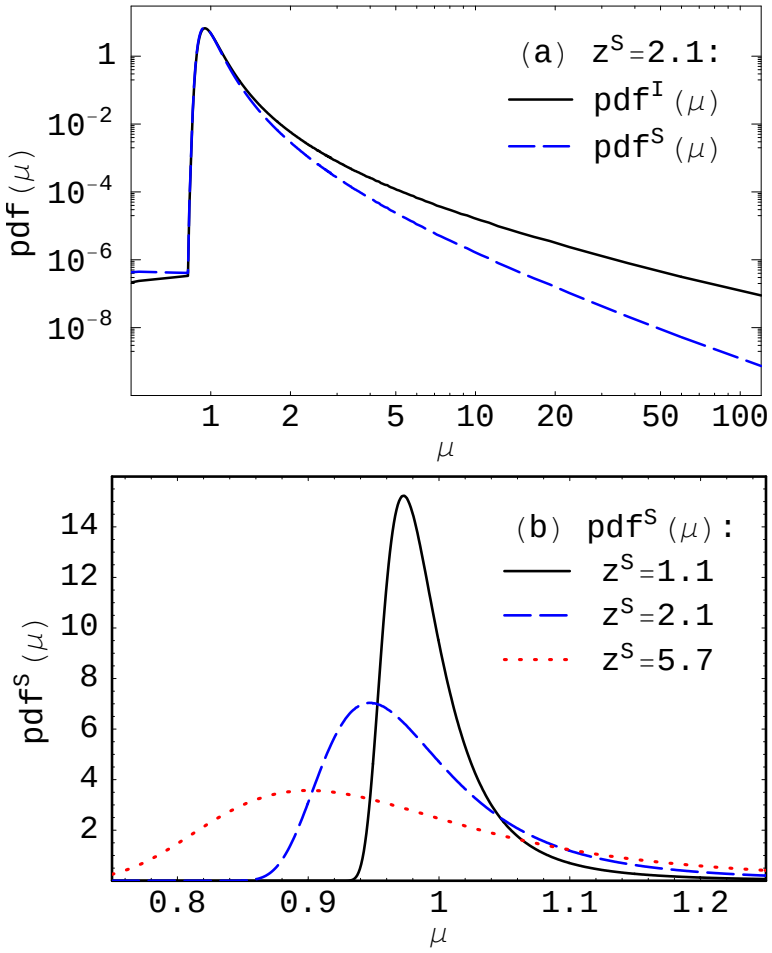

Figure 2.1: The probability density pdf(μ) of the magnification μ. (a) Logarithmic plot comparing $\mathrm{pdf}^{\mathrm{I}}(\mu)$ (solid line) and $\mathrm{pdf}^{\mathrm{S}}(\mu)$ (dashed lines) for a source redshift of $z^{\mathrm{S}} = 2.1$. (b) Linear plot comparing the $\mathrm{pdf}^{\mathrm{I}}(\mu)$ around $\mu = 1$ for different source redshifts, $z^{\mathrm{S}} = 1.1$ (solid line), $z^{\mathrm{S}} = 2.1$ (dashed lines) and $z^{\mathrm{S}} = 5.7$ (dotted lines).

balances the heavier tail so that $\int \mu \mathrm{pdf}^{\mathrm{S}}(\mu)\mathrm{d}\mu \approx 1$ for all redshifts [see Eq. (2.17)]. These results for peak position and width are in good agreement with those of Valageas (2000) and Fluke et al. (2002), who considered similar cosmologies.

There is a lower bound to the magnification of images of type I, which is realized for rays which propagate through empty cones (i.e., for which the matter density vanishes along their path) and which are subject to no shear effects (e.g., Dyer and Roeder 1972; Seitz and Schneider 1992). No light ray can diverge more strongly than such an empty-beam ray. Lower magnifications can only be produced for overfocussed rays which then belong to Type II or III. A simple way of calculating this lower bound $\mu_{\min}$ for a flat universe is given in Appendix 2.6. The steep rise in the probability density of the magnification at $\mu \approx 0.83$ seen in Fig. 2.1(a) is substantially larger than the theoretical bound $\mu_{\min} = 0.69$ for $z^{\mathrm{S}} = 2.1$, indicating that there are no real empty cones in a realistic universe, which is in agreement with findings by Vale and White (2003).

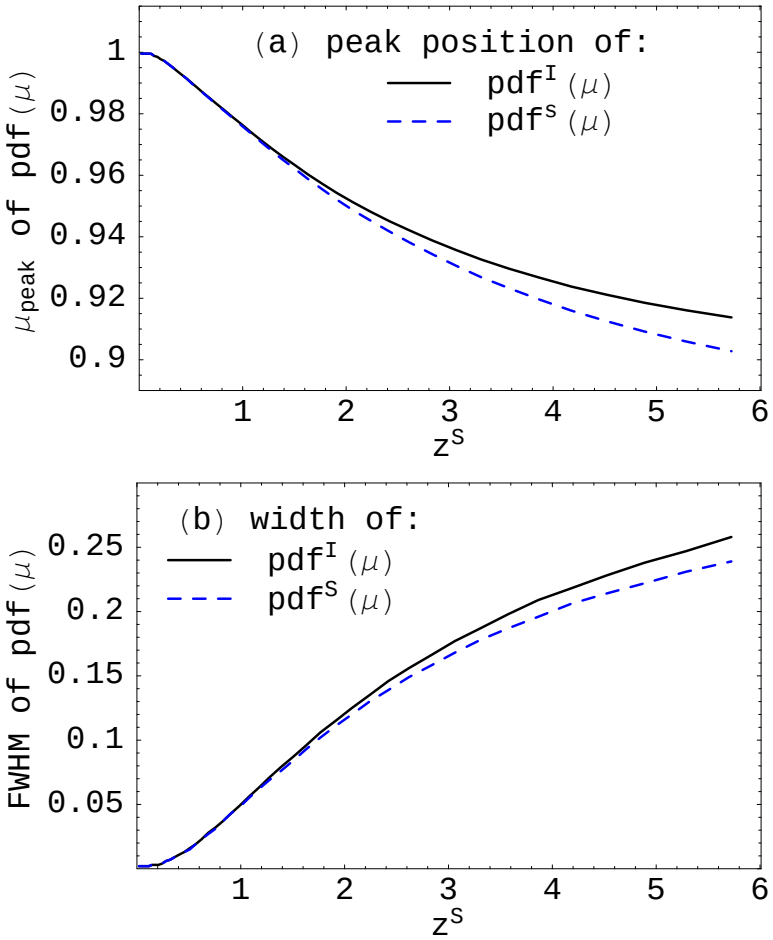

Figure 2.2: The peak position (a) and the width (b) of the probability densities $\mathrm{pdf}^{\mathrm{I}}(\mu)$ (solid lines) and $\mathrm{pdf}^{\mathrm{S}}(\mu)$ (dashed lines) for the magnification μ as a function of source redshift z^{S}. The distributions get broader and more skew with increasing z^{S}.

2.3.2 Strong-lensing optical depths

Sufficiently concentrated matter clumps between distant light sources and the observer can give rise to highly magnified, strongly distorted, or multiple images. We refer to such phenomena as strong lensing. In order to quantify the amount of strong lensing expected in a ΛCDM universe with the parameters of the Millennium Simulation, we used our large set of random rays to estimate:

- the fraction with $\det \mathbf{A} < 0$ (type II),
- the fraction with $\det \mathbf{A} > 0$ and $\mathrm{tr}\, \mathbf{A} < 0$ (type III),
- the fraction with $\det \mathbf{A} < 0$ or $\mathrm{tr}\, \mathbf{A} < 0$, i.e. the sum of the two previous classes (type II $\vee$ III),
- the fraction with a length-to-width ratio $r > 10$ for images of sufficiently small circular sources, and

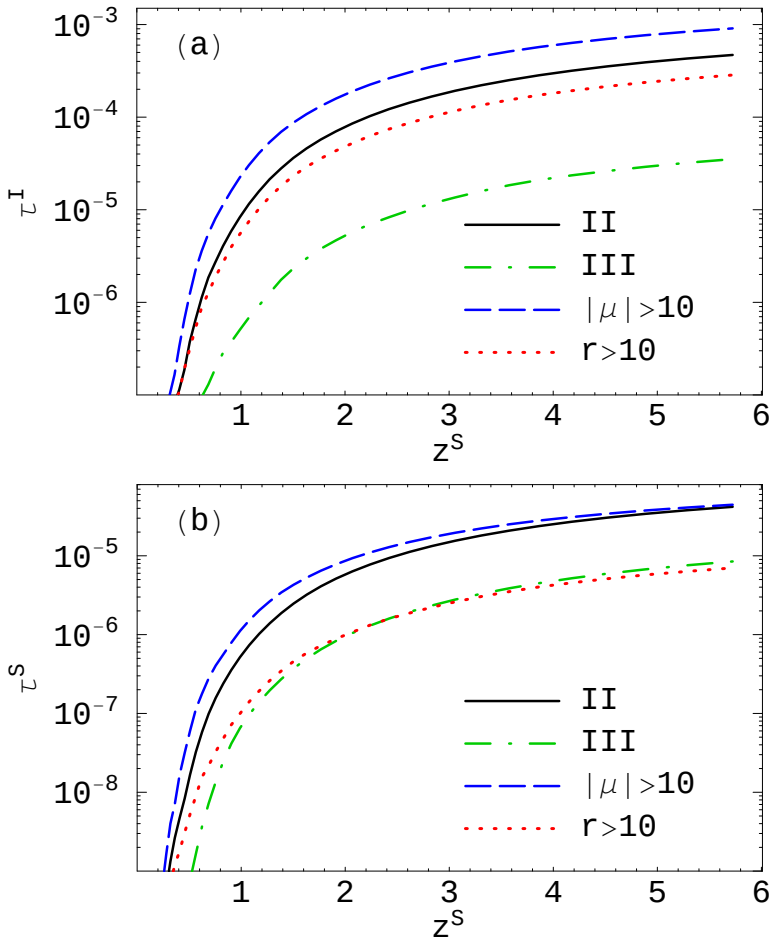

Figure 2.3: Optical depths for images of small circular sources of type II (solid lines), of type III (dash-dotted lines), with large magnification (dashed lines) and with large length-to-width ratio (dotted lines), assuming a uniform distribution of images in the image plane (a), and a uniform distribution of sources in the source plane (b). Note that the optical depths are significantly smaller in the latter case, and that the relative optical depths for different types of strong lensing are not the same in the two cases.

- the fraction with magnification $|\mu| > 10$.

The corresponding optical depths $\tau_p^{\rm I}(z^{\rm S})$ and $\tau_p^{\rm S}(z^{\rm S})$ are plotted in Fig. 2.3 as functions of the source redshift $z^{\rm S}$. Since all the image properties we consider are (either by definition or at least statistically) associated with large magnifications, the optical depths $\tau_p^{\rm S}(z^{\rm S})$ are always a factor 5 to 20 smaller than the corresponding $\tau_p^{\rm I}(z^{\rm S})$.

The optical depths for $r > 10$ are 2 to 20 times smaller than those for $|\mu| > 10$. Similar results have been found by Dalal et al. (2004) and by Li et al. (2005). Evidently, the optical depth for highly magnified images does not provide a reliable estimate for the probability of images with a large length-to-width ratio.

The optical depth $\tau_{r>10}^{\rm S}$ may be a reasonable approximation to the optical depth for giant arcs with length-to-width ratio $r > 10$, since both finite source size and finite source

ellipticity affect this particular property only weakly. Moreover the two effects work in opposite directions. For example, Li et al. (2005) found that the optical depth for $r > 10$ is almost identical to the optical depth for arc images with length-to-width-ratios > 10 of elliptical sources with an effective diameter of 1 arcsec.

All our optical depths show a strong dependence on source redshift, similar to that previously noted by Wambsganss et al. (2004) and Li et al. (2005). Comparing to their results in detail, however, we find a somewhat stronger redshift dependence, resulting in 2 to 3 times higher optical depths at $z^{\mathrm{S}} > 0.5$. There are various possible explanations for this discrepancy. The simulations they use have 3 to 20 times worse mass resolution than the Millennium Simulation. In addition, Wambsganss et al. (2004) reduced their spatial resolution on lens planes with increasing redshift, thereby potentially missing some low mass lenses, whereas we always use the full spatial resolution permitted by the force resolution of the Millennium Simulation. Furthermore, Wambsganss et al. (2004) measured the fraction of multiply imaged sources for which at least one image has $|\mu| > 10$. Thus they do not include sources with a single highly magnified image, as can occur for a marginally subcritical lens. Moreover, they do not account for the fact that multiply imaged sources can give rise to more than one image with $|\mu| > 10$. Similarly, Li et al. (2005) only considered the magnification μ and length-to-width-ratio r of the brightest image of multiply imaged sources for the calculation of the optical depths for $|\mu| > 10$ and $r > 10$, although they took into account all giant-arc images for a given population of extended sources in their calculation of the optical depth for giant arcs. Furthermore, they only considered massive clusters and neglected possible contributions from foreground and background matter. These decisions caused them to underestimate the total cross-sections for strong lensing (at least for smaller sources).

Fold singularities generically produce strongly magnified and distorted images as pairs, and sources near cusps may give rise to one or three strongly magnified or distorted images (Schneider et al. 1992). Therefore, sources with multiple highly magnified or strongly distorted images might explain a substantial part of the discrepancy between our results and those of Wambsganss et al. (2004) and Li et al. (2005). With our methods, we cannot quantify this effect, but we discuss the other effects further in the following sections.

2.3.3 Lens properties

In most cases, the properties of strongly lensed rays, i.e. rays with $\det \mathbf{A} < 0$, $\operatorname{tr} \mathbf{A} < 0$, $|\mu| > 10$, or $r > 10$, are predominantly caused by a single matter clump along the line of sight. We refer to this as the lens of the ray. In order to find these clumps and to study their properties, we determined for each strongly lensed ray those lens planes which were sufficient to produce the relevant property in the single-plane approximation. Only 2×10^{-4} of all rays had more than one 'sufficient' plane, and we will simply ignore these rays in the following. On the other hand, there was no sufficient plane for up to 41 percent of the rays, depending on source redshift and the property considered, so we will discuss these cases in more detail in Sec 2.3.4. For most strongly lensed rays, however, this simple criterion identifies exactly one lens plane. The redshift of this plane was then taken as the lens redshift z^{L} for the ray. For rays of type II $\vee$ III (i.e. rays

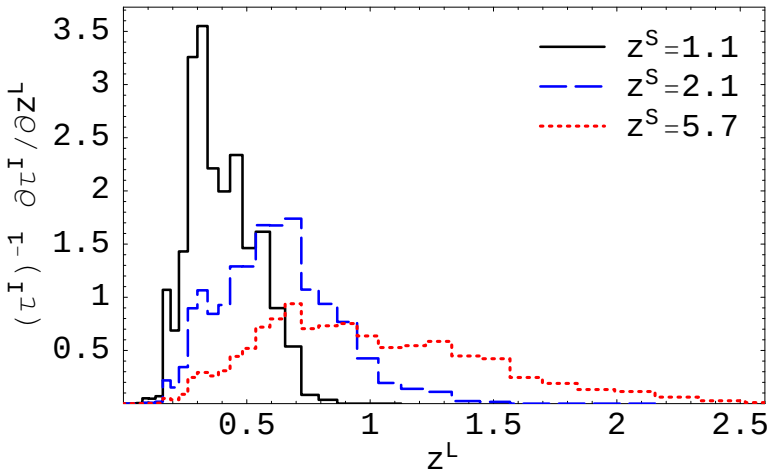

Figure 2.4: The cross-section $\partial\tau^{\mathrm{I}}/\partial z^{\mathrm{L}}$ for rays of type II $\vee$ III as a function of lens redshift z^{L} for sources at redshift $z^{\mathrm{S}} = 1.1$ (solid line), $z^{\mathrm{S}} = 2.1$ (dashed line), and $z^{\mathrm{S}} = 5.7$ (dotted line). Even for high redshift sources, the typical lens redshift is relatively low.

with $\det \mathbf{A} < 0$ or $\mathrm{tr}\,\mathbf{A} < 0$), the resulting lens redshift distribution is illustrated in Fig. 2.4. Here we plot the cross-section $\partial\tau^{\mathrm{I}}/\partial z^{\mathrm{L}}$ as a function of lens redshift z^{L} for various source redshifts z^{S}. Even for sources at redshift $z^{\mathrm{S}} = 5.7$, most of the lenses have redshift $z^{\mathrm{L}} < 2.5$. The relatively low cross-section at higher z^{L} reflects both the lower abundance of massive halos and the less favourable geometry for lensing at these redshifts (see Fig. 2.6). The lens redshift distributions for rays with $|\mu| > 10$ and with $r > 10$ are almost indistinguishable from that of Fig. 2.4 despite the different total optical depths.

We studied not only the redshift of the clumps acting as strong lenses, but also their masses. All significant matter concentrations have already been identified as DM halos in the simulation and their masses and central positions are available in the simulation archive. We first projected the centres of all halos onto the lens planes in the same way as was done for the particles. For each strongly lensed ray and for all DM halos close to the point where the ray intersects a lens plane, we determined the ratio M^{L}/b, where M^{L} is the conventional halo mass (defined as the mass within a sphere with mean enclosed density 200 times the cosmological mean), and b denotes the impact parameter of the ray with respect to halo centre.

The DM halo with the largest M^{L}/b on the sufficient plane was then defined to be the lens of ray. We discarded from further analysis those 3 to 6 percent of rays for which the largest value of M^{L}/b was not at least ten times the second largest value. This cut removed all cases where one could not easily separate the influence of several neighbouring DM halos, for example in merging clusters.[2] The resulting distributions of lens masses for rays of type II $\vee$ III, with $|\mu| > 10$, and with $r > 10$ are compared in Fig. 2.5a, where the cross-sections $\partial\tau^{\mathrm{I}}/\partial \log M^{\mathrm{L}}$ are plotted for $z^{\mathrm{S}} = 2.1$ as a function of lens halo mass M^{L}. Although the corresponding total optical depths are quite different,

[2]The choice M^{L}/b is somewhat arbitrary. We also tried M^{L}/b^2, but a different halo was chosen only in a few cases, all of which were removed by our imposed ratio cut.

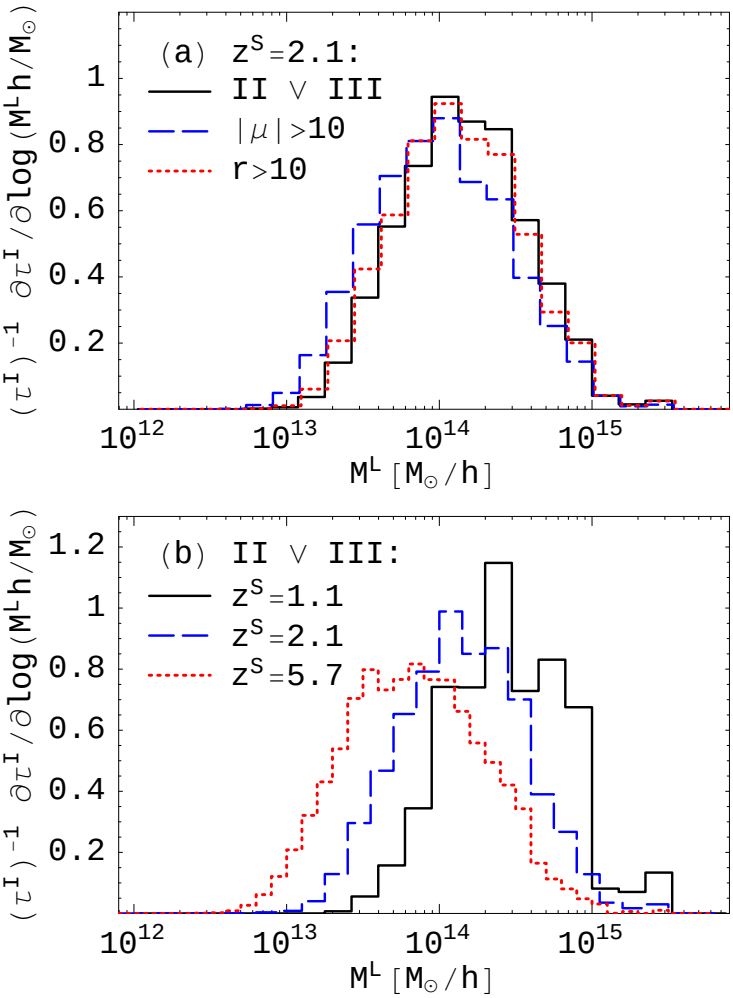

Figure 2.5: The cross-section $\partial\tau^{\mathrm{I}}/\partial \log M^{\mathrm{L}}$ as a function of the mass of the lensing halo M^{L} (see text). Panel (a) compares rays of type II ∨ III (solid line), rays with $|\mu| > 10$ (dashed line), and rays with $|r| > 10$ (dotted line) for source redshift $z^{\mathrm{S}} = 2.1$. (b) compares rays of type II∨III for sources at redshift $z^{\mathrm{S}} = 1.1$ (solid line), $z^{\mathrm{S}} = 2.1$ (dashed line), and $z^{\mathrm{S}} = 5.7$ (dotted line). The lens mass distribution is almost independent of the type of strong lensing event, but it shifts towards lower masses for higher source redshift.

their lens mass distributions are very similar. There is only a small shift toward lower masses for rays with $|\mu| > 10$, and $r > 10$ compared to rays of type II ∨ III. In the following we will restrict discussion to the latter for simplicity.

In Fig. 2.5b, the cross-section $\partial\tau^{\mathrm{I}}/\partial \log M^{\mathrm{L}}$ is plotted as a function of mass for type-II∨III rays and for various source redshifts z^{S}. The measured cross-section $\partial\tau^{\mathrm{I}}/\partial \log M^{\mathrm{L}}$ vanishes for masses below $4 \times 10^{12} h^{-1}\,\mathrm{M}_\odot$ and above $4 \times 10^{15} h^{-1}\,\mathrm{M}_\odot$. The main contribution to the optical depth τ^{I} comes from halos with $10^{13} h^{-1}\,\mathrm{M}_\odot \lesssim M^{\mathrm{L}} \lesssim 10^{15} h^{-1}\,\mathrm{M}_\odot$. For higher source redshifts, the cross section has more weight at lower masses.

The upper mass limit for the cross-section simply reflects the fact that there are no halos more massive than $4 \times 10^{15} h^{-1}\,\mathrm{M}_\odot$ in the simulation. However, the cross-section

decreases rapidly with increasing $M^{\rm L}$ already for $M^{\rm L} > 10^{15} h^{-1}\,{\rm M}_\odot$. The exponential decrease in halo abundance with increasing mass apparently dominates over the increasing cross-section of individual halos.

At all source redshifts there is a significant contribution from halos with $M^{\rm L} < 10^{14} h^{-1}\,{\rm M}_\odot$. For the small sources considered here, the set of DM halos causing strong lensing extends to substantially lower masses than Li et al. (2005) and Dalal et al. (2004) suggest for halos producing giant arcs. The Millennium Simulation has 12 to 20 times better mass resolution than the simulations used by these authors. This provides a considerably better representation of the central halo regions which produce strong lensing. In addition, halos are inefficient in generating strongly distorted images for sources with angular extent comparable to or larger than their Einstein radii. Thus, neglecting or incorrectly treating halos below a given mass (e.g. because of limited mass resolution) has a larger effect on the optical depths for small sources than on those for extended sources – especially for high source redshifts. Together these effects may explain why we find 2 to 3 times larger optical depths at high redshift than the values given by Li et al. (2005).

What sets the lower mass limit for the cross-section $\partial\tau^{\rm I}/\partial \log M^{\rm L}$? The nominal mass resolution for *identifying* DM halos in the Millennium Simulation is about $10^{10} h^{-1}\,{\rm M}_\odot$, so there are plenty of halos with $M^{\rm L} < 4 \times 10^{12} h^{-1}\,{\rm M}_\odot$. The identification limit cannot, in itself, explain the lack of halos less massive than $4 \times 10^{12} h^{-1}\,{\rm M}_\odot$ in our sample. However, the regions capable of causing strong lensing are very small for low-mass halos, so our cross section estimates may be limited by the resolution of our lens planes; critical regions with a diameter below the mesh spacing or the effective gravitational smoothing scale are not resolved. In order to estimate the mass limit induced by these effects, we considered spherical NFW halos (Navarro et al. 1997) with concentration parameter

$$c(M^{\rm L}, z^{\rm L}) = \frac{9.59}{1+z^{\rm L}} \left(\frac{M^{\rm L}}{10^{14} h^{-1}\,{\rm M}_\odot} \right)^{-0.102} \tag{2.13}$$

determined by halo mass and redshift (Dolag et al. 2004). For given lens and source redshifts, there is a minimum lens mass for which the Einstein radius exceeds the resolution limit of our lens plane. We take the latter to be $5h^{-1}\,{\rm kpc}$ comoving, thus requiring a minimum of four mesh points across the Einstein diameter. This limit takes into account not just the limit imposed by the mesh spacing of $2.5h^{-1}\,{\rm kpc}$ ($\sim 1.7h^{-1}\,{\rm kpc}$ in radius), but also the force softening and the smoothing for particles in the halo cores. The solid line in Fig. 2.6 shows the resulting minimum mass $M^{\rm L}$ as a function of $z^{\rm L}$ for $z^{\rm S} = 5.7$. The shading in this plot gives the cross-section $\partial^2\tau^{\rm I}/\partial z^{\rm L} \partial \log M^{\rm L}$. The region of the $(z^{\rm L}, \log M^{\rm L})$-plane with non-zero cross-section is bounded above by the largest halo mass at each redshift (the dashed line). The lower boundary of this region lies slightly below our analytic estimate of the resolution limit (the solid line). About 6 percent of the cross-section is below the analytic estimate. Some deviation is expected because this estimate does not include the effects of intrinsic ellipticity, asymmetries and substructure, and of the scatter in concentration of halos of given mass. It also neglects scatter due to additional matter inhomogeneities along the LOS. These effects should result in strong lensing by somewhat lower mass halos than our simple spherical

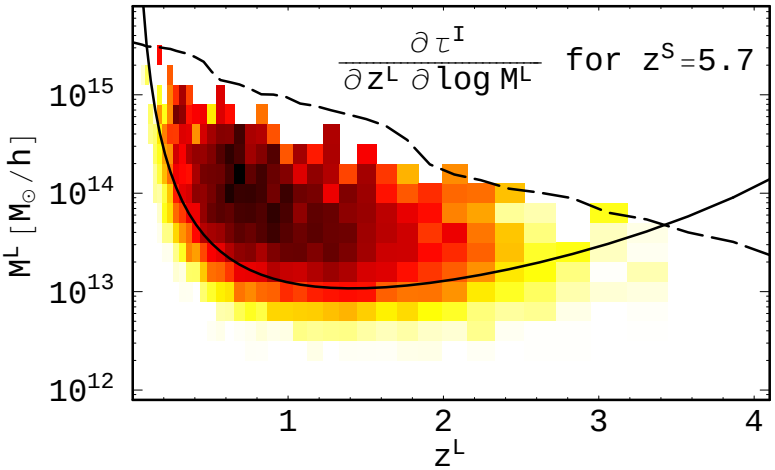

Figure 2.6: The cross-section $\partial\tau^{\mathrm{I}}/\partial z^{\mathrm{L}}\partial\log M^{\mathrm{L}}$ for rays of type II $\vee$ III and sources at redshift $z^{\mathrm{S}} = 5.7$ as a function of the redshift z^{L} and halo mass M^{L} of the lens. Darker areas correspond to higher cross-sections (on a logarithmic scale). The dashed line marks the mass of the largest DM halo in the Millennium Simulation at each redshift. The solid line joins masses for which a spherical NFW halo of typical concentration would have Einstein radius $5h^{-1}$ kpc, approximately the resolution limit on the lens planes. The cross-section for strong lensing in our ray sample is almost entirely contained between these two limits.

model would indicate (Meneghetti et al. 2007; Hennawi et al. 2007b; Fedeli et al. 2007). In particular, a high-concentration, prolate halo with its major axis along the LOS has a greatly enhanced cross-section relative to a spherical halo of the same mass with a typical concentration. Moreover, ellipticity and scatter in concentration lead to larger cross-sections *on average* compared to spherical NFW halos of the mean concentration.

Besides the resolution limit due to the mesh spacing and local smoothing scale on the lens plane, there is another factor limiting the resolution: The critical regions of the relevant halos may not have been simulated to the accuracy required to get fully converged results in the face of discreteness effects resulting from the relatively small number of particles in these regions. According to the criteria given by Power et al. (2003), only the most massive halos in the Millennium Simulation at $0.3 < z < 2$ should have spherically averaged density profiles which are fully converged at radii comparable to their Einstein radius. At lower masses and at other redshifts the particle number in the inner regions is below the value advocated by Power et al. (2003). (In contrast, the softening length of the Millennium Simulation appears adequate to avoid major problems.) When the particle number is too small, Power et al. (2003) show that simulations typically underestimate the central concentration of a halo, implying a reduction in its strong lensing cross-section. This effect is a relatively slow function of particle mass. In addition, strong lensing depends on the projected density distribution rather than the 3-D density profile which Power et al. (2003) studied; there are typically two to three orders of magnitude more particles projected within a halo's Einstein radius than there are within a central sphere of radius r_E. Thus it is unclear how seriously the under-resolution of halo cores will affect the cross-sections we calculate.

To obtain a rough estimate of how much optical depth we lose due to resolution

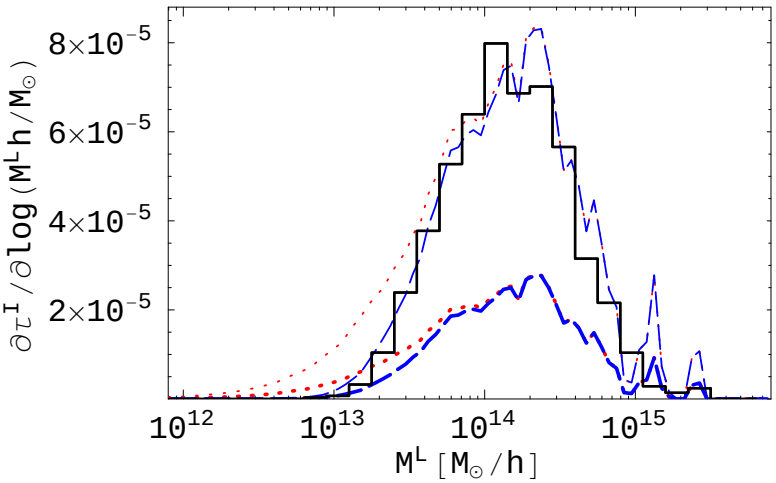

Figure 2.7: The cross-section $\partial\tau^{\rm I}/\partial\log M^{\rm L}$ for rays of type II $\vee$ III to sources at $z^{\rm S} = 2.1$ as a function of the lensing halo mass $M^{\rm L}$. The solid histogram gives the direct estimate from the Millennium Simulation. For all other curves we have replaced each halo in the simulation by a spherical NFW halo with the same virial mass and maximal circular velocity. The heavy dotted line gives the result for all halos, while the heavy dashed line shows the effect of excluding all halos with Einstein radius $r_{\rm E} < 5h^{-1}\,$kpc comoving. Thin lines show the result of scaling these two curves up by a factor of 3, so that their shape can be compared more easily to the direct estimate from the simulation. The cut-off in cross-section at low halo mass in the simulation appears to correspond well to that induced by this simple model for the resolution limit. This suggests that resolution effects reduce our total cross-sections by of order 15%.

effects, we calculated the cross-section $\partial\tau^{\rm I}_{\rm II\vee III}/\partial\log M^{\rm L}$ approximating all DM halos in the Millennium Simulation by spherical NFW halos while either (i) taking into account or (ii) disregarding halos with an Einstein radius $r_{\rm E} < 5h^{-1}\,$kpc comoving. In doing this, we used the measured maximal circular velocity of each halo to estimate its concentration parameter, rather than assuming the concentration to be given by Eq. (2.13). The cross-sections obtained for the two cases are shown in Fig. 2.7. Due to the scatter in the halo concentrations, the analytical estimate excluding halos with Einstein radius $r_E < 5h^{-1}\,$kpc extends to lower masses than the limit calculated above by assuming Eq. (2.13) for all halos. The estimate for $\tau^{\rm I}_{\rm II\vee III}$ including halos with Einstein radius $r_E < 5h^{-1}\,$kpc is only about 15 percent larger than the estimate excluding such halos. Moreover, there is no significant contribution to the full estimate from halos below a few times $10^{12}h^{-1}\,{\rm M}_\odot$. Indeed, a detailed analysis shows that the strong-lensing cross-section of spherical NFW halos with $M^{\rm L} \le 10^{13}h^{-1}\,{\rm M}_\odot$ decreases exponentially with decreasing mass, and is not compensated by the increasing number of halos.

Fig. 2.7 also shows the two spherical halo-based estimates scaled up by a factor of 3. The curve neglecting halos with small Einstein radii is then a good match to the histogram derived directly from the simulation. Hence, the cross-section $\partial\tau^{\rm I}_{\rm II\vee III}/\partial\log M^{\rm L}$ is about three times as large for simulated halos as for spherical NFW halos, at least for halo masses $M^{\rm L} > 4\times10^{13}h^{-1}\,{\rm M}_\odot$ where the resolution limit is unimportant. If this result applies also at lower mass, it implies that limited resolution does not lead us to

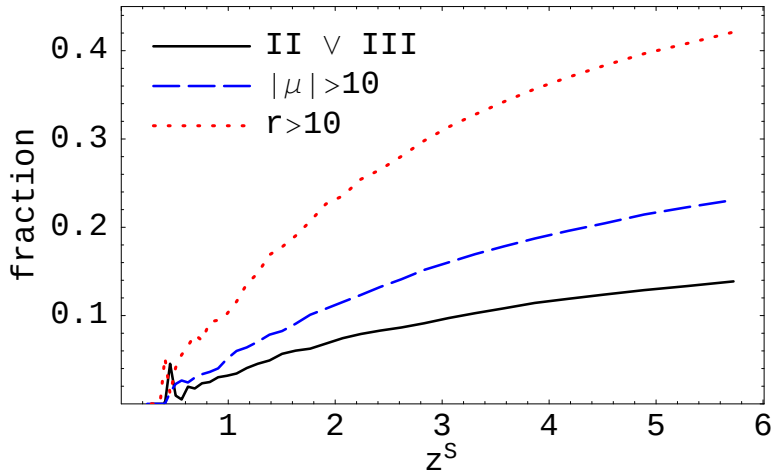

Figure 2.8: The fraction of rays of type II ∨ III (solid line), of rays with $|\mu| > 10$ (dashed line), and of rays with $r > 10$ (dotted line) to source redshift z^{S} for which no single lens plane is able to generate the relevant property on its own. The relative importance of foreground and background material clearly increases with increasing z^{S}.

underestimate total optical depths substantially, perhaps only by about 15%. Note that the missing cross section corresponds to very small image splittings $\Delta\theta^{\mathrm{I}} \lesssim 1\,\mathrm{arcsec}$, a scale where the gravitational effects of the baryons in the central galaxy are expected to be important.

2.3.4 Effects of additional matter along the line of sight

For some rays with $\det \mathbf{A} < 0$, $\mathrm{tr}\,\mathbf{A} < 0$, $|\mu| > 10$, or $r > 10$, there is no individual lens plane that is sufficient to produce the relevant property in the single-plane approximation. The fraction of rays for which this is the case is shown in Fig. 2.8. It increases with increasing source redshift, is lowest for rays of type II ∨ III, and is highest for rays with $r > 10$. This fraction gives an indication of the extent to which foreground and background material affects the strong lensing optical depths we have estimated. Such material is expected to have no or little effect on average for the image(s) of a randomly chosen object of given redshift. However, by selecting rays in the extreme tail of lensing distributions, we may be significantly biased towards lines-of-sight for which the additional material enhances the effect of the primary lens. Fig. 2.8 suggests that additional material is particularly effective in enhancing the probability of highly distorted images (e.g. giant arcs), presumably because these are sensitive to the lensing map in a narrow region around its critical lines. One should, however, bear in mind that not only do certain directions gain a considered property through the primary lens being supplemented by additional LOS material, but other regions lose the same property because the primary lens is counteracted by lower than average additional material. Therefore, the fractions of Fig. 2.8 do not reflect the overall contribution of line-of-sight material to our cross-sections.

In general, the effects of foreground and background material are relatively weak. In the cases where there is no single plane which is sufficient to generate the relevant

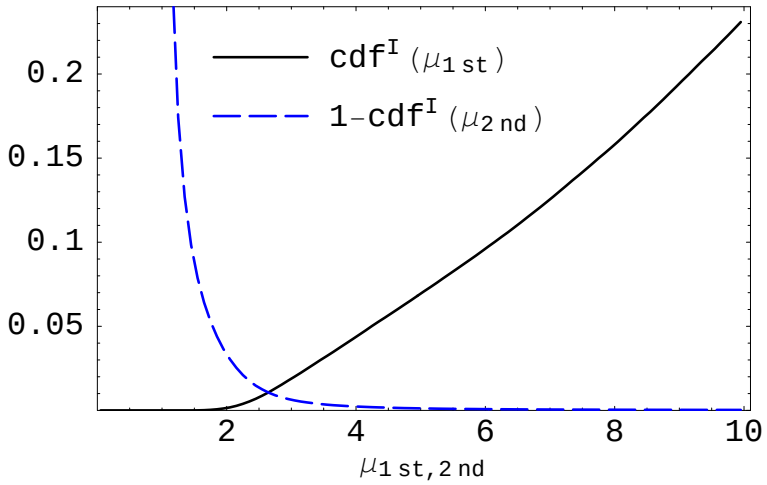

Figure 2.9: The cumulative distribution function $\mathrm{cdf}^{\mathrm{I}}$ of the largest $\mu_{1\mathrm{st}}$ and of the second largest $\mu_{2\mathrm{nd}}$ single-plane magnification for all rays with a magnification $|\mu| > 10$ to source redshift $z^{\mathrm{S}} = 5.7$. For clarity we plot $1 - \mathrm{cdf}^{\mathrm{I}}(\mu_{2\mathrm{nd}})$ rather than $\mathrm{cdf}^{\mathrm{I}}(\mu_{2\mathrm{nd}})$ so that the high tail of the distribution can be compared with the low tail of $\mathrm{cdf}^{\mathrm{I}}(\mu_{1\mathrm{st}})$. In almost all cases the effect due to the primary lens is strongly dominant.

property, there is still usually a single plane dominating the lensing effects. As an example, we determined for each ray with $|\mu| > 10$ and $z^{\mathrm{S}} = 5.7$ the planes which gave rise to the largest and second largest magnifications, $\mu_{1\mathrm{st}}$ and $\mu_{2\mathrm{nd}}$, resp., in the single-plane approximation. The cumulative distribution of these magnifications is shown in Fig. 2.9. Even though the fraction of rays with $\mu_{1\mathrm{st}} < 10$ is about 23 percent, virtually all rays have $\mu_{1\mathrm{st}} > 2$ and 93 percent of the rays have $\mu_{1\mathrm{st}} > 5$. In most of the cases where there is no sufficient lens plane to cause $|\mu| > 10$ alone, there is still an 'almost sufficient' plane that gives rise to a magnification significantly larger than unity. In only 3 percent of cases is $\mu_{2\mathrm{nd}} > 2$, and in 90 percent of all rays we find $\mu_{2\mathrm{nd}} < 1.4$. Thus to a good approximation strong lensing can be thought of as being caused by individual objects. These results agree qualitatively with the findings of Wambsganss et al. (2005) for the distribution of the surface mass density.

There are, nevertheless, a few strongly lensed rays whose properties are due to more than one object or lens plane. As noted above, two or more objects at similar redshift contribute significantly for a few percent of all rays. Fig. 2.9 shows that for a further few percent two or more uncorrelated objects at different redshifts make a significant contribution. For the remaining rays the overall effects of foreground and background matter are at a much lower level. To demonstrate this quantitatively, we first determined the projected mass overdensity at the position of each ray on each plane. We then divided these overdensities by the critical surface densities of the relevant planes. Finally, for each ray we summed the contributions from all planes to obtain a 'LOS convergence' $\tilde{\kappa}$, which – to be more precise – is the lensing-efficiency-weighted projection of the matter overdensity along the ray. (This is equal to the convergence κ in the single-plane and weak-lensing approximations.) We then performed a similar calculation for all rays of type II $\vee$ III, with $|\mu| > 10$ or with $r > 10$. In addition, when calculating $\tilde{\kappa}$ for these

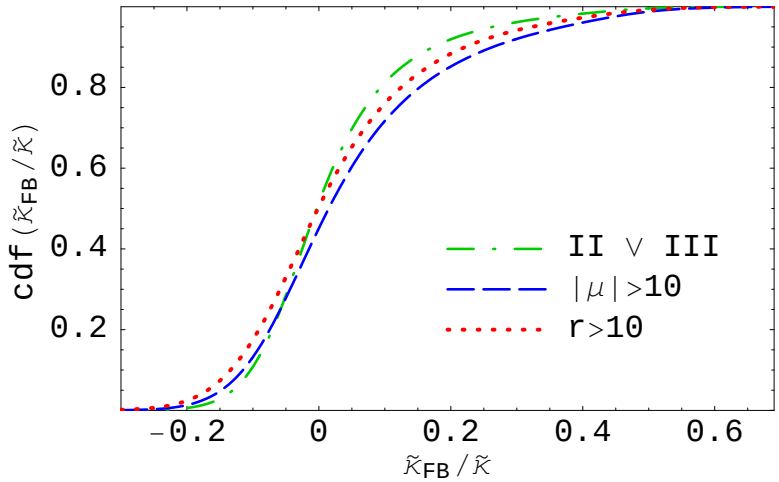

Figure 2.10: The cumulative distribution function $\mathrm{cdf}(\tilde{\kappa}_{\mathrm{FB}}/\tilde{\kappa})$ of the relative contribution $\tilde{\kappa}_{\mathrm{FB}}/\tilde{\kappa}$ of additional matter to the total LOS convergence $\tilde{\kappa}$ for strongly lensed rays and for source redshift $z^{\mathrm{S}} = 5.7$. The dash-dotted line is for rays of type II ∨ III, the dashed line for rays with $|\mu| > 10$, and the dotted line for rays with $r > 10$.

rays, we excluded the contribution of the plane containing the primary lens to isolate the contribution $\tilde{\kappa}_{\mathrm{FB}}$ of foreground and background matter to the lensing event. The cumulative distribution of the ratio of $\tilde{\kappa}_{\mathrm{FB}}$ to $\tilde{\kappa}$ is shown in Fig. 2.10. For 20 percent of the rays of type II ∨ III, additional matter along the LOS contributes more than 10 percent to the total LOS convergence. On the other hand, for 50 percent of the rays, there is a negative contribution $\tilde{\kappa}_{\mathrm{FB}}$. Although there is a noticeable fraction of strongly lensed rays whose LOS convergence is enhanced by additional matter along the LOS, there is also a noticeable fraction of strongly lensed rays whose LOS convergence is decreased due to the lack of matter along the LOS.

In Fig. 2.11, distributions of the LOS convergence for $z^{\mathrm{S}} = 5.7$ are compared for all rays and for strongly lensed rays with the primary lens contribution removed. Although the distributions are very similar, small shifts are visible. In Fig. 2.12, we show the means of these distributions as a function of source redshift z^{S}. By definition, the mean LOS convergence of all LOS should be zero. The measured mean for our whole ray sample is not exactly zero because of sampling variance,[3] but it is much smaller than the mean for strongly lensed rays with the primary lens excluded. This demonstrates a small but measurable bias towards selecting directions in which matter in front or behind the primary lens enhances the lensing. The effect increases with increasing source redshift, is weakest for the sample of rays with $r > 10$, and is strongest for $|\mu| > 10$. For $z^{\mathrm{S}} = 5.7$ and $|\mu| > 10$, where the bias is strongest, we find an average contribution of 0.04 to the LOS convergence. Hence, in all cases the bias is small in comparison with the effect of the primary lens for which $\tilde{\kappa} \sim 1$.

[3] One might naively expect the sampling variance to be negligible for the 640 million rays we shot. However, the rays were not shot independently, but are confined to forty different patches of $40h^{-1} \times 40h^{-1}\,\mathrm{Mpc}^2$ on each lens plane. The matter content of each patch is still subject to significant cosmic variance, and so, therefore, is the combined sampling area.

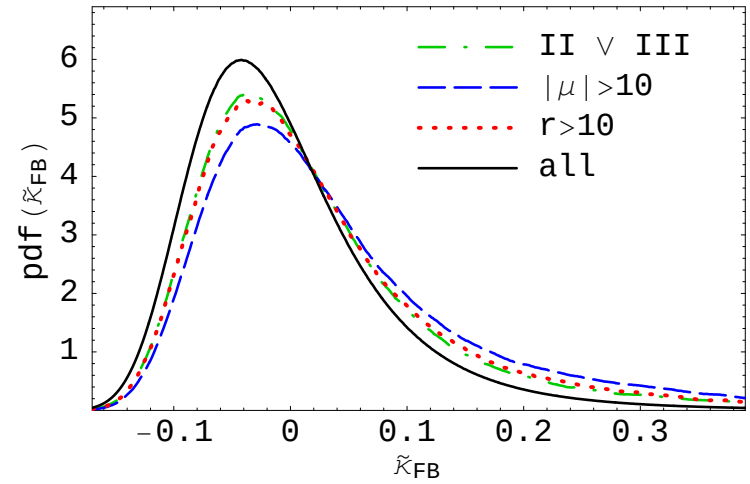

Figure 2.11: The probability density function $\mathrm{pdf}(\tilde{\kappa}_{\mathrm{FB}})$ of the LOS convergence $\tilde{\kappa}_{\mathrm{BF}}$ for strongly lensed rays and for source redshift $z^{\mathrm{S}} = 5.7$, but with the primary lens contribution excluded. The dash-dotted line is for rays of type II $\vee$ III, the dashed line for rays with $|\mu| > 10$, and the dotted line for rays with $r > 10$. For comparison, the solid line shows the corresponding distribution $\mathrm{pdf}(\tilde{\kappa})$ for all rays irrespective of their lensing properties. A small but significant shift towards larger convergence is visible in the direction of strong-lensing events.

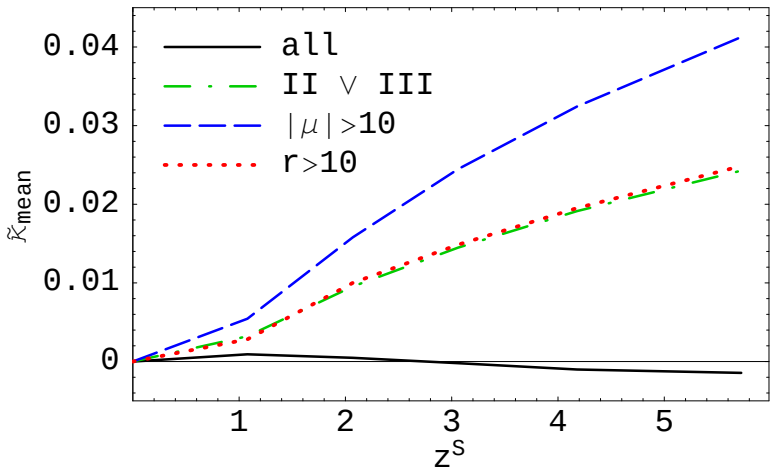

Figure 2.12: The mean $\tilde{\kappa}_{\mathrm{mean}}$ of the distributions shown in Fig. 2.11 as a function of source redshift z^{S}. The line types correspond to those of Fig. 2.11. The mean LOS convergence for all rays irrespective of their lensing properties is non-zero only because of residual sampling variance. The mean convergence from foreground and background matter along rays containing a strong lens is significantly non-zero, however, although still much smaller than the typical convergence due to the primary lens.

2.4 Summary

The aim of this work has been to study the statistical distribution of the distortion of images of distant sources due to gravitational lensing. In particular, we have concentrated on estimating the cross-section for rare strong-lensing events. Our results were obtained

by shooting random rays through a series of lens planes created from the Millennium Simulation (Springel et al. 2005). This is the largest N-body simulation of cosmological structure formation available today. We have devised improved algorithms to make the lens-planes and to calculate bending angles and shear matrices on these planes in order to take full advantage of the very large volume and the high spatial and mass resolution offered by the simulation.

In Sec. 2.3.1, we presented results for the statistical distribution of the magnification of point sources. The distribution is skewed with a peak at magnifications below unity and a tail toward high magnification. With increasing source redshift, the peak broadens and moves to lower magnifications, while the tail gains more weight. The magnification distribution affects the observed luminosity distribution of astronomical standard candles. For type Ia supernovae, perhaps the most interesting case, magnification effects on the luminosity distribution are still small for current samples compared to the intrinsic luminosity scatter, to extinction and to other effects. In future high-redshift, high-precision surveys, however, such magnification effects may cause significant systematic errors, so it will be necessary to detect and to correct for them (Dodelson and Vallinotto 2006; Munshi and Valageas 2006). In the most optimistic case, detailed comparison with predictions of the magnification distribution may help to discriminate between cosmological models.

Various optical depths connected to strong lensing were presented in Sec. 2.3.2. In particular, we estimated the fraction of images of sufficiently small sources that are highly magnified, have a large length-to-width ratio, or belong to multiply imaged sources. All the optical depths we analyse increase strongly with increasing redshift. In comparison with earlier results by, e.g., Li et al. (2005) and Wambsganss et al. (2004), we find a stronger evolution with source redshift, leading to higher optical depths for source redshifts $z^{\mathrm{S}} > 1$. We discussed possible reasons for this difference.

The results we presented in Sec. 2.3.3 show that significant contributions to the strong-lensing optical depths come from dark matter halos with masses between $10^{13}h^{-1}\,\mathrm{M}_{\odot}$ and $10^{15}h^{-1}\,\mathrm{M}_{\odot}$. The upper mass limit is due to the very rapidly decreasing abundance of more massive structures. This exponential decrease occurs at lower mass at higher redshift, and in conjunction with the lens geometry it explains why almost all lenses are at redshifts $z^{\mathrm{L}} < 2.5$, even for sources with $z^{\mathrm{S}} > 5$. The lower mass limit for strong lensing is due primarily to the small cross-sections of individual low-mass halos, although the spatial and mass resolution limits of the simulation itself and of our lens planes also play some role. Estimates based on analytic results for spherical NFW halos fit to the Millennium data suggest that these resolution effects are subdominant, and probably only reduce our total cross-sections by of order 15%. A more important effect on the relevant scales is our neglect of the baryonic mass of the central galaxies. We will come back to this in later work.

We find that the mass range over which halos can cause strong lensing extends to lower masses than those given by Li et al. (2005) and Dalal et al. (2004). This difference may in part reflect the lower resolution of the simulations used by these authors, and in part the fact that they considered extended sources with diameters ~ 0.1–$1\,\mathrm{arcsec}$, while we assumed sufficiently small sources when calculating our cross-sections. Halos

near our lower mass limit have Einstein radii of order 1 arcsec and so are inefficient in producing strongly distorted images of sources of comparable angular extent.

Since our set of lens planes represents the whole matter distribution between source and observer, we are able to quantify the influence of foreground and background matter on the frequency and the properties of strong lensing events. We find that such effects are quite modest. On average, the contribution of foreground and background material is only a few percent. Although we do find a bias towards excess foreground and background matter on strong-lensing lines-of-sight, the effect is significantly smaller than suggested by Wambsganss et al. (2005).

The most obvious extension to the work we have presented here would be ray-tracing studies of the effects of lensing for realistic distributions of source properties and across finite size fields. This will, for example, allow direct comparison with observations of massive galaxy clusters where many sets of multiple images are now detected in the best cases (Broadhurst et al. 2005; Halkola et al. 2006). When galaxy properties from galaxy formation modelling within the Millennium Simulation (e.g. Springel et al. 2005; Croton et al. 2006; Bower et al. 2006; De Lucia and Blaizot 2007) are combined with such ray-tracing analyses, it will be possible to study whether the dark halo masses of individual cluster galaxies are consistent with observation, providing an additional observational test of the hierarchical build-up of structure predicted by the standard ΛCDM model. This combination of semi-analytic simulation of galaxy formation with ray-tracing measures of lensing will also allow an estimate of how our strong-lensing cross-sections should be modified to account for the galaxies, as well as detailed studies of predictions for galaxy-galaxy lensing. We intend to come back to all these topics in future work.

Acknowledgments

We thank Volker Springel and Jeremy Blaizot for helpful discussions concerning the software development. Furthermore, we thank Ole Möller, Matthias Bartelmann, Joachim Wambsganss, Guoliang Li, and Shude Mao for helpful discussions concerning gravitational lensing. This work was supported by the DFG within the Priority Programme 1177 under the projects SCHN 342/6 and WH 6/3.

2.5 Appendix: Integral relations for the magnification

For a well behaved non-singular lens system, the numbers of images of type I, II and III of a given source satisfy $n_{\mathrm{I}} - n_{\mathrm{II}} + n_{\mathrm{III}} = 1$ (Schneider et al. 1992). Here we briefly discuss an 'integral version' of this theorem for the particular geometry used in our work: the Multiple-Plane Approximation with lens planes carrying a smooth and non-singular matter distribution that is periodic with a rectangular unit cell of dimensions $L_1 \times L_2$. In this case, the image plane and source plane can both be represented by a rectangle $\mathbb{P} = [0, L_1] \times [0, L_2]$ with periodic boundary conditions. Furthermore, the lens mapping

$$\mathcal{L} : \mathbb{P} \to \mathbb{P} : \boldsymbol{\theta} \mapsto \boldsymbol{\beta}(\boldsymbol{\theta}) = \boldsymbol{\theta} + \boldsymbol{\alpha}(\boldsymbol{\theta})$$

from image position $\boldsymbol{\theta}$ to source position $\boldsymbol{\beta}$ for a given source redshift is then smooth and non-singular with a smooth, non-singular, and periodic deflection angle $\boldsymbol{\alpha}(\boldsymbol{\theta})$. Under these conditions, the inverse signed magnification $\mu^{-1} = \det(\partial\boldsymbol{\beta}/\partial\boldsymbol{\theta})$ satisfies the following relation:

$$1 = \frac{1}{||\mathbb{P}||} \int_{\mathbb{P}} \mathrm{d}^2\boldsymbol{\theta}\ \mu^{-1}(\boldsymbol{\theta}), \tag{2.14}$$

where $||\mathbb{P}|| = L_1 L_2$ denotes the area of the rectangle $\mathbb{P}$. The following derivation employs integration by parts and exploits the smoothness and periodicity of $(\partial\boldsymbol{\beta}/\partial\boldsymbol{\theta})$:

$$\begin{aligned}
\int_{\mathbb{P}} \mathrm{d}^2\boldsymbol{\theta}\ \mu^{-1}(\boldsymbol{\theta}) &= \int_{\mathbb{P}} \mathrm{d}^2\boldsymbol{\theta}\ \det\left(\frac{\partial\boldsymbol{\beta}}{\partial\boldsymbol{\theta}}\right) \\
&= \int_0^{L_1} \mathrm{d}\theta_1 \int_0^{L_2} \mathrm{d}\theta_2\ \left(\frac{\partial\beta_1}{\partial\theta_1}\frac{\partial\beta_2}{\partial\theta_2} - \frac{\partial\beta_1}{\partial\theta_2}\frac{\partial\beta_2}{\partial\theta_1}\right) \\
&= \int_0^{L_2} \mathrm{d}\theta_2 \left(\int_0^{L_1} \mathrm{d}\theta_1\ \frac{\partial\beta_1}{\partial\theta_1}\frac{\partial\beta_2}{\partial\theta_2}\right) \\
&- \int_0^{L_1} \mathrm{d}\theta_1 \left(\int_0^{L_2} \mathrm{d}\theta_2\ \frac{\partial\beta_1}{\partial\theta_2}\frac{\partial\beta_2}{\partial\theta_1}\right) \\
&= \int_0^{L_2} \mathrm{d}\theta_2 \left(\left[\beta_1\frac{\partial\beta_2}{\partial\theta_2}\right]_{\theta_1=0}^{L_1} - \int_0^{L_1} \mathrm{d}\theta_1\ \beta_1\frac{\partial^2\beta_2}{\partial\theta_1\partial\theta_2}\right) \\
&- \int_0^{L_1} \mathrm{d}\theta_1 \left(\left[\beta_1\frac{\partial\beta_2}{\partial\theta_1}\right]_{\theta_2=0}^{L_2} - \int_0^{L_2} \mathrm{d}\theta_2\ \beta_1\frac{\partial^2\beta_2}{\partial\theta_1\partial\theta_2}\right) \\
&= \int_0^{L_2} \mathrm{d}\theta_2 \left[\beta_1\frac{\partial\beta_2}{\partial\theta_2}\right]_{\theta_1=0}^{L_1} - \int_0^{L_1} \mathrm{d}\theta_1 \left[\beta_1\frac{\partial\beta_2}{\partial\theta_1}\right]_{\theta_2=0}^{L_2} \\
&= \int_0^{L_2} \mathrm{d}\theta_2\ [\beta_1(L_1,\theta_2) - \beta_1(0,\theta_2)]\ \frac{\partial\beta_2(L_1,\theta_2)}{\partial\theta_2} \\
&- \int_0^{L_1} \mathrm{d}\theta_1\ [\beta_1(\theta_1,L_2) - \beta_1(\theta_1,0)]\ \frac{\partial\beta_2(\theta_1,L_2)}{\partial\theta_2} \\
&= \int_0^{L_2} \mathrm{d}\theta_2 L_1 \frac{\partial\beta_2(L_1,\theta_2)}{\partial\theta_2} \\
&= L_1 L_2\ .
\end{aligned}$$

For our ray sampling method, it follows directly from relation (2.14) that a representative sample of rays with random positions $\boldsymbol{\theta}_i$ $(i = 1, \ldots, N)$ in the image plane should satisfy:

$$\frac{1}{N}\sum_{i=1}^{N} \mu^{-1}(\boldsymbol{\theta}_i) \approx \frac{1}{||\mathbb{P}||} \int_{\mathbb{P}} \mathrm{d}^2\boldsymbol{\theta}\ \mu^{-1}(\boldsymbol{\theta}) = 1. \tag{2.15}$$

For our ray sample, we find that

$$\left|\frac{1}{N}\sum_{i=1}^{N} \mu^{-1}(\boldsymbol{\theta}_i)\right| - 1 < 0.003$$

for all source redshifts.

For the magnification distribution, Eq. (2.14) implies that

$$\begin{aligned}
\mathrm{pdf}^{\mathrm{S}}(\mu') &= \frac{\mathrm{d}}{\mathrm{d}\mu'} \frac{\int_{\mathbb{P}} \mathrm{d}^2\boldsymbol{\theta}\ |\mu(\boldsymbol{\theta})|^{-1}\, \Theta[\mu' - \mu(\boldsymbol{\theta})]}{\int_{\mathbb{P}} \mathrm{d}^2\boldsymbol{\theta}\ |\mu(\boldsymbol{\theta})|^{-1}} \\
&= \frac{\int_{\mathbb{P}} \mathrm{d}^2\boldsymbol{\theta}\ |\mu(\boldsymbol{\theta})|^{-1}\, \delta[\mu' - \mu(\boldsymbol{\theta})]}{\int_{\mathbb{P}} \mathrm{d}^2\boldsymbol{\theta}\ |\mu(\boldsymbol{\theta})|^{-1}} \\
&= |\mu'|^{-1} \frac{\int_{\mathbb{P}} \mathrm{d}^2\boldsymbol{\theta}\, \delta[\mu' - \mu(\boldsymbol{\theta})]}{\int_{\mathbb{P}} \mathrm{d}^2\boldsymbol{\theta}\ |\mu(\boldsymbol{\theta})|^{-1}} \\
&= \frac{\int_{\mathbb{P}} \mathrm{d}^2\boldsymbol{\theta}}{\int_{\mathbb{P}} \mathrm{d}^2\boldsymbol{\theta}\ |\mu(\boldsymbol{\theta})|^{-1}} |\mu'|^{-1} \mathrm{pdf}^{\mathrm{I}}(\mu') \\
&= \left(1 - 2\,\tau_{\mathrm{II}}^{\mathrm{S}}\right) |\mu'|^{-1} \mathrm{pdf}^{\mathrm{I}}(\mu') \ .
\end{aligned}$$

In practice, the optical depth $\tau_{\mathrm{II}}^{\mathrm{S}}$ for images with negative magnification is very small. Hence,

$$\mathrm{pdf}^{\mathrm{S}}(\mu') \approx |\mu'|^{-1} \mathrm{pdf}^{\mathrm{I}}(\mu'). \tag{2.16}$$

Employing the fact that both probability distributions are normalised, we finally find:

$$\int_{\mathbb{R}} |\mu|^{-1}\, \mathrm{pdf}^{\mathrm{I}}(\mu)\, \mathrm{d}\mu \approx 1 \ , \quad \text{and} \quad \int_{\mathbb{R}} |\mu|\, \mathrm{pdf}^{\mathrm{S}}(\mu)\, \mathrm{d}\mu \approx 1. \tag{2.17}$$

2.6 Appendix: Empty-beam magnification in a flat universe

The Jacobian of the lens mapping for light propagation through an inhomogeneous universe is given by (see, e.g., Schneider 2006a):

$$\mathbf{A}_{ij}(\boldsymbol{\theta}, w) = \delta_{ij} - \frac{2}{c^2} \int_0^w \mathrm{d}w'\, \frac{(w - w')w'}{w}\, \frac{\partial^2 \Phi(\boldsymbol{x}(\boldsymbol{\theta}, w'), w')}{\partial\theta_i\, \partial\theta_k}\, \mathbf{A}_{kj}(\boldsymbol{\theta}, w'). \tag{2.18}$$

Here, Φ denotes the three-dimensional gravitational potential, w the comoving line-of-sight distance and $\boldsymbol{\theta}$ the direction of the light ray, and $\boldsymbol{x}$ the comoving transverse separation. For an empty beam, we have $\mathbf{A} = \mathrm{diag}(\mu_{\mathrm{min}}^{-1/2}, \mu_{\mathrm{min}}^{-1/2})$. Furthermore, the Poisson equation in this case reads

$$\nabla^2 \Phi(\boldsymbol{x}(\boldsymbol{\theta}, w), w) = -\frac{3H_0^2 \Omega_{\mathrm{m}}}{2a(w)} \ ,$$

where $a(w)$ is the scale factor.

Considering now the $1,1$-component of Eq. (2.18), we find

$$\mu_{\mathrm{min}}^{-1/2}(w) = 1 + \frac{3H_0^2 \Omega_{\mathrm{m}}}{2c^2} \int_0^w \mathrm{d}w'\, \frac{(w - w')w'}{a(w')w}\, \mu_{\mathrm{min}}^{-1/2}(w') \ .$$

Differentiating this expression twice, we finally obtain the differential equation

$$\frac{\mathrm{d}^2 f}{\mathrm{d}w^2} = \frac{3H_0^2\Omega_\mathrm{m}}{2c^2}\,\frac{f(w)}{a(w)}\,,$$

where $f(w) \equiv w\mu_\mathrm{min}^{-1/2}(w)$. This ordinary differential equation can be easily solved numerically.

3 Strong lensing optical depths in a ΛCDM universe II: The influence of the stellar mass in galaxies

Stefan Hilbert, Simon D.M. White, Jan Hartlap, and Peter Schneider, 2008: MNRAS (in press)

Abstract

We investigate how strong gravitational lensing in the concordance ΛCDM cosmology is affected by the stellar mass in galaxies. We extend our previous studies, based on ray-tracing through the Millennium Simulation, by including the stellar components predicted by galaxy formation models. We find that the inclusion of these components greatly enhances the probability for strong lensing compared to a 'dark matter only' universe. The identification of the 'lenses' associated with strong-lensing events reveals that the stellar mass of galaxies (i) significantly enhances the strong-lensing cross-sections of group and cluster halos, and (ii) gives rise to strong lensing in smaller halos, which would not produce noticeable effects in the absence of the stars. Even if we consider only image splittings $\gtrsim 10\,\mathrm{arcsec}$, the luminous matter can enhance the strong-lensing optical depths by up to a factor of 2.

Key words: gravitational lensing – dark matter – large-scale structure of the Universe – galaxies: general – cosmology: theory – methods: numerical

3.1 Introduction

The ΛCDM model, the current standard model of cosmological structure formation, is based on a flat universe with cold dark matter and a cosmological constant. It has been shown to fit a wide range of observations, including the properties of galaxies, their clustering, the accelerated expansion inferred from the apparent luminosity of distant type Ia supernovae, the structure of the high-redshift intergalactic medium, and temperature fluctuations in the cosmic microwave background (Spergel et al. 2007).

Further tests and constraints on the parameters of the ΛCDM model are obtained from measurements of gravitational-lensing effects, which were first discovered through multiple images of distant quasars (Walsh et al. 1979) and highly distorted images of distant galaxies at optical (Lynds and Petrosian 1986; Soucail et al. 1987) and radio (Hewitt et al. 1988) wavelengths. Many recent observations of gravitational-lensing effects around galaxies (e.g. Mandelbaum et al. 2006b; Simon et al. 2007), and in and around galaxy clusters (e.g. Mandelbaum et al. 2006a; Clowe et al. 2006; Natarajan et al. 2007;

Comerford et al. 2006; Massey et al. 2007a) are well explained by the dark-matter structures predicted from the ΛCDM model. Surveys measuring the weak lensing effects of the matter distribution as a whole (e.g. Semboloni et al. 2006; Hoekstra et al. 2006; Simon et al. 2007; Massey et al. 2007b; Benjamin et al. 2007) are particularly promising for further constraining the parameters of the ΛCDM model. An open question is whether the observed frequency of giant arcs (Luppino et al. 1999; Zaritsky and Gonzalez 2003; Gladders et al. 2003) is consistent with predictions based on the ΛCDM model with parameters favoured by other observations (e.g. Bartelmann et al. 1998; Oguri et al. 2003; Dalal et al. 2004; Wambsganss et al. 2004; Li et al. 2006; Meneghetti et al. 2007).

The efforts currently underway to improve the measurement of lensing effects need to be matched by a comparable improvement in the theoretical predictions. According to the ΛCDM model, most of the matter in our Universe is dark. The baryonic matter contributes significantly, however, to the inner regions of galaxies and clusters, which is where strong lensing is observed. Most theoretical studies of strong lensing by galaxies (e.g. Turner et al. 1984; Maoz and Rix 1993; Möller and Blain 2001; Huterer et al. 2005; Oguri 2006; Chae 2007; Möller et al. 2007; Oguri et al. 2008) use analytic profiles to model both the luminous and the dark components of the lenses. Many studies of strong lensing by galaxy clusters use profiles obtained from N-body simulations for the dark matter, but neglect the luminous matter (e.g. Bartelmann et al. 1998; Wambsganss et al. 2004; Li et al. 2006). There are, however, also studies of the effect of galaxies on giant-arc probabilities in clusters. Meneghetti et al. (2000), for example, placed galaxies randomly into simulated dark-matter clusters and concluded that, although the galaxies change certain aspects of cluster lensing, they do not have a strong effect on the formation of giant arcs. Meneghetti et al. (2003) and Dalal et al. (2004) studied the effect of a large central galaxy in a cluster, and found that even a very massive central galaxy does not greatly affect the cross-section for giant arcs.

Puchwein et al. (2005) and Rozo et al. (2006) incorporated a treatment of the baryonic component into cluster-formation simulations and studied its influence on giant-arc probabilities. Such simulations currently have difficulty producing a galaxy population which matches observation, so their results are not simple to interpret. Until this problem is overcome, a hybrid approach that embeds a semi-analytic treatment of galaxy formation within an N-body simulation of dark-matter evolution (Springel et al. 2001, 2005) appears the most realistic way to address these issues.

In earlier work (Hilbert et al. 2007b, paper I in the following), we studied the statistics of strong lensing by shooting random rays through a series of lens planes created from the Millennium Simulation (Springel et al. 2005). This very large N-body simulation of cosmological structure formation did not explicitly include gas physics such as radiative cooling and star formation, and the results presented in paper I did not account for the effects of the stellar components of galaxies.

In this paper, we extend the work of paper I to include the gravitational effects of the stars in galaxies, as inferred from semi-analytic galaxy-formation models implemented within the evolving dark-matter distribution of the Millennium Simulation (Springel et al. 2005; Croton et al. 2006; De Lucia et al. 2006; De Lucia and Blaizot 2007). These models, which have been adjusted to be consistent with a large number of observations, couple star formation in the galaxies directly to the properties of the underlying dark

matter. They currently provide the most accurate way to simulate how the dark-matter distribution is populated with galaxies.

The Millennium Simulation has higher resolution and a much larger volume than simulations used in previous studies of the effects of galaxies on strong lensing. On scales above the resolution limit, the simulation provides a more realistic matter distribution than analytic models. Furthermore, the galaxy model we use provides the stellar mass of the galaxies as well as their positions with respect to the dark matter in the simulation, which is a considerable improvement over the simpler recipes used to place galaxies into dark-matter halos in previous work (e.g. by Meneghetti et al. 2000, 2003; Dalal et al. 2004). Thus we hope to obtain more accurate results, particularly in those regions where both the luminous and the dark matter are important for lensing. This includes the inner few arcseconds of most lenses, regions which dominate many surveys for strong lensing (Myers et al. 2003; Oguri et al. 2006; Bolton et al. 2006; Willis et al. 2006; Cabanac et al. 2007).

Our paper is organised as follows. In Sec. 3.2, we summarise the main aspects of our method for shooting a representative ray sample through the Millennium Simulation, and we describe how we incorporate the lensing effects of the stellar mass in galaxies. In Sec. 3.3, we present results for the magnification distribution, for strong-lensing optical depths, and for lensing cross-sections as a function of lens halo mass and projected distance between lens centre and image. In particular, we compare the results obtained for dark matter alone to those obtained when the stellar mass of galaxies is also included. The paper concludes with a summary and outlook in Sec. 3.4.

3.2 Simulation methods

Our approach for simulating gravitational lensing closely follows that of paper I. The reader is referred to that paper for a detailed description. Here, we summarise the main aspects of the method and discuss the extensions needed for the present work.

In order to calculate image distortions resulting from the gravitational deflection of light by matter inhomogeneities between the source and the observer, we use a Multiple-Lens-Plane algorithm (e.g. Blandford and Narayan 1986; Schneider et al. 1992; Seitz et al. 1994; Jain et al. 2000). Lens planes are introduced transverse to the line-of-sight, and matter inhomogeneities in the observer's backward light cone are projected onto them. Light rays are traced back from the observer to their source under the assumption that the rays propagate unperturbed between lens planes, but are deflected when passing through a plane. The ray distortions (more precisely, the distortions of infinitesimally thin ray bundles) induced by the lens planes are calculated from the projected matter distribution on the planes.

3.2.1 The dark-matter contribution

We use the particle data of the of the Millennium Simulation (Springel et al. 2005) to generate the dark-matter distribution on the lens planes. The Millennium Simulation assumes a flat ΛCDM universe with a matter density of $\Omega_{\rm M} = 0.25$ in terms of the critical density, a cosmological constant with $\Omega_\Lambda = 0.75$, a Hubble constant $100h\,\mathrm{kms}^{-1}\mathrm{Mpc}^{-1}$

with $h = 0.73$, a primordial spectral index $n = 1$ and a normalisation parameter $\sigma_8 = 0.9$ for the linear density power spectrum. The simulation followed 10^{10} particles of mass $m_\mathrm{p} = 8.6 \times 10^8 h^{-1}\,\mathrm{M}_\odot$ in a cubic region of side length $L = 500h^{-1}\,\mathrm{Mpc}$ comoving from redshift $z = 127$ to $z = 0$. The effective resolution reached near the centres of dark-matter halos is comparable to the comoving force-softening length of $5h^{-1}\,\mathrm{kpc}$. During the run, 64 snapshots of the simulation were taken and stored on disk.

Along the line-of-sight, we place one plane for each snapshot at the corresponding distance from the observer, resulting in 44 planes for sources at redshift $z^\mathrm{S} = 5.7$ (the highest redshift we consider). For each lens plane, the particles within an oblique slice of appropriate thickness through the corresponding snapshot are projected onto a hierarchy of meshes (with a spacing of $2.5h^{-1}\,\mathrm{kpc}$ comoving for the finest mesh). The projected matter distribution is smoothed by an adaptive scheme to reduce shot noise from individual particles while retaining a resolution of about $5h^{-1}\,\mathrm{kpc}$ comoving in dense regions. Fast-Fourier-Transform (FFT) methods (Frigo and Johnson 2005) are employed to calculate the dark-matter lensing potential from the projected particle distribution on the planes. The second derivatives of the potential, which quantify the dark-matter contribution to the distortion of light rays passing through the lens planes, are calculated by finite difference and bilinear interpolation.

3.2.2 The stellar contribution

The Millennium Simulation did not explicitly simulate the physics of star formation. Rather this was done in post-processing by applying several semi-analytic models to halo merger trees generated from the stored output in order to follow the formation and evolution of the galaxies. In this paper we use the catalogue made publicly available by Lemson and the Virgo Consortium (2006)[1] based on the model by De Lucia and Blaizot (2007) to obtain the main properties of the galaxies. Besides many other quantities, the catalogue provides the positions, stellar disc and bulge[2] masses, and disc radii. Here, we restrict our analysis to galaxies with $M_\mathrm{stellar} \geq 10^9 h^{-1}\mathrm{M}_\odot$, which we project onto the same set of lens planes as the simulation particles. As a test, we also tried a higher mass limit $M_\mathrm{stellar} \geq 10^{10} h^{-1}\mathrm{M}_\odot$, finding rather minor changes. Clearly our adopted limit is quite sufficient to include all significant lenses, at least according to this model.

For each galaxy, we approximate the projected matter distribution of the disc component by an exponential surface-density profile with comoving scale radius $r_\mathrm{s\,disc}$ and total mass M_disc taken from the galaxy catalogue data:[3]

$$\Sigma_\mathrm{disc}(r) = \frac{M_\mathrm{disc}}{2\pi r_\mathrm{s\,disc}^2} \exp\left(-\frac{r}{r_\mathrm{s\,disc}}\right). \tag{3.1}$$

Here, $\Sigma_\mathrm{disc}(r)$ denotes the comoving surface mass density at projected comoving distance r on the lens plane.

[1] http://www.mpa-garching.mpg.de/Millennium

[2] Here, 'bulge' means the spheroidal stellar component of a galaxy, e.g., the stellar bulge of a disc galaxy or the all stars in an elliptical galaxy with no disc.

[3] The catalogue does not contain M_disc and $r_\mathrm{s\,disc}$ explicitly, but provides the total stellar mass M_stellar, the stellar-bulge mass M_bulge, the physical disc radius R_disc, and the redshift z. According to the underlying galaxy-formation model, $M_\mathrm{disc} = M_\mathrm{stellar} - M_\mathrm{bulge}$ and $r_\mathrm{s\,disc} = R_\mathrm{disc}(1+z)/3$.

The galaxy model of De Lucia and Blaizot (2007) provides bulge masses $M_{\rm bulge}$, but not the bulge radii. We thus use an empirical relation to calculate the bulge radii from the bulge masses. Shen et al. (2003)[4] studied the size distribution of 140 000 galaxies in the Sloan Digital Sky Survey (SDSS) and found a relation $\bar{R}_{\rm e} \propto M_{\rm stellar}^{0.56}$ between the median physical effective radius $\bar{R}_{\rm e}$ and stellar mass $M_{\rm stellar}$ of early-type galaxies at redshift $z \lesssim 0.3$. Trujillo et al. (2006) combined results of SDSS, GEMS, and FIRES to study the evolution of galaxy sizes between redshift $z = 0$ and $z \approx 3$, and found $R_{\rm e} \propto (1+z)^{-0.45}$ for the mean radius $R_{\rm e}$ of early types at fixed stellar mass. For the effective bulge radius $r_{\rm e\,bulge}$ (measured in comoving units), we combine these relations into:

$$r_{\rm e\,bulge} = (1+z)^{0.55} \left(\frac{M_{\rm bulge}}{10^{10} h^{-1}\,{\rm M}_\odot} \right)^{0.56} \times 0.54 h^{-1}\,{\rm kpc}. \tag{3.2}$$

The bulge component of each galaxy is then approximated by a spherical de-Vaucouleurs profile (de Vaucouleurs 1948):

$$\Sigma_{\rm bulge}(r) = \frac{94.5 M_{\rm bulge}}{r_{\rm e\,bulge}^2} \exp\left[-7.67 \left(\frac{r}{r_{\rm e\,bulge}} \right)^{1/4} \right]. \tag{3.3}$$

Here, $\Sigma_{\rm bulge}(r)$ denotes the projected bulge surface mass density at projected comoving radius r.

For each galaxy, we use analytic expressions to calculate the ray distortions induced by the mass distributions (3.1) and (3.3) (see, e.g., Cardone 2004). The disc and bulge contributions of all galaxies on the lens plane are then summed to obtain the stellar contribution to the distortion of light rays passing through the plane.

The profile (3.1) for the disc component closely follows the projected mass distribution of a stellar disc seen face-on. This, of course, neglects the effects of disc inclination with respect to the line-of-sight, which on average increases the cross-section for strong lensing by isolated disc galaxies (e.g. Wang and Turner 1997; Möller and Blain 1998). Similarly, the model (3.3) for the bulge neglects ellipticity. Furthermore, recent observations (Trujillo et al. 2007) indicate a stronger evolution of galaxy size with redshift for very massive galaxies, leading to smaller radii for spheroid-like galaxies with $M_{\rm stellar} > 10^{11}\,{\rm M}_\odot$ at redshifts $z \gtrsim 1$ than our estimate (3.2). Thus our model for the stellar component of galaxies may be inaccurate for strong lensing occurring close to the centres of galaxies. For strong lensing at distances of several effective radii, however, the details of the stellar matter distribution do not influence the lensing properties very strongly.

To test the dependence of our results on the particular choice of the mass profile for the stars in galaxies, we replaced the de-Vaucouleurs profile (3.3) by a Hernquist profile (Hernquist 1990), and by a Plummer profile with $\Sigma_{\rm bulge}(r) \propto (r_{\rm e\,bulge}^2 + r^2)^{-2}$ and the same effective radius $r_{\rm e\,bulge}$. For 'cuspy' de-Vaucouleurs and Hernquist profiles, the optical depths and cross-sections for strong lensing by both dark and luminous matter agree within $\sim 20\%$, whereas the results for the 'cored' Plummer profile were noticeably smaller. Hence, our results are not very sensitive to the details of stellar mass distribution as long as we use cuspy profiles for the spheroid stellar component of the galaxies.

[4] See also Shen et al. (2007) for an Erratum.

The particles in the Millennium Simulation are treated as collisionless particles by the simulation and are used in our calculations to obtain the dark-matter distribution on the lens planes, but they represent the *total* mass in the simulated part of the universe. One could argue that the stellar mass we add to the lens planes should be removed somewhere else to balance the mass budget. Here, we refrain from doing this for two main reasons: (i) The mass in stars (1% of the total mass at $z = 0$) is small compared to the mass in collapsed objects (50% at $z = 0$). (ii) Although the baryons that produce the stars originate from within the halos around the galaxies, gas physics increases the dark-matter density in the inner part of the halos compared to collisionless simulations (e.g. Barnes and White 1984; Blumenthal et al. 1986; Gnedin et al. 2004). Only in the halo outskirts, which are not relevant for strong lensing, is there a net decrease of the matter density. The effects of the baryons on the dark-matter profile and their relevance for lensing (see, e.g., Puchwein et al. 2005; Jing et al. 2006; Rozo et al. 2006; Wambsganss et al. 2008) are not the primary focus of this work, so we neglect these effects in the following.

3.2.3 Sampling image distortions

The light rays traced back from the observer through the lens planes to their source define the lens mapping $\boldsymbol{\theta} \mapsto \boldsymbol{\beta}$, which relates the 'observed' angular position $\boldsymbol{\theta}$ of a ray in the image plane $\mathbb{P}^{\mathrm{I}}$ to the 'true' angular position $\boldsymbol{\beta}$ of its source in source plane $\mathbb{P}^{\mathrm{S}}$ at a given redshift z^{S}. The distortion matrix $\mathbf{A} = (\partial\boldsymbol{\beta}/\partial\boldsymbol{\theta})$, i.e. the Jacobian of the lens mapping, can be calculated from the distortions that the ray bundles experience when passing through the lens planes.

For sufficiently small sources, the distortion matrix quantifies the image distortions induced by the deflections. In this case, the image magnification μ is given by $\mu = (\det \mathbf{A})^{-1}$, and the eigenvalues λ_1 and λ_2 of $\mathbf{A}$ (w.l.o.g. $|\lambda_1| > |\lambda_2|$) determine the major-to-minor axis ratio $r = |\lambda_1|/|\lambda_2|$ of the elliptical images of circular sources (Schneider et al. 1992).

To quantify the frequency of images with a given property p, e.g. a large magnification or large length-to-width ratio, we define the optical depths

$$\tau_p^{\mathrm{I}} = \frac{\int_{\mathbb{P}^{\mathrm{I}}} \mathrm{d}^2\boldsymbol{\theta}\, 1_p(\boldsymbol{\theta})}{\int_{\mathbb{P}^{\mathrm{I}}} \mathrm{d}^2\boldsymbol{\theta}} \tag{3.4}$$

and

$$\tau_p^{\mathrm{S}} = \frac{\int_{\mathbb{P}^{\mathrm{I}}} \mathrm{d}^2\boldsymbol{\theta}\; |\mu(\boldsymbol{\theta})|^{-1}\, 1_p(\boldsymbol{\theta})}{\int_{\mathbb{P}^{\mathrm{I}}} \mathrm{d}^2\boldsymbol{\theta}\; |\mu(\boldsymbol{\theta})|^{-1}}, \tag{3.5}$$

where $1_p(\boldsymbol{\theta}) = 1$ if the image at position $\boldsymbol{\theta}$ has property p, and $1_p(\boldsymbol{\theta}) = 0$ otherwise. For volume-limited surveys, τ_p^{I} estimates the fraction of images with property p assuming a uniform distribution of images in the image plane, whereas τ_p^{S} estimates the fraction of images with property p assuming a uniform distribution of sources in the source plane.

In order to estimate these optical depths, the dark-matter and the stellar contributions to the distortion are calculated at 160 million randomly chosen positions on each lens plane. For every considered source redshift, the distortions from all lens planes with

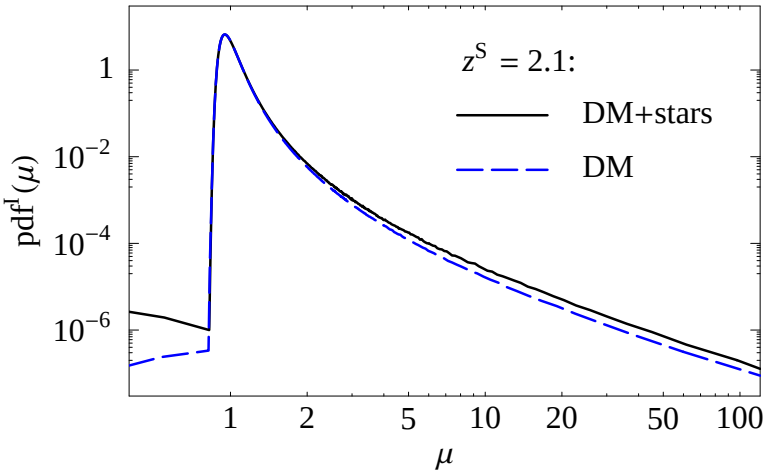

Figure 3.1: The probability density $\mathrm{pdf}^{\mathrm{I}}(\mu)$ of the magnification μ for sources at redshift $z^{\mathrm{S}} = 2.1$. The case of lensing by dark and luminous matter (solid line) is compared to the case of dark matter alone (dashed line).

smaller redshift are combined at random to generate the distortion matrices for rays along 1.6×10^8 random lines-of-sight. Combining the distortions from different lens planes at random saves us from computing the actual path of light rays, while it allows us to sample the image distortions on a very large area under the assumption that the mass distribution projected on different lens planes is uncorrelated.

The measured fraction of rays with a certain property, e.g. a large magnification, is then used as a Monte-Carlo estimate for the corresponding optical depth τ^{I} to the chosen source redshift. The optical depth τ^{S} is obtained by additionally weighting all rays by their inverse magnification. For comparison purposes, we repeat the procedure using the dark-matter contribution alone, and using the stellar contribution alone.

3.3 Results

3.3.1 The magnification distribution

By binning the magnifications of our random rays, we estimated the probability density function

$$\mathrm{pdf}^{\mathrm{I}}(\mu') = \frac{\mathrm{d}}{\mathrm{d}\mu'} \tau^{\mathrm{I}}_{\mu(\boldsymbol{\theta}) \leq \mu'}. \tag{3.6}$$

In Fig. 3.1, the distribution including the stellar contribution is compared with the dark-matter only distribution for sources at redshift $z^{\mathrm{S}} = 2.1$. There is little difference between the two distributions at magnifications $\mu \approx 1$. Only in the high-μ tail (containing the strongly focused rays) and for very low μ (containing the overfocused rays) do the two distributions differ significantly. The increased pdf at high magnifications hints at a higher optical depth for large magnifications when the effects of the luminous matter are included. Qualitatively the same behaviour is found for all considered source redshifts.

3.3.2 Strong-lensing optical depths

From our ray sample, we calculate

- the fraction of rays with $\det \mathbf{A} < 0$ (called type II),
- the fraction with $\det \mathbf{A} > 0$ and $\mathrm{tr}\, \mathbf{A} < 0$ (type III),
- the fraction with $\det \mathbf{A} < 0$ or $\mathrm{tr}\, \mathbf{A} < 0$, i.e. the sum of the two previous classes (type II $\vee$ III)[5],
- the fraction with a length-to-width ratio $r > 10$ for images of sufficiently small circular sources, and
- the fraction with magnification $|\mu| > 10$.

The corresponding optical depths $\tau_p^{\mathrm{I}}(z^{\mathrm{S}})$ and $\tau_p^{\mathrm{S}}(z^{\mathrm{S}})$ are plotted in Fig. 3.2 as functions of the source redshift z^{S}. The optical depths that account for the stellar mass in galaxies are significantly larger than those which neglect it. The effect is particularly large at low source redshifts, where the dark matter alone is much less efficient in producing strong lensing. In contrast to lensing by dark matter alone, the optical depths for $|\mu| > 10$ and $r > 10$ are quite similar when the luminous matter is included, the optical depth $\tau_{\mathrm{II}}^{\mathrm{S}}$ for images of type II is no longer much smaller than $\tau_{\mathrm{II}}^{\mathrm{I}}$, and the optical depth $\tau_{\mathrm{III}}^{\mathrm{S}}$ is even larger than $\tau_{\mathrm{III}}^{\mathrm{I}}$. This implies that most images of type III are strongly demagnified. These are the images of multiply imaged sources that often remain undetected in observations because they are demagnified and close to the bright centre of the lens galaxy.

The optical depths for joint lensing by luminous and dark matter show similar behaviour to cored isothermal spheres. For singular isothermal spheres, one of the two eigenvalues of the distortion matrix $\mathbf{A}$ is unity (Schneider et al. 1992). Hence, $|\mu| = r$, and the cross-sections for $r > 10$ and $|\mu| > 10$ are equal. Singular isothermal spheres do not produce images of type III. If the central singularity is replaced by a small core, the lens acquires a finite cross-section for strongly demagnified images of type III, and the cross-sections for $r > 10$ and $|\mu| > 10$ separate slightly. Thus, the addition of baryons apparently makes the mass profiles of strong lenses resemble isothermal spheres with small cores.

3.3.3 Lens properties

As discussed in paper I for lensing by dark matter alone, the properties of most strongly lensed rays, i.e. rays with $\det \mathbf{A} < 0$, $\mathrm{tr}\, \mathbf{A} < 0$, $|\mu| > 10$, or $r > 10$, are predominantly caused by a single matter clump along the line of sight. This is equally the case if galactic baryons are included as lensing material. In order to find these matter clumps, which we refer to as the lenses of the rays, we use the method described in paper I: We determine for each strongly lensed ray the lens plane that is sufficient to produce the

[5] In all situations relevant for this work, images of type II and III, and hence all images of type II $\vee$ III, belong to sources with multiple images.

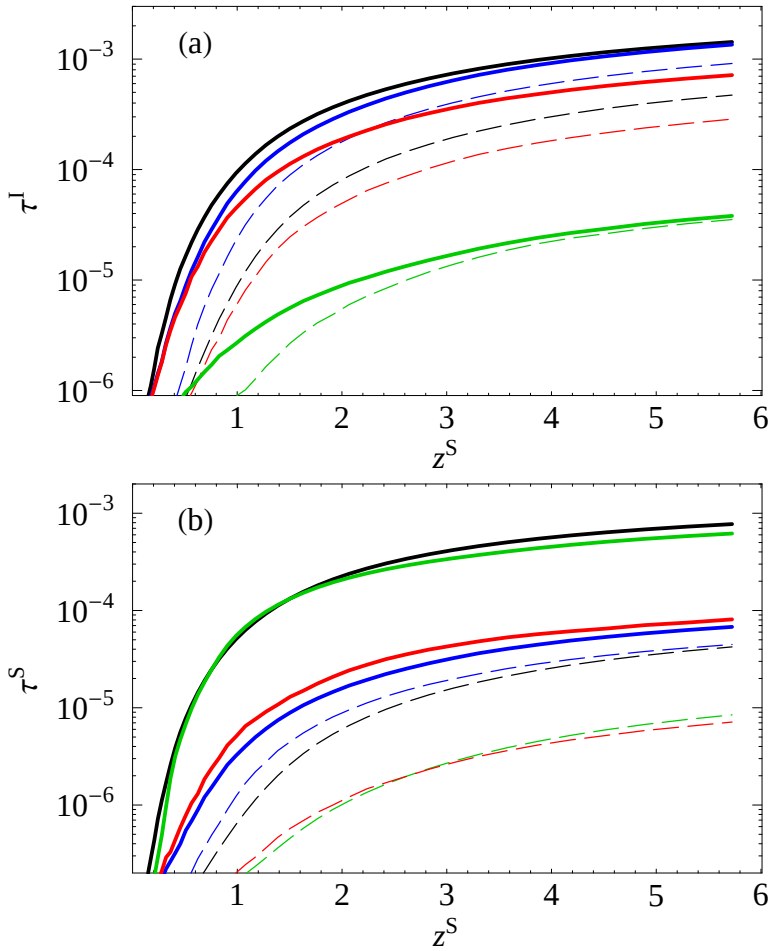

Figure 3.2: Comparison between the optical depths caused by dark and luminous matter (solid lines) and the optical depths caused by dark matter alone (dashed lines), either assuming a uniform distribution of images in the image plane (a), or a uniform distribution of sources in the source plane (b). Shown are optical depths for images of small circular sources of type II (black lines), of type III (green), with large magnification (blue) and with large length-to-width ratio (red).

relevant property in the single-plane approximation. Depending on source redshift and the property considered, this simple criterion identifies exactly one lens plane for at least 60% (usually $> 80\%$) of the rays. The redshift of this plane is taken as the lens redshift z^{L} for the ray.

The resulting lens redshift distribution for rays of type II$\vee$III is illustrated in Fig. 3.3, where the cross-section $\partial\tau^{\mathrm{I}}_{\mathrm{II}\vee\mathrm{III}}/\partial z^{\mathrm{L}}$ is plotted as a function of lens redshift z^{L} for various source redshifts z^{S}. (Not shown are the lens redshift distributions for rays with $|\mu| > 10$ and with $r > 10$, but these are very similar.) The inclusion of the stellar mass slightly increases the typical redshift of lenses (cf. fig. 4 in paper I), but most of the lenses still have $z^{\mathrm{L}} < 2.5$ even for high source redshifts. The lack of lenses at high redshift reflects the lower abundance of massive galaxies and halos, as well as the less

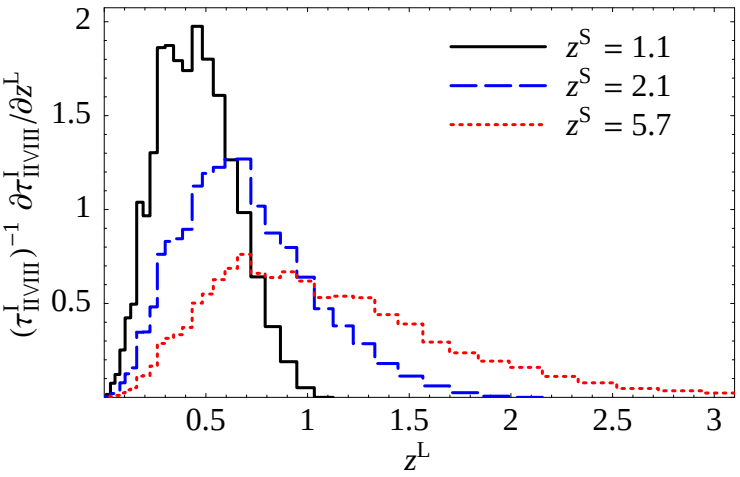

Figure 3.3: The cross-section $\partial\tau^{\rm I}_{\rm II}\vee{\rm III}/\partial z^{\rm L}$ for rays of type II$\vee$III as a function of lens redshift $z^{\rm L}$ for sources at redshift $z^{\rm S}=1.1$ (solid line), $z^{\rm S}=2.1$ (dashed line), and $z^{\rm S}=5.7$ (dotted line) considering lensing by both dark and luminous matter.

favourable geometry for lensing at these redshifts.

Following the method in paper I, we identify for each strongly lensed ray the dark-matter halo[6] associated with the lens by locating on the sufficient plane the halo with the highest ratio M/b of its virial mass M (defined as the mass within a sphere with mean enclosed density 200 times the cosmological mean) to the projected distance b of its centre from the position where the ray intersects the plane. The resulting distributions of halo masses for rays of type II $\vee$ III, with $|\mu|>10$, and with $r>10$ are compared in Fig. 3.4a, where the cross-sections $\partial\tau^{\rm I}/\partial\log M^{\rm L}$ are shown for $z^{\rm S}=5.7$ as a function of lens halo mass $M^{\rm L}$. For $M^{\rm L}>10^{14}h^{-1}\,{\rm M}_\odot$, the cross-sections increase by at most 40% when the effects of the galaxies are included. For $M^{\rm L}<10^{14}h^{-1}\,{\rm M}_\odot$, the difference is much larger, however. In particular, the mass distribution of strongly lensing halos extends to significantly lower values when the galaxies are included (see Fig. 3.4b). There is both a maximum at masses $M^{\rm L}\approx 3\times10^{13}h^{-1}\,{\rm M}_\odot$ and a low-mass 'tail'.

For lower source redshifts $z^{\rm S}=1.1$, there is both a low-mass 'tail' and a maximum at masses $M^{\rm L}\approx10^{14}h^{-1}\,{\rm M}_\odot$ for rays with $|\mu|>10$ (see Fig. 3.5). For rays with $r>10$ and rays of II $\vee$ III, the distribution becomes bimodal with an additional maximum at $M^{\rm L}\approx2\times10^{12}h^{-1}\,{\rm M}_\odot$.

As can be seen in Fig. 3.4a, $\partial\tau^{\rm I}_{r>10}/\partial\log M^{\rm L}$ and $\partial\tau^{\rm I}_{|\mu|>10}/\partial\log M^{\rm L}$ are very similar for $M^{\rm L}\lesssim10^{12}h^{-1}\,{\rm M}_\odot$. Strong lenses with these masses clearly show the lensing characteristics of isothermal spheres. Lenses with masses $M^{\rm L}\gtrsim10^{13}h^{-1}\,{\rm M}_\odot$, however, have much smaller cross-sections for $r>10$ than for $|\mu|>10$, which can be interpreted as 'convergence-dominated' lensing, with shear being much less important than convergence.

For halos with mass $M^{\rm L}<10^{13}h^{-1}\,{\rm M}_\odot$, the dark matter alone is unable to produce strong lensing. However, the stellar mass of the galaxies changes this. As can

[6]The dark-matter halos considered here were identified in the simulation by applying a friend-of-friend group-finding algorithm to the dark-matter particle distribution.

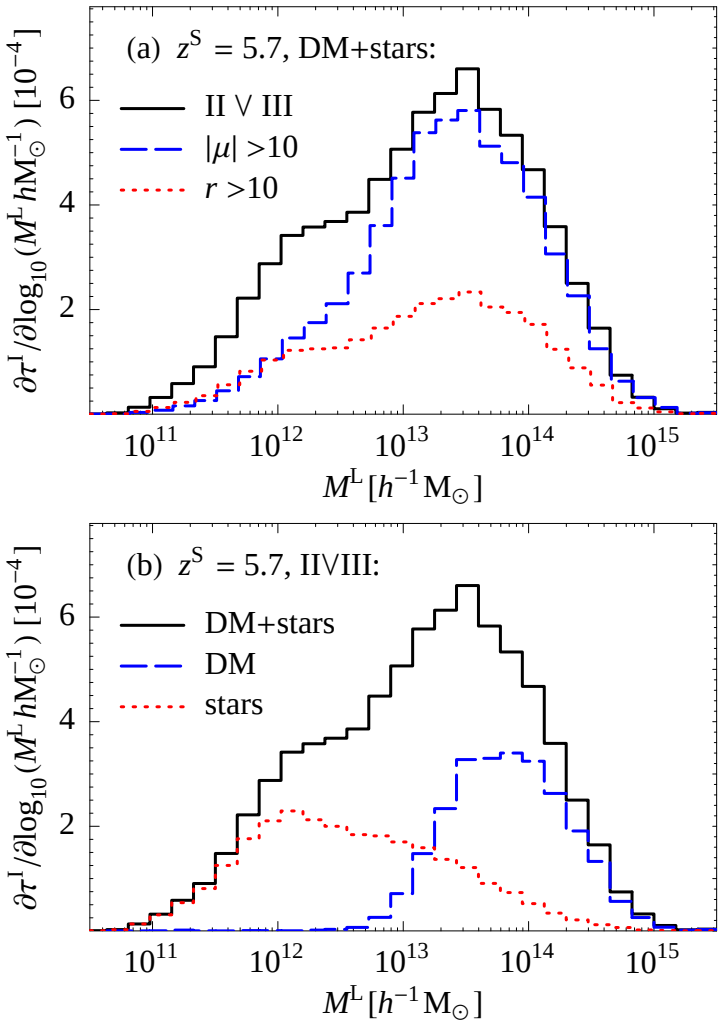

Figure 3.4: The cross-section $\partial\tau^{\mathrm{I}}/\partial \log M^{\mathrm{L}}$ as a function of the lens halo mass M^{L} (see text) for sources at redshift $z^{\mathrm{S}} = 5.7$. Panel (a) compares rays of type II $\vee$ III (solid line), rays with $|\mu| > 10$ (dashed line), and rays with $|r| > 10$ (dotted line) for lensing by both dark and luminous matter. (b) compares rays of type II $\vee$ III for lensing by both dark and luminous matter (solid line), for lensing by dark matter alone (dashed line), and for lensing by luminous matter alone (dotted line).

be seen in Fig. 3.4b, the cross-section is maximal for $M^{\mathrm{L}} \approx 10^{12} h^{-1}\,\mathrm{M}_\odot$ if *only* the *stellar* mass is considered. Even though such galaxies typically have stellar masses $M_{\mathrm{stellar}} < 10^{11} h^{-1}\,\mathrm{M}_\odot$, and Einstein radii $r_{\mathrm{E}} \lesssim 1\,\mathrm{arcsec}$, their high abundance apparently outweighs the small cross-sections of individual galaxies. Note that galaxies with such small Einstein radii produce strong lensing in our simulation because we use analytic expressions for the stellar contribution to the light deflection, which are not subject to the (larger) resolution limit of the meshes used for the the dark-matter contribution.

The cross-sections for strong lensing by both dark and luminous matter shown in Fig. 3.4a decrease rapidly for $M^{\mathrm{L}} < 10^{12} h^{-1}\,\mathrm{M}_\odot$ and vanish for $M^{\mathrm{L}} < 5 \times 10^{10} h^{-1}\,\mathrm{M}_\odot$.

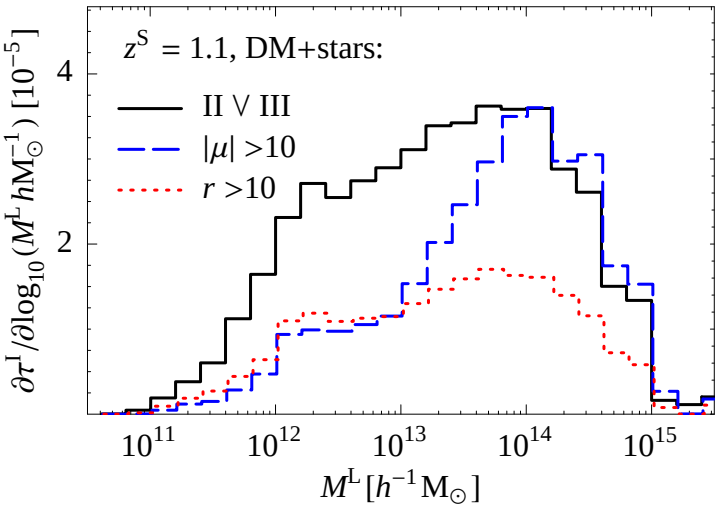

Figure 3.5: The cross-section $\partial\tau^I/\partial\log M^L$ as a function of the lens halo mass M^L for sources at redshift $z^S = 1.1$. Compared are the rays of type II∨III (solid line), rays with $|\mu| > 10$ (dashed line), and rays with $|r| > 10$ (dotted line) for lensing by both dark and luminous matter.

Apparently, halos with $M < 5 \times 10^{10} h^{-1}\,M_\odot$ do not contribute to strong lensing even when the baryons in stars are taken into account.

3.3.4 Images at larger radii

The inclusion of the stellar mass in galaxies greatly increases the optical depths for strong lensing. As discussed in the preceding section, a large part of the increase can be traced back to galaxies that have small Einstein radii $r_E \lesssim 1$ arcsec and hence produce only small image splittings. This suggests that the effects of the luminous matter on the optical depths is smaller for larger image splittings.

To measure the impact parameter of a strongly lensed ray with respect to the lens centre – and thus obtain an estimate for the expected image splitting – we now consider the dark-matter subhalos[7] and – in the case of lensing by both luminous and dark matter – the galaxies[8] as individual lens candidates. For each strongly lensed ray, we identify the galaxy or dark-matter subhalo on the 'sufficient' plane that has the largest ratio M/b^2 of its mass M and the square of the projected distance between its centre and the ray. This ratio compares the impact parameter b to the Einstein radius $r_E \propto \sqrt{M}$ of the lens candidate under the simplifying assumption of a point mass.[9]

[7] as identified by SUBFIND (Springel et al. 2001)

[8] with their stars and their associated dark-matter subhalo (if there is one)

[9] Strongly lensed rays at larger impact parameters w.r.t. the halo centre are often lensed by substructure, which produce image splittings much smaller than the distance from the halo centre. The number of strongly lensed rays at large impact parameters w.r.t. the halo centre is therefore rather a measure of the amount of substructure present in dark-matter halos than a measure for large image splittings. If we identify the mass with the largest ratio M/b as lens (as in the previous section), too often a cluster main halo is selected, although the lensing is due to a smaller non-central galaxy in that cluster (as is revealed by inspection of individual cases). For M/b^2, this problem does not occur.

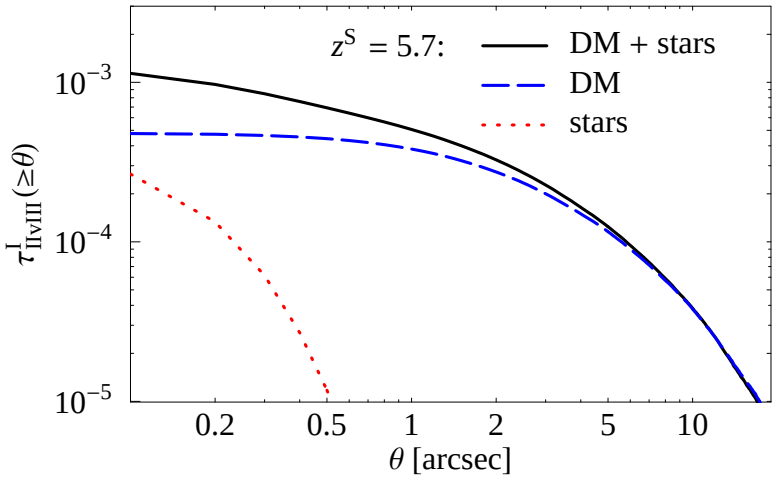

Figure 3.6: The optical depth $\tau^{\rm I}_{\rm II}\vee{\rm III}(\geq\theta)$ for rays of type II$\vee$III with lens impact parameters $\geq\theta$. Compared are the depths for lensing by both dark and luminous matter (solid line), by dark matter alone (dashed line), and by luminous matter alone (dotted line) for sources at redshifts $z^{\rm S}=5.7$.

The resulting optical depths $\tau^{\rm I}_{\rm II}\vee{\rm III}(\geq\theta)$ for rays of type II$\vee$III at angular separations $\geq\theta$ from the lens centre are plotted in Fig. 3.6 for sources at redshift $z^{\rm S}=5.7$. The difference between the optical depths for lensing by dark and luminous matter and lensing by dark matter alone are very large for images at radii <1 arcsec. However, the optical depths become more similar for larger radii so that the difference is less than 15 per cent for radii >5 arcsec, and becomes negligible for radii >10 arcsec. The other optical depths for strong lensing exhibit a very similar behaviour as a function of minimal distance from the lens. These findings agree well with results of Oguri (2006), who studied the image-separation distribution using analytical mass profiles, or Meneghetti et al. (2000), Meneghetti et al. (2003) and Dalal et al. (2004), who considered the influence of galaxies on the probabilities for giant arcs and arclets in clusters.

The cross-section $\partial\tau^{\rm I}_{{\rm II}\vee{\rm III},\geq\theta}/\partial\log M^{\rm L}$ for images of type II$\vee$III at radii $\geq\theta$ is plotted in Fig. 3.7 as a function of the lens halo mass $M^{\rm L}$. If all images are considered, the cross-sections for lensing by both dark and luminous matter differs quite strongly from the cross-section for lensing by dark matter alone. Restricted to images at radii $\theta>1$ arcsec, however, the cross-sections become quite similar. In particular, the cross-section for strong lensing at radii $\theta>1$ arcsec is very small for lenses with $M^{\rm L}<10^{13}h^{-1}\,{\rm M}_\odot$ even if the stellar mass is included. This confirms our assumption that the luminous and dark matter in smaller halos produces strongly lensed images only at radii <1 arcsec. For radii $\theta>5$ arcsec, there are virtually no lenses with masses below $M^{\rm L}<2\times10^{13}{\rm M}_\odot h^1$, and the cross-sections are almost identical.

The optical depths $\tau^{\rm S}(z^{\rm S})$ for strong lensing by both dark and luminous matter as a function of source redshift $z^{\rm S}$ are compared to the optical depths caused by dark matter alone in Fig. 3.8 for images with lens impact parameters ≥5 arcsec. These optical depths can be interpreted as being restricted to image splittings $\gtrsim10$ arcsec. The enhancement due to the stellar mass is larger for sources at lower redshift. For $z^{\rm S}=1$, the stellar

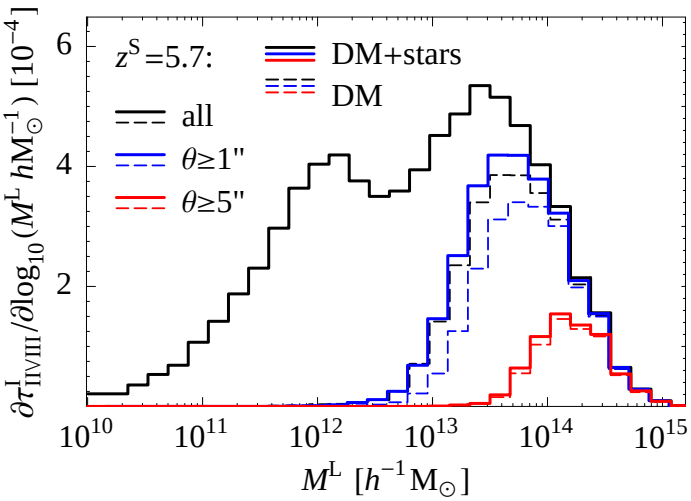

Figure 3.7: The cross-section $\partial\tau^{\rm I}_{\rm II\vee III,\geq\theta}/\partial\log M^{\rm L}$ as a function of the lens halo mass $M^{\rm L}$ (see text) for lensing by both dark and luminous matter (solid line) and lensing by dark matter (dashed line) for sources at redshift $z^{\rm S}=5.7$. Compared are the cross-sections for rays of type II $\vee$ III regardless of their impact parameters (black lines), at impact parameters $\theta\geq 1\,$arcsec (blue lines), and at $\theta\geq 5\,$arcsec (red lines).

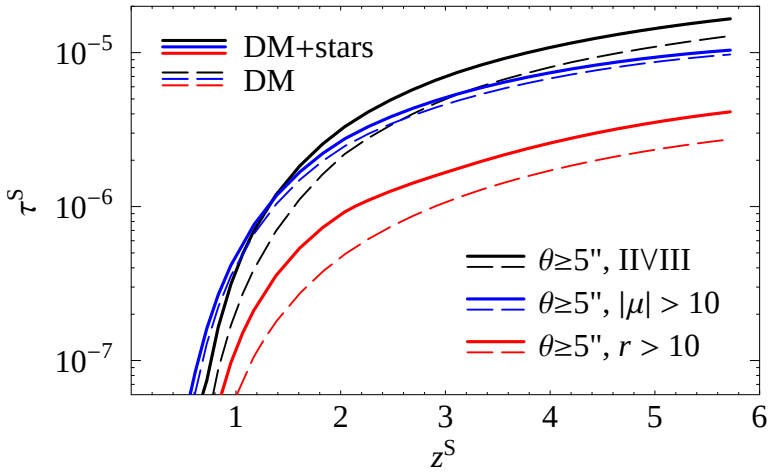

Figure 3.8: The optical depth $\tau^{\rm S}$ as a function of source redshift $z^{\rm S}$ for images of small circular sources of type II $\vee$ III (black lines), with large magnification (blue) and with large length-to-width ratio (red) at lens impact parameters $\theta\geq 5\,$arcsec. Compared are the optical depths for lensing by both dark and luminous matter (solid lines) and by dark matter alone (dashed lines).

mass increases the optical depths by up to a factor two. For larger source redshifts the increase is $\lesssim 1.5$ depending on source redshift and the property considered. Compared to the other optical depths, the optical depth for $|\mu|>10$ is affected least by the stellar matter. Note that the difference in the optical depths for lensing by both dark and luminous matter and by dark matter alone is larger for $\tau^{\rm S}$ than for $\tau^{\rm I}$ because of additional differences in the magnification distribution.

3.3.5 Quasar lensing

The optical depths for images lensed by luminous and dark matter at radii ≥ 5 arcsec (Fig. 3.8) are an order of magnitude lower than the corresponding depths for images at radii ≥ 0.5 arcsec (not shown). This ratio is consistent with results by Inada et al. (2008), who identified ten lensed quasars with image splittings 1–2 arcsec and one lensed quasar with a splitting of 15 arcsec in a statistical sample of 22 683 quasars with redshifts $0.6 \leq z \leq 2.2$ from the Sloan Digital Sky Survey (SDSS).

The quasar sample of Inada et al. (2008) has been used by Oguri et al. (2008) to constrain the matter content and dark-energy evolution of the Universe. Hennawi et al. (2007a) estimated the number of expected number of quasars with very large image separations in similar samples. To obtain an estimate of the expected total number of lensed quasars in the sample of Inada et al. (2008) from our data, we assume that every strongly lensed source with image splitting ≥ 1 arcsec has one image of type II at radii ≥ 0.5 arcsec from the lens centre. The quasar sample is limited to apparent i-band magnitudes $m_i < 19.1$. For the calculation of the magnification bias, we use the quasar luminosity function obtained by Richards et al. (2005) from the 2dF-SDSS LRG and Quasar Survey and Croom et al. (2004):

$$\Phi(L_g; z) = \frac{\Phi^*(z)}{L_g^*(z)} \left[\left(\frac{L_g}{L_g^*(z)} \right)^{-\alpha} + \left(\frac{L_g}{L_g^*(z)} \right)^{-\beta} \right]^{-1} . \tag{3.7}$$

Here, L_g denotes the rest-frame g-band luminosity, z the quasar redshift, and $\Phi^*(z)$ a normalisation constant. The bright-end slope $\alpha = -3.31$, and the faint-end slope $\beta = -1.45$. The break luminosity $L_g^*(z)$ is parametrised as

$$L_g^*(z) = 10^{k_1 z + k_2 z^2 - 0.4 M_g^*(0)} L_{g0} \tag{3.8}$$

with $M_g^*(0) = -21.61$, $k_1 = 1.39$, $k_2 = -0.29$, and L_{g0} as a luminosity standard.

We then convert the apparent i-band magnitude limit $m_i^{\rm lim} = 19.1$ to the corresponding g-band luminosity

$$L_g^{\rm lim}(z) = 10^{-0.4\left[m_i^{\rm lim} - {\rm DM}(z) - K_{i,g}(z)\right]} L_0, \tag{3.9}$$

where DM(z) denotes the distance modulus to redshift z, and the K-correction $K_{i,g}(z)$ 'corrects' between observer-frame i-band and rest-frame g-band. We use the K-correction discussed in Richards et al. (2006), i.e. we assume $K_{i,g} = K_{i,i'}(z) - 0.664$ with $K_{i,i'}(z)$ given by table 4 in Richards et al. (2006).

The quasar lensing cross-section $\sigma_{\rm QL}(z)$ as a function of redshift z is then calculated

from our ray sample by (Schneider et al. 1992):

$$\begin{aligned}\sigma_{\rm QL}(z) &= \frac{1}{N_{\rm rays}}\sum_{i=1}^{N_{\rm rays}}|\mu(i;z)|^{-1}1_{\rm QL}(i;z)\times \\ &\qquad\times\frac{\int_{|\mu(i;z)|^{-1}L_g^{\rm lim}(z)}^{\infty}\Phi(L_g;z){\rm d}L_g}{\int_{L_g^{\rm lim}(z)}^{\infty}\Phi(L_g;z){\rm d}L_g}, \\ &= \frac{1}{N_{\rm rays}}\sum_{i=1}^{N_{\rm rays}}|\mu(i;z)|^{-1}1_{\rm QL}(i;z)\times \\ &\qquad\times\frac{F(|\mu(i;z)|^{-1}x^{\rm lim}(z))}{F(x^{\rm lim}(z))}.\end{aligned} \tag{3.10}$$

Here, $N_{\rm rays}$ denotes the total number of rays, $\mu(i;z)$ denotes the magnification of ray i for sources at redshift z, and $1_{\rm QL}(i;z)=1$ if ray i is of type II with lens impact parameter ≥ 0.5 arcsec, and zero otherwise,

$$F(x^{\rm lim}) = \int_{x^{\rm lim}}^{\infty}\left[x^{-\alpha}+x^{-\beta}\right]^{-1}{\rm d}x\,, \tag{3.11}$$

and $x^{\rm lim}(z)=L_g^{\rm lim}(z)/L_g^*(z)$. The factor $|\mu(i;z)|^{-1}$ in Eq. (3.10) accounts for the fact that we assume a uniform distribution of sources in the source plane, while our ray sampling method uniformly samples the image plane. The ratio of the cumulative luminosity distributions quantifies the increase of source counts due to a lower luminosity threshold for detection in regions of higher magnification.

Under the assumption that the total number of quasars is not affected by magnification bias, the number of lensed quasars $N_{\rm QL}$ in the sample of Inada et al. (2008) is obtained by integrating over the observed redshift distribution $n_{\rm Q}(z)$ of the quasar sample[10] weighted by the cross-section:

$$N_{\rm QL} = \int_0^{\infty} n_{\rm Q}(z)\sigma_{\rm QL}(z){\rm d}z\,. \tag{3.12}$$

If we consider lensing by dark matter alone, we predict less than one lensed quasar with image splitting ≥ 1 arcsec. For lensing by both luminous and dark matter, three lensed quasars with image splitting ≥ 1 arcsec are predicted. This is still small compared to the 11 lensed quasars in the sample. One reason for this discrepancy could be that our simple ray-selection criterion $1_{\rm QL}$ does not provide a very good approximation for the fraction of strongly lensed sources with image splittings > 1 arcsec.[11] Furthermore, we certainly underestimated the magnification bias.[12] Other possible reasons for the discrepancy

[10] http://www-utap.phys.s.u-tokyo.ac.jp/~sdss/sqls/

[11] The criterion $1_{\rm QL}$ effectively excludes (the abundant) lenses with $r_{\rm E} < 0.5$ arcsec, which do not produce image splittings $\gtrsim 0.5$ arcsec. Undesirably, the criterion also excludes those multi-image systems with image separations > 0.5 arcsec where the type-II image is near the centre of the lens.

[12] The magnitude limit for the quasar sample is $i_{\rm cor} \leq 19.1$, where $i_{\rm cor}$ is the Galactic-extinction corrected magnitude of the brightest image with an image-separation dependent admixture of the fainter image(s) and the lens galaxy (Oguri et al. 2006). Moreover, the brightest image is often the primary image, which is of type I, but *not* of type II.

may be effects of non-spherical baryon distribution or halo contraction due to baryon condensation. These are not considered here. Imitating the contraction effect by simply doubling the stellar mass in the galaxies, we predict about 8 lensed quasars, much closer to the observed numbers of lensed quasars. These results indicate that predictions are very sensitive to detailed assumptions about galaxy and dark matter structure on small scales, and are thus unlikely to provide robust constraints on cosmological parameters.

3.4 Summary

In this work, we have studied how the stellar components of galaxies affect predictions for gravitational lensing in the concordance ΛCDM cosmology. Our results were obtained by shooting random rays though a series of lens planes created from the Millennium Simulation. The dark-matter component on the lens planes was constructed directly from the dark-matter particle distribution of the simulation, while the distribution of the luminous matter was obtained from semi-analytic galaxy formation models run on stored merger trees from the simulation.

In Sec. 3.3.1 we discussed the influence of stellar mass on the statistical distribution of point-source magnifications. Although this distribution is almost unchanged for magnifications $\mu \approx 1$, the galaxies induce a noticeable increase of the probability for very high and very low magnifications.

In Sec. 3.3.2, we presented optical depths for images of small sources that are highly magnified, strongly distorted or belong to multiply imaged sources. We compared the results obtained by including both dark and luminous matter to those obtained for dark matter alone. We find that the inclusion of the luminous matter greatly enhances the strong-lensing optical depths compared to a 'dark-matter only' universe. Our results in Sec. 3.3.3 show that the increase is partly due to a significant enhancement of the strong-lensing cross-section of group and cluster halos with virial masses $M > 10^{13} h^{-1}\,\mathrm{M}_\odot$. In addition, the stellar matter leads to significant strong lensing in smaller halos, which would not cause noticeable strong lensing otherwise. Although these halos have typical Einstein radii $r_\mathrm{E} \lesssim 1\,\mathrm{arcsec}$, their large abundance outweighs their small individual cross-sections, leading to a bimodal distribution of integrated cross-sections with halo mass both for strongly distorted images and for multiply imaged sources at redshifts $z^\mathrm{S} \lesssim 1$.

In Sec. 3.3.4, we estimated optical depths for strongly lensed images formed at larger distance from centre of their lens. Although the optical depths for lensing by both the dark and luminous matter are much larger than for lensing by dark matter alone for images at radii $< 1\,\mathrm{arcsec}$, for images at larger radii the optical depths are much more similar. For images at radii $\geq 5\,\mathrm{arcsec}$, the optical depths differ by at most a factor of two. For radii $\gtrsim 10\,\mathrm{arcsec}$, there is almost no enhancement due to the galaxies, in agreement with earlier studies (e.g. Meneghetti et al. 2003; Dalal et al. 2004).

Our results are consistent with the observed radial distribution of multiply imaged quasars with splittings $\geq 1\,\mathrm{arcsec}$ in the recent SDSS quasar sample of Inada et al. (2008) *only* if the effect of the galaxies is taken into account. The total number of lensed quasars predicted by our standard model is still quite low compared to the number

observed, indicating a need to include the effects of baryonic dissipation on the dark matter distribution in order to explain the data fully.

An obvious extension of the work presented here will be ray-tracing over finite fields to study the effects of lensing on sources with finite extent. With a realistic distribution of source properties, the results could be compared directly with observations of massive galaxy clusters, where many distorted images and multi-image systems have been studied in some detail (Broadhurst et al. 2005; Halkola et al. 2006).

Here, we used only the stellar mass and the size information from the semi-analytic galaxy formation models. In future work, the morphology and luminosity information could be added to simulate galaxy-galaxy lensing surveys with given selection functions. With some improvements in the modelling of the galaxies, in particular by assuming realistic elliptical profiles for the stellar components, such simulated surveys will provide detailed predictions for galaxy-galaxy lensing.

The dark-matter distribution in galaxies, groups and clusters does not merely provide an arena for physical processes in the baryonic gas, it is also subject to modification by these processes (Blumenthal et al. 1986; Gnedin et al. 2004). Baryon condensation increases the dark-matter density in the inner parts of halos, and so affects their dark-matter lensing properties (Puchwein et al. 2005; Jing et al. 2006; Rozo et al. 2006). The semi-analytic models used here do not yet describe these processes, but they should be included in future work aiming at higher precision.

Acknowledgments

We thank Volker Springel, Gabriella De Lucia, Jérémy Blaizot, Manfred Kitzbichler, and Ole Möller for helpful discussions. This work was supported by the DFG within the Priority Programme 1177 under the projects SCHN 342/6 and WH 6/3.

4 Imaging the cosmic matter distribution using gravitational lensing of pregalactic HI

Stefan Hilbert, R. Benton Metcalf, and S. D. M. White, 2007: MNRAS, 382, 1494

Abstract

21-cm emission from neutral hydrogen during and before the epoch of cosmic reionisation is gravitationally lensed by material at all lower redshifts. Low-frequency radio observations of this emission can be used to reconstruct the projected mass distribution of foreground material, both light and dark. We compare the potential imaging capabilities of such 21-cm lensing with those of future galaxy lensing surveys. We use the Millennium Simulation to simulate large-area maps of the lensing convergence with the noise, resolution and redshift-weighting achievable with a variety of idealised observation programmes. We find that the signal-to-noise of 21-cm lens maps can far exceed that of any map made using galaxy lensing. If the irreducible noise limit can be reached with a sufficiently large radio telescope, the projected convergence map provides a high-fidelity image of the true matter distribution, allowing the dark matter halos of individual galaxies to be viewed directly, and giving a wealth of statistical and morphological information about the relative distributions of mass and light. For instrumental designs like that planned for the Square Kilometer Array (SKA), high-fidelity mass imaging may be possible near the resolution limit of the core array of the telescope.

Key words: large-scale structure of Universe – dark matter – gravitational lensing – intergalactic medium

4.1 Introduction

Since Zwicky (1933) first realised that unseen material is needed to explain the dynamics of galaxy clusters, many observations have indicated that large-scale structures are dominated by some form of dark matter. The now widely accepted cold dark matter (CDM) model provides a consistent explanation for cosmic microwave background (CMB) fluctuations, for type Ia supernova distances, for clustering measures from galaxy redshift surveys, for galaxy cluster abundances and their evolution, and for the statistics both of weak gravitational lensing and of Lyα absorption in quasar spectra. The universe apparently contains about five times as much dark matter as ordinary baryons, providing in total about a quarter of the closure density. According to the CDM picture, every

galaxy has its own dark matter halo, which may be partially disrupted in a group or cluster to produce a common halo. These structures can be predicted in great detail by numerical simulations, but the predictions are yet to be convincingly verified because we are unable to map the dark matter distribution in enough detail to make a proper comparison. Weak gravitational lensing of distant galaxies has allowed progress to be made, but only near the centres of the largest galaxy clusters is the signal-to-noise sufficient for true mapping. The limitations of this approach are clearly indicated by the recent image of a representative field made using deep Hubble Space Telescope data by Massey et al. (2007a). The resolution and sensitivity of lensing maps based on galaxies are fundamentally limited by the finite number density and the intrinsic ellipticities of the sources. In this paper, we demonstrate that much higher fidelity and resolution can be achieved if future observations allow pregalactic HI to be used as the gravitationally lensed source.

The spin temperature of neutral hydrogen during and before the epoch of reionisation ($8 \lesssim z \lesssim 300$) fell out of thermal equilibrium with the CMB radiation, resulting in the absorption and emission of 21-cm radiation. There has been a great deal of interest in the prospect of detecting and mapping this radiation using radio telescopes now under construction or in planning (see Furlanetto et al. 2006, for an extensive review). This radiation provides an excellent source for gravitational lensing studies. Structure is expected in the 21-cm emission down to arcsecond scales, and at each point on the sky there will be ~ 1000 statistically independent regions at different redshifts, and thus frequencies, that could in principle be observed. Gravitational lensing will coherently distort the 21-cm brightness temperature maps at these different frequencies. For each frequency, the gradient in the brightness temperature may be used to obtain an estimate of the lensing distortion. Since the intrinsic structure in the HI gas that acts as noise on the estimate is uncorrelated for maps at (sufficiently) different frequencies, the coherent distortion of the brightness temperature can be measured with high accuracy if enough independent redshifts are observed. In this way, a map of the foreground matter density can be constructed (Zahn and Zaldarriaga 2006; Metcalf and White 2007).

Observing the 21-cm radiation at high redshift is challenging. Foregrounds of atmospheric, galactic, or extragalactic origin (e.g. synchrotron radiation from electrons) dominate over the 21-cm signal in the relevant frequency range (Furlanetto et al. 2006). The foregrounds are expected to vary much less with frequency (and with position on the sky for galactic foregrounds) than the 21-cm signal from high-redshift HI structures (Zaldarriaga et al. 2004; Zahn and Zaldarriaga 2006). Therefore, it is hoped that the foreground radiation and the 21-cm signal may be separated by modelling the foregrounds as slowly varying functions of frequency.

Subtracting foregrounds from the observed radiation will be complicated and will contribute noise to the temperature map. In addition to the noise from foreground residuals, there is *irreducible noise* in the mass map constructed from the 21-cm-lensing signal, which comes from the unknown intrinsic structure of the 21-cm brightness temperature distribution. This noise cannot be reduced by increasing the collecting area of the telescope, by increasing the integration time or by improving the removal of foregrounds. Metcalf and White (2007) showed that if the signal-to-noise in the brightness temperature map at each frequency is greater than one, then the noise in the mass map

will be close to the irreducible value. Increasing the frequency resolution of the radio observations increases the number of effectively independent regions along the line-of-sight until the bandwidth becomes smaller than the radial correlation length of structure in the brightness temperature distribution. If the bandwidth is matched to the correlation length, the irreducible noise is minimised. The correlation length in turn depends on beam size, and is smaller for smaller beams. Thus unlike galaxy lensing surveys, the irreducible noise *decreases* with increasing resolution for 21-cm lensing. In practise, there is a trade-off because smaller bandwidth means less flux, but this can be compensated by increasing collecting area and/or integration time. In this paper, we study what is achievable with an idealised radio telescope, so we assume that the irreducible noise level is reached, using values calculated by Metcalf and White (2007) as a function of beam-size and frequency.

At least in principle, a 21-cm lensing survey will be much less noisy than surveys using galaxies (because of the larger effective number of sources) and will have a substantially stronger signal (because of the greater distance of the sources and the additional structure that lies in front of them). For a galaxy shear map, the noise increases with decreasing smoothing because fewer galaxies are used to estimate the shear at each point of the map. The opposite is true for 21-cm lensing, where a smaller beam allows one to observe more independent sources along each line-of-sight. It should therefore be possible to make high-resolution images of the matter distribution at high signal-to-noise using 21-cm lensing, while the smallest scale over which galaxy lensing can map with $S/N > 1$ is $\gtrsim 1\,\mathrm{arcmin}$, even using an ambitious dedicated space telescope. In addition, 21-cm lensing will provide information about the mass distribution at redshifts much higher than can be probed by galaxy lensing. The results we show below illustrate these points clearly.

This paper is organised as follows. In Sec. 4.2, the relevant elements of lensing theory are introduced, and the parameters of our idealised surveys are discussed. Our lensing simulation method is described in Sec. 4.3. The results of our simulations are presented in Sec. 4.4. Sec. 4.5 contains our conclusions.

4.2 Lensing preliminaries

Gravitational lensing shifts the observed position of each point in the image of a distant source. Take the observed angular position on the sky to be $\boldsymbol{\theta}$ and the position in the absence of lensing to be $\boldsymbol{\beta}$. The first-order distortion in the image is expressed by the derivatives of the mapping between these angles. The distortion matrix is commonly decomposed into the convergence κ and two components of shear, γ, defined by

$$\left[\frac{\partial \boldsymbol{\beta}}{\partial \boldsymbol{\theta}}\right] = \begin{pmatrix} 1-\kappa+\gamma_1 & \gamma_2 \\ \gamma_2 & 1-\kappa-\gamma_1 \end{pmatrix}. \tag{4.1}$$

To lowest order and to an excellent approximation (Vale and White 2003), the con-

vergence is related directly to the distribution of matter through

$$\kappa\left(\boldsymbol{\theta}\right) = \frac{3}{4} H_o \Omega_m \int_0^\infty dz \; \frac{(1+z)^2}{E(z)} g\left(z\right) \delta\left(D(z)\,\boldsymbol{\theta}, z\right) \tag{4.2a}$$

$$\simeq \frac{4\pi G}{c^2} \sum_i g\left(z_i\right) \left(\Sigma_i\left(\boldsymbol{\theta}\right) - \overline{\rho}\left(z_i\right) \delta l_i\right) = \sum_i \kappa_i \tag{4.2b}$$

with

$$g(z) = (1+z)^{-1} \int_z^\infty dz' \; w\left(z'\right) \frac{D(z,0) D(z',z)}{D(z',0)}. \tag{4.2c}$$

Here $D(z',z)$ is the angular size distance between the two redshifts, and $\delta(\boldsymbol{x},z)$ is the fractional density fluctuation at redshift z and perpendicular position $\boldsymbol{x}$. The function $E(z) = \sqrt{\Omega_m(1+z)^3 + \Omega_\Lambda + (1-\Omega_m-\Omega_\Lambda)(1+z)^2}$, where Ω_m and Ω_Λ, are the densities of matter and the cosmological constant measured in units of the critical density. The weighting function for the source distance distribution, $w(z)$, is normalised to unity.

Equation (4.2b) is the multiple-lens-plane approximation, in which z_i is the redshift of the ith lens plane, $\Sigma_i\left(\boldsymbol{\theta}\right)$ is its surface density, δl_i is its proper thickness, and $\overline{\rho}(z_i)$ is the average matter density of the universe. This approximation is well justified if the planes are thin compared to the range in redshift over which $g(z)$ varies and $\kappa_i \gtrsim 1$ for no more than one lens plane. This second requirement is well justified for all but a very small fraction of the sky where multiple galaxy clusters happen to overlap in projection.

When we consider galaxy surveys, we model the redshift distribution of usable galaxies as

$$w(z) = \frac{3z^2}{2z_0^3} \exp\left[-\left(\frac{z}{z_0}\right)^{3/2}\right] \text{, where } \; z_0 = \frac{z_{\rm med}}{1.412} \tag{4.3}$$

is set to obtain the median redshift $z_{\rm med}$ appropriate for each specific survey (Smail et al. 1994). We estimate the smoothed convergence distribution for a Gaussian smoothing kernel defined by

$$W(\theta) = \frac{2}{\pi\lambda^2} \exp\left(-\frac{2\theta^2}{\lambda^2}\right), \tag{4.4}$$

where θ denotes the angular separation between two points on the sky, and the 'beam diameter' λ quantifies the spatial scale of the smoothing. For the kernel (4.4), the correlation function for the noise in the convergence map is given by

$$\xi_{\rm N}(\theta) = \frac{\sigma_\epsilon^2}{2\pi\lambda^2 n_{\rm g}} \exp\left(-\frac{\theta^2}{\lambda^2}\right) \; , \tag{4.5}$$

where $n_{\rm g}$ is the number density of source galaxies on the sky, and σ_ϵ is the standard deviation in the magnitude of their ellipticities (van Waerbeke 2000). A realistic value is $\sigma_\epsilon = 0.3$ [for example, $\sigma_\epsilon = 0.32 + 0.0014(\text{mag} - 20)^3$ for the ACS camera on HST (Massey et al. 2007b)]. The proposed satellite SNAP[1] is expected to survey $\sim 2\%$ of the sky with an estimated galaxy density of $n_{\rm g} \simeq 100\,\text{arcmin}^{-2}$ and a median redshift $z_{\rm med} \sim 1.23$. [For comparison, Massey et al. (2007a,b) were able to use 71 galaxies

[1] snap.lbl.gov

per square arcminute in the HST COSMOS survey.] The DUNE[2] satellite proposes surveying $\sim 50\%$ of the sky with $n_{\rm g} \simeq 35\,{\rm arcmin}^{-2}$ and a median redshift $z_{\rm med} \sim 0.9$. Several proposed ground based surveys – LSST[3], PanSTARRS[4], VISTA[5] – hope to reach source number densities comparable to DUNE. In the following, we adopt these two sets of parameters as our optimistic assessment of the parameters defining future *space-* and *ground-based* galaxy surveys. For a Gaussian smoothing with $\lambda = 1\,{\rm arcmin}$, they yield a normalization, $\sigma_{\rm N} = \sqrt{\xi_{\rm N}(\theta = 0)}$, of 0.012 and 0.02, respectively, for the noise correlation.

When simulating convergence maps derived from 21-cm observations, we will make the approximation $w(z) = \delta(z - z_0)$. This is reasonable because angular size distances are a weak function of source redshift over the relevant range. The noise in the convergence map is worked out in Metcalf and White (2007) under the assumption that the high-frequency components of maps of pregalactic HI decorrelate with increasing redshift separation in the same way as those of maps of the underlying cold dark matter distribution. In this case, the noise is very well approximated as a Poisson process smoothed by the telescope beam, which we again model as Gaussian. This results in the same correlations as in Eq. (4.5) except with a different normalisation $\sigma_{\rm N}$. Here, we adopt normalisations of 0.0042 for a $\lambda = 6$ arcsecond beam and 0.014 for a $\lambda = 1$ arcminute beam. These values are representative for surveys that observe the 21-cm radiation at redshifts around $z_0 = 12$, work close to the irreducible-noise limit, cover $\sim 10\,{\rm MHz}$ in frequency, and have optimal bandwidth $\sim 0.05\,{\rm MHz}$. A beam size $\lambda = 6\,{\rm arcsec}$ is very futuristic, since it corresponds to a densely filled array with baselines of order 100 km. A beam with $\lambda = 1\,{\rm arcmin}$ might be realized with the planned Square Kilometer Array[6] (SKA) (Metcalf and White 2007). The assumed source redshift $z_0 = 12$ for the 21-cm radiation lies within the expected obvservable redshift range of the SKA.

4.3 Simulations

We simulated maps of the lensing convergence using the Millennium Simulation (Springel et al. 2005) and the multiple-lens-plane approximation. The Millennium Simulation is a very large N-body simulation of cosmological structure formation containing 10^{10} particles in a cubic region of $L = 500h^{-1}\,{\rm Mpc}$ comoving on a side. The cosmological parameters for the simulation are: $\Omega_m = 0.25$, $\Omega_\Lambda = 0.75$, and a Hubble constant of $h = 73$ in units of $100\,{\rm km\,s^{-1}Mpc^{-1}}$. The initial density power spectrum is scale-invariant (spectral index $n = 1$) with normalisation $\sigma_8 = 0.9$. Snapshots of the matter distribution were stored on disk at 64 output times between redshift $z = 127$ and $z = 0$. For $0 \leq z \leq 1$, the snapshots are spaced at roughly 200 Myr intervals resulting in 23 snapshots in that range. Above redshift unity, the snapshots are spaced approximately logarithmically in the expansion factor.

[2] www.dune-mission.net
[3] www.lsst.org
[4] pan-stars.ifa.hawaii.edu
[5] www.vista.ac.uk
[6] www.skatelescope.org

For each snapshot of the simulation, we project the matter distribution in a slice of appropriate thickness onto a plane and place it at the snapshot's redshift along the line of sight. The projected matter density on these lens planes is represented by meshes with a spacing of $2.5h^{-1}\,\mathrm{kpc}$ comoving. In order to reduce discreteness noise while retaining the high resolution of the simulation, an adaptive smoothing kernel is used. Before projection, the mass associated with each particle is distributed in a spherical cloud with Gaussian density profile and *rms* radius equal to half the distance to its 64th nearest neighbour. The projected density at each mesh point on the lens plane is then calculated by summing the contributions from each particle.

To create convergence maps over a field of $10^\circ \times 10^\circ$, we shoot 36000×36000 light rays through the series of 50 lens planes which extend from $z = 0$ to $z = 9$. On each lens plane, we calculate the projected matter density at the position of each ray by bilinear interpolation between surrounding mesh points. Using Eq. (4.2), the convergence κ_i is then calculated and summed for each ray to get $\kappa(\boldsymbol{\theta})$ for the assumed source redshift distribution [i.e. $w(z) = \delta(z - 12)$ for the 21-cm emission, and $w(z)$ given by Eq. (4.3) for the galaxies].

The convergence maps obtained by this procedure have a resolution of 1 arcsecond and are essentially noise-free. In order to simulate maps as they would be observed, we add independent Gaussian noise with appropriate dispersion to each pixel and smooth the maps using a Gaussian filter representing either the radio telescope beam or the required smoothing in the case of galaxy lensing. This procedure yields convergence maps with the desired resolution and with noise satisfying Eq. (4.5).

For a $10^\circ \times 10^\circ$ field, the comoving volume of the backward light cone out to $z = 12$ is more than 32 times that of the Millennium Simulation. The region out to $z = 2$ which contains most of the lensing structures is still 4.5 times larger in comoving volume than the simulation. Every simulated object thus contributes to the projected mass distribution several times. As explained in Hilbert et al. (2007b), the lens planes were constructed by projection along a line-of-sight which is tilted with respect to the principal axes of the simulation, and as a result are periodic on a rectangular cell of size $1.58 \times 1.66h^{-2}\mathrm{Gpc}^2$ comoving; the periodic length normal to the lens planes is $5.24h^{-1}\mathrm{Gpc}$ comoving. There are objects that appear multiple times at the same redshift when $z > 1.2$, but the number of these cases becomes significant (i.e. exceeds 1/3 of all objects at a given redshift) in our field only for $z > 2$. Objects also appear multiple times at different redshifts. However, objects are projected on top of their own images only in very few (special) directions and for very widely separated redshifts.[7] Generally multiple copies of objects are almost always seen at different redshifts and are almost always projected onto different foregrounds and backgrounds. As a result, there is effectively no duplication of projected structure within this field, despite the fact that the total

[7] Our lens-plane geometry ensures that multiple copies at the same or similar redshift are separated by angles equal to or not much smaller than the angular scale of the simulation box at that redshift. These multiple copies introduce artificial correlations on large angular scales and decrease the statistical independence of well-separated parts of the simulated field, but they do not affect correlations on smaller angular scales, nor do they alter one-point statistics such as the convergence probability distribution. Since the artificial correlations have different angular scales at different redshifts, multiple copies have different foregrounds and backgrounds in projection.

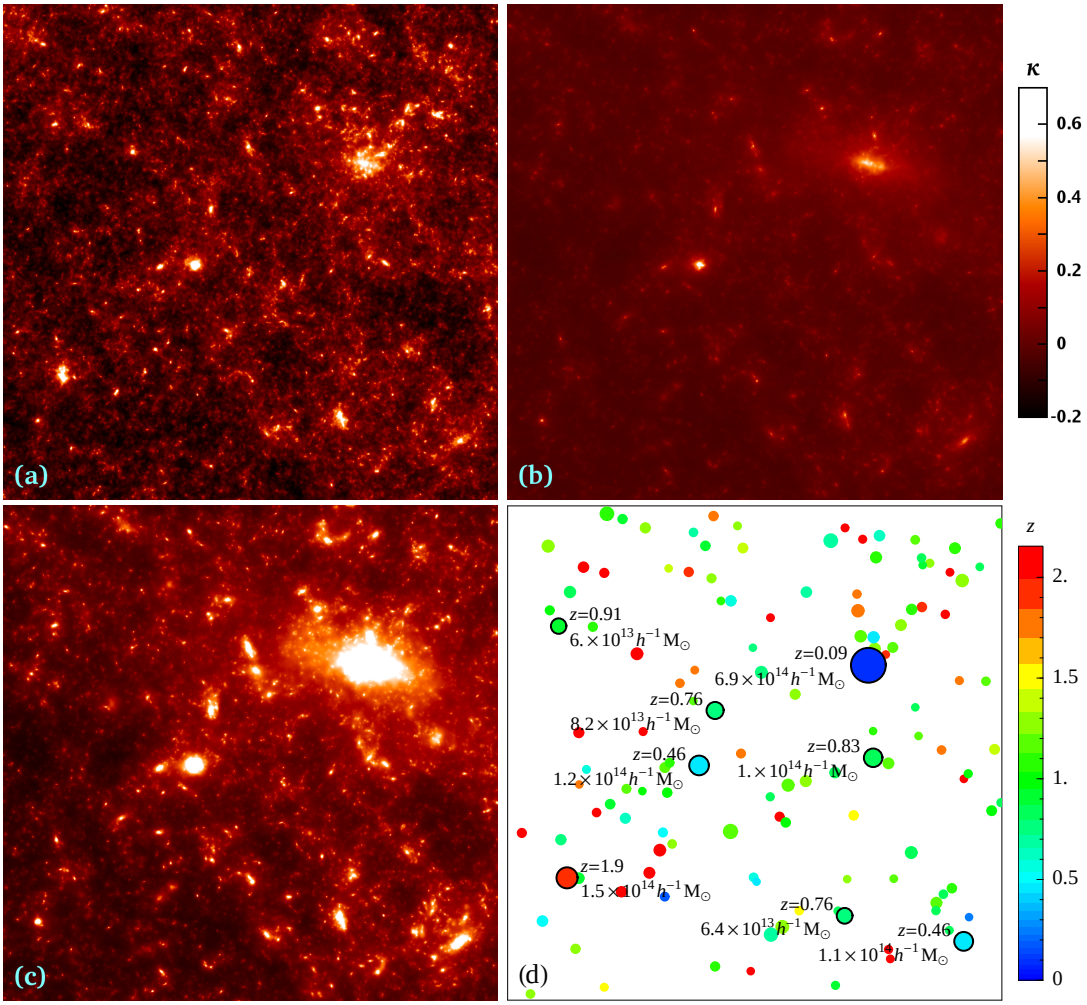

Figure 4.1: Convergence maps in a field of $20' \times 20'$. (a), (b) and (c) are all unsmoothed maps at 1 arcsec resolution. (a) has the distance weighting appropriate for HI sources at $z = 12$, while (b) and (c) are weighted as appropriate for a space-based galaxy survey with median redshift $z_{\rm med} = 1.23$. Both (a) and (b) follow the colour scale indicated by the bar. (c) is identical to (b) but with contrast enhanced by a factor of 11/3 to allow closer comparison with (a). Panel (d) identifies redshifts (colour-coded) and virial masses (size-coded) for all objects in the field with $M_{200} > 10^{13} h^{-1}\,{\rm M}_\odot$. The eight most massive objects are labelled explicitly.

comoving length of the line-of-sight out to $z = 12$ is more than 14 times the side of the computational box.

4.4 Results

4.4.1 Images

Figures 4.1, 4.2, and 4.3 show simulated convergence maps. The $20' \times 20'$ field shown in these examples is only a small fraction (1/900) of the full $10^\circ \times 10^\circ$ map that we

simulated. The latter is too large to be displayed in sufficient detail. This particular field was chosen because it has a prominent mass concentration at upper right that is large enough to be detected in all the cases we investigate. This halo is at redshift $z = 0.09$ and has a virial mass $M_{200} = 6.9 \times 10^{14} h^{-1}\,\mathrm{M}_\odot$. Thus it represents a galaxy cluster similar to the Coma cluster. For this reason, the field is not typical. From our Millennium Simulation data, we find that there is only a 3% probability for a random field this size to contain a halo more massive than $5 \times 10^{14} h^{-1}\,\mathrm{M}_\odot$.

The second largest mass concentration visible in the field (at lower left) is at redshift $z = 1.9$ and has a mass of $1.5 \times 10^{14} h^{-1}\,\mathrm{M}_\odot$. This is also a relatively unusual event. From our data, we expect one halo with $M_{200} > 10^{14} h^{-1}\,\mathrm{M}_\odot$ and $z > 1.5$ per square degree, corresponding to a 12% probability for a $20' \times 20'$ field. There are three more halos with masses above $10^{14} h^{-1}\,\mathrm{M}_\odot$ visible. The most prominent of these (left centre) is at redshift $z = 0.46$ and has a mass of $1.2 \times 10^{14} h^{-1}\,\mathrm{M}_\odot$. On average, we expect about two such clusters in each $20' \times 20'$ field.

The three convergence maps in Fig. 4.1 are made without smoothing or added noise in order to illustrate the dependence on the redshift distribution of the sources. The map at top left gives the expected convergence distribution (at 1 arcsec resolution) for sources at $z \sim 12$, representing the case of high-redshift 21-cm lensing. The map at top right uses the same colour table but a different source redshift distribution, that appropriate for an optimistic space-based galaxy survey. The principal impression in comparing the two is that there is much less structure in the 'galaxy' map. This reflects the lowering of the overall amplitude caused by the smaller source distances in the galaxy case. Averaged over the full $10^\circ \times 10^\circ$ area, the *rms* value σ_κ of κ is 0.11 in the 21-cm map, but only 0.03 in the galaxy map (see Tab. 4.1 for a summary of the statistical properties of our simulated maps). The map at lower left repeats the galaxy map, but now the contrast is enhanced by a factor of 11/3 so that the colour range matches that of the 21-cm map. Displayed in this way, the two maps look similar. Nearby objects such as the most massive cluster appear stronger in the galaxy map, whereas more distant objects appear stronger in the 21-cm map. There are a few large structures that appear in the 21-cm map, but are absent from the galaxy map. These are objects that lie beyond the redshifts assumed for the galaxies. In particular, the large mass concentration at $z = 1.9$ is clearly visible in the 21-cm map, but is virtually absent in the galaxy map. For the reader's orientation, the lower right map indicates masses and redshifts for all halos in the field with $M_{200} > 10^{13} h^{-1}\,\mathrm{M}_\odot$.

The two maps in Fig. 4.2 illustrate expectations for 21-cm lensing reconstructions based on a (futuristic) radio telescope with a Gaussian beam of width $\lambda = 6$ arcsec (corresponding to baselines ~ 100 km). The left image includes beam-smearing but excludes noise. A comparison with the 1 arcsec map at the top left of Fig. 4.1 shows that very little detail is lost, and over the full $10^\circ \times 10^\circ$ area the *rms* value of κ is reduced by only 9% to 0.098. The right image also includes noise assuming the irreducible level expected for observations with the optimal band width for a telescope beam of this size (~ 0.05 MHz). This has virtually no effect on the image, demonstrating that such a (very large) telescope could produce high resolution mass maps with very high fidelity. All structures with $M_{200} \geq 10^{13} h^{-1}\,\mathrm{M}_\odot$ (these are indicated in Fig. 4.1d) can be clearly identified out to high redshift, and even many smaller halos down to masses

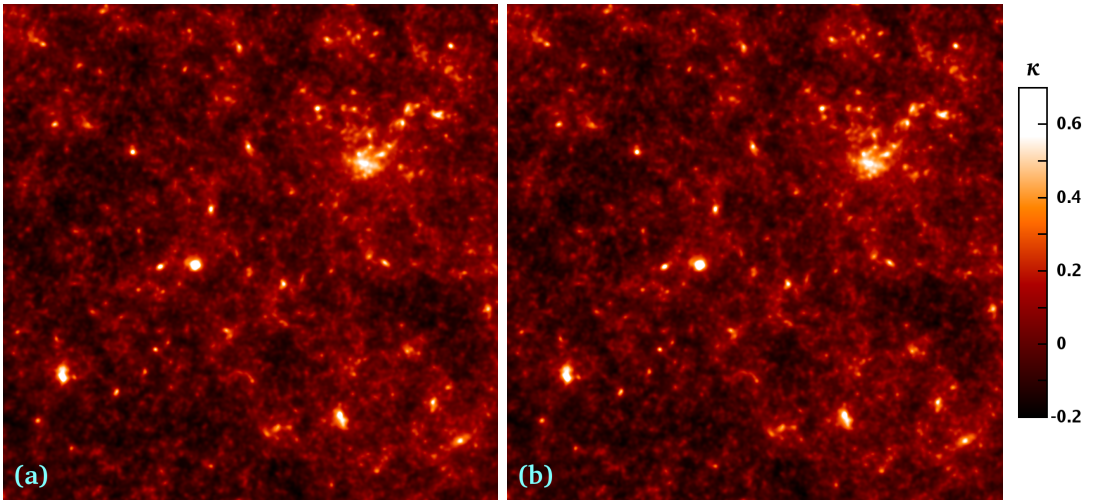

Figure 4.2: 21-cm-based convergence maps for the $20' \times 20'$ field shown in Fig. 4.1(a), but smoothed assuming a telescope beam with $\lambda = 6\,\mathrm{arcsec}$. Whereas (a) is noise-free, noise has been added in (b) at the irreducible value for a map of this resolution. The colour scale indicated by the bar at right is the same as in Fig. 4.1(a).

$M_{200} \gtrsim 10^{11} h^{-1}\,\mathrm{M}_\odot$ are visible. The signal-to-noise at the scale of the beam is very high even in low density regions, so substantial departures from optimal conditions could be tolerated without significant degradation of the resulting maps.

Figure 4.3 shows maps smoothed with a Gaussian of width $\lambda = 1\,\mathrm{arcmin}$. The colour scale is the same in all of them and differs from those of Fig. 4.1 and Fig. 4.2. Now, the resolution is similar to that obtainable with the planned Square Kilometer Array (Metcalf and White 2007). The top two images are for sources at $z \sim 12$ with no noise (left) and with noise at the irreducible level expected for observations at the optimal bandwidth for this beam-size (right). Again the fidelity of the image is high (although some differences can be seen in low-κ areas), and many of the more massive halos indicated in Fig. 4.1d are detected individually. The middle row of maps are for our optimistic space-based galaxy lensing case, again without and with noise, while the bottom row gives the corresponding maps for our optimistic ground-based survey parameters. As at higher resolution, one is struck by how little structure is visible in these maps compared to the 21-cm case. The rms value of κ over the full $10^\circ \times 10^\circ$ field is smaller by factors of 3 and 4 in the space- and ground-based galaxy cases in comparison with the 21-cm case (see Table 4.1).

The fidelity of the 'observed' (i.e. noisy) maps is low in the galaxy lensing cases. A few of the structures seen in the noiseless maps are still visible in their noisy counterparts, in particular the largest object, but many of the low-amplitude peaks in these maps are due to noise. In effect, only the large cluster at $z = 0.09$ is unambiguously detected for both surveys, while the two $10^{14} h^{-1}\,\mathrm{M}_\odot$ halos at $z = 0.46$ also stand out above the noise in the 'space-based' map. The larger halo at $z = 1.9$ remains unseen. The fidelity of these maps could be improved by increasing the smoothing length, but this would be at the expense of losing all the individual halos. In practice, an adaptive smoothing method such as a maximum entropy scheme would probably be used in order to remove

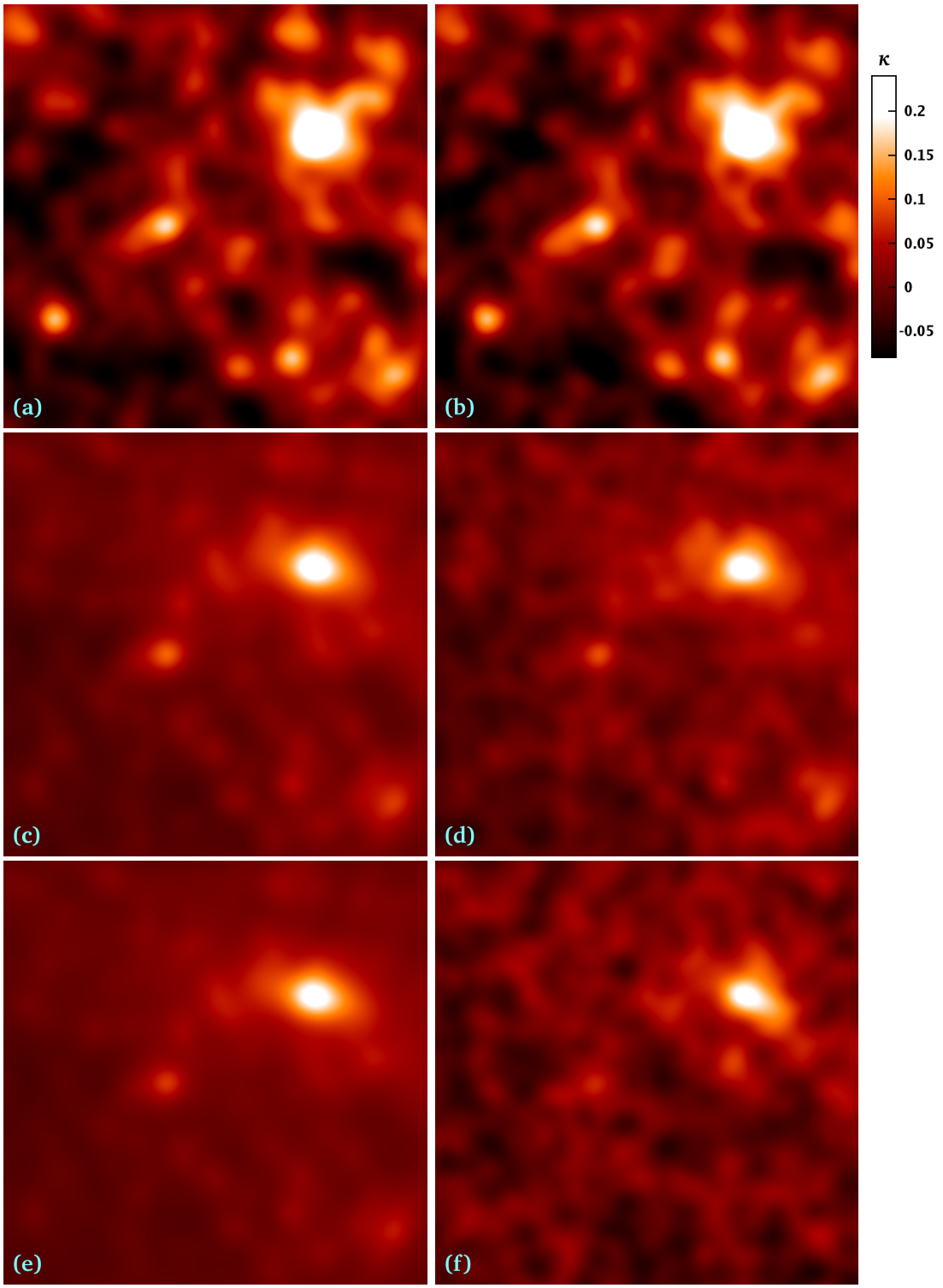

Figure 4.3: Convergence maps smoothed at $\lambda = 1$ arcmin for the $20' \times 20'$ field shown in Fig. 4.1: (a) and (b) 21-cm-based map *without* and *with* noise, resp.; (c) and (d) space-based galaxy lensing map without and with noise; (e) and (f) ground-based galaxy lensing map without and with noise. All panels use the colour scale indicated by the bar at right.

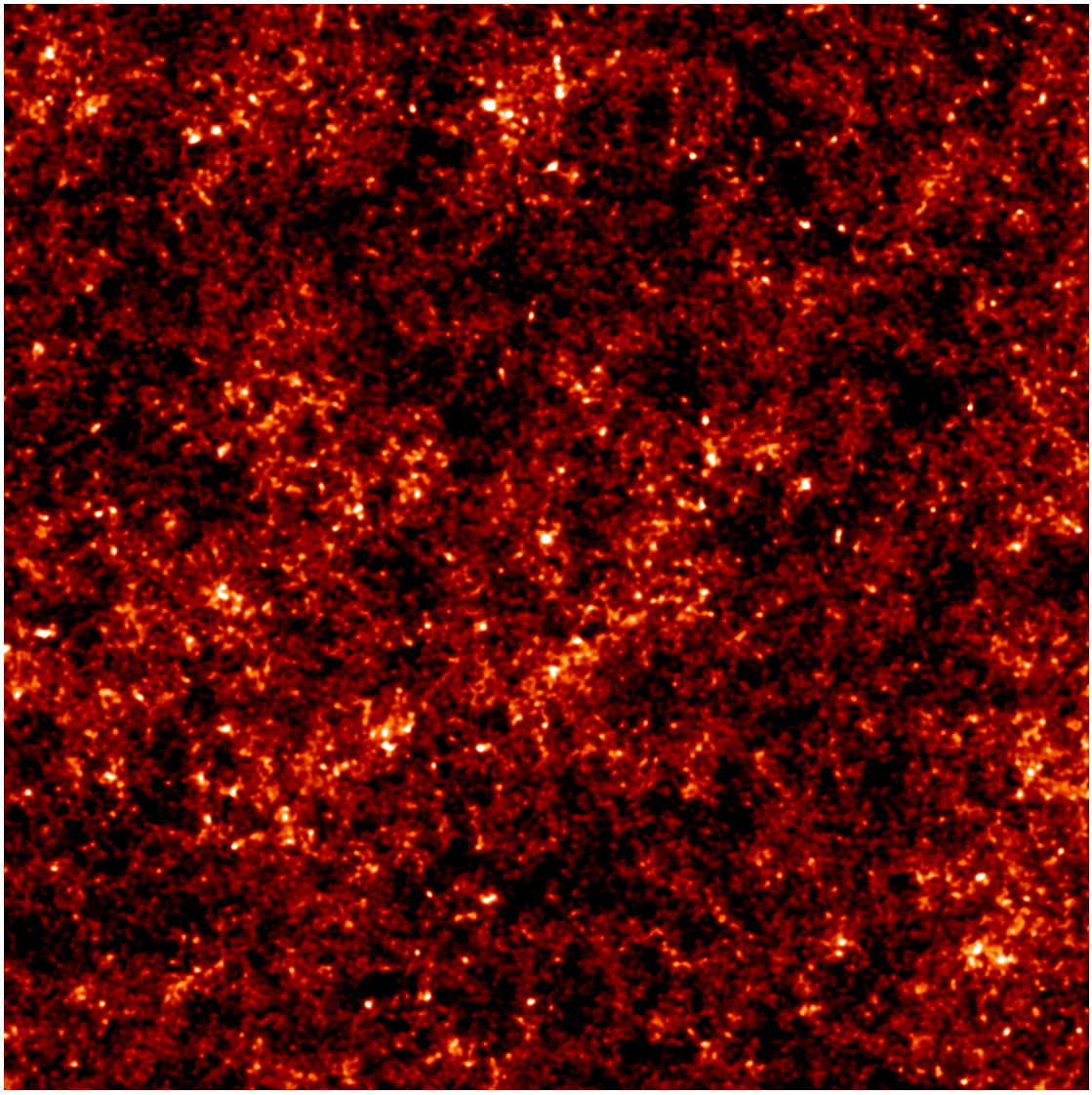

Figure 4.4: 21-cm-based convergence maps for a $5^\circ \times 5^\circ$ field with a $\lambda = 1$ arcmin beam and noise. The colour scale is the same as in Fig. 4.3. The field shown in Figs. 4.1, 4.2, and 4.3 lies at the centre of this map.

low-significance features. This would leave rather little structure visible in our $20' \times 20'$ patch, only the highest peak in the 'ground-based' case. Only a few percent of fields this size would contain an object massive enough to be detected with high significance in a survey with these parameters. This limitation is quite evident in current ground-based lensing surveys (Semboloni et al. 2006; Bacon et al. 2000; Kaiser et al. 2000; Van Waerbeke et al. 2000; Wittman et al. 2000).

In order to give a better impression of the reconstruction capabilities of a radio telescope such as SKA, Fig. 4.4 shows the map of Fig. 4.3b expanded to show a $5^\circ \times 5^\circ$ field. (Note that this is still only 1/4 of the full field we simulated.) Current plans for the SKA

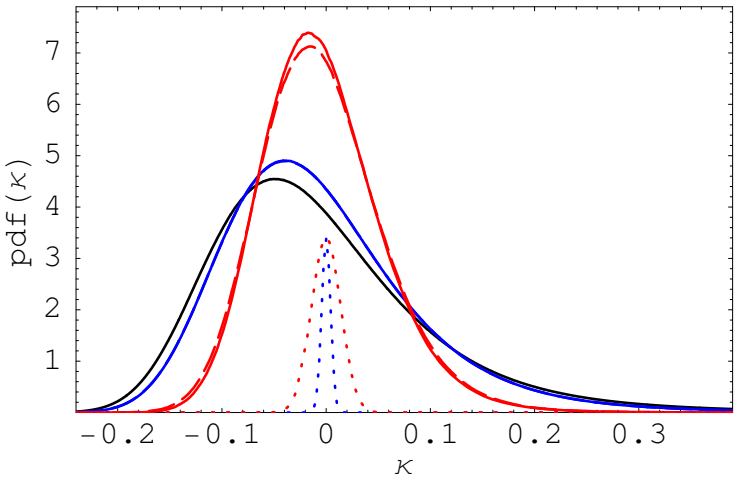

Figure 4.5: The probability density function pdf(κ) of the convergence for sources at $z = 12$ (black line) compared to the distribution smoothed with a Gaussian beam with $\lambda = 6$ arcsec (blue solid curve), and 1 arcmin (red solid curve). The dashed curves show the smoothed distributions with noise added at the irreducible level expected for observations of the pregalactic HI with optimal total bandwidth and frequency resolution. The dotted lines illustrate the noise distributions by themselves.

should enable this resolution to be reached using the dense 'core' array, but the noise level in the convergence map will depend on the way in which reionisation proceeds. If the number density of ionised bubbles is large and they persist for a significant fraction of the redshift range expected for SKA ($7 \lesssim z \lesssim 13$) then noise levels nearly this good can be obtained in 90 days of integration time. A more pessimistic scenario is that reionisation happens very suddenly and nearly uniformly. Even if this is the case, and reionisation occurs near $z \sim 7$, moderate fidelity maps at 1.5 arcmin resolution should be possible and the same noise levels as in Fig. 4.3 should be attainable but on 3 arcmin scales. In the latter case, SKA maps will be more noisy than Fig. 4.3 after 90 days of integration, although still of much higher fidelity than galaxy-based maps.

The conclusion of this section is that galaxy lensing surveys do not provide sufficient signal-to-noise to image any but the most massive individual dark matter structures, but that a very large radio telescope could, in principle, provide high-resolution, high-fidelity images of the cosmic mass distribution in which the halos of individual massive galaxies and galaxy groups are visible.

4.4.2 Pixel distributions

Another useful way to represent the information in our simulated maps is to plot the probability density function for the convergence, pdf(κ), in the different cases. For this we can use the full 10×10 degree field, rather than the smaller subfields discussed in section 4.4.1. Quantitative statistics for all these distributions are given in Table 1.

Figure 4.5 shows the results for sources at $z = 12$, as appropriate for pregalactic HI. This confirms quantitatively our previous conclusion that the irreducible noise has very little effect on the maps. Indeed, its effects are not even visible for a $\lambda = 6$ arcsec beam,

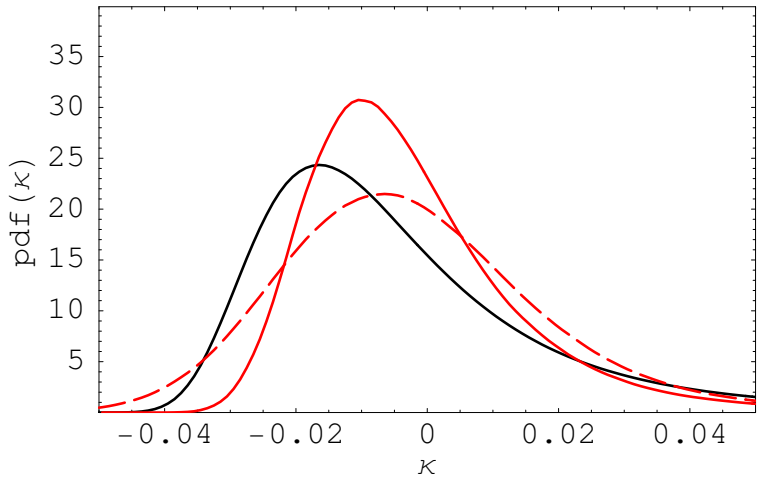

Figure 4.6: The probability density function pdf(κ) of the convergence for an optimistic space-based galaxy lensing survey (median redshift $z_{\rm med} = 1.23$). The unsmoothed, noiseless case is shown in black. The red curves are for Gaussian smoothing of width $\lambda = 1\,$arcmin. The dashed and solid curves are with and without noise respectively. The assumed density of source galaxies is $100\,\mathrm{arcmin}^{-2}$. Note the difference in κ-scale compared to Fig. 4.5.

and they are still small for $\lambda = 1\,$arcmin. This just reflects the fact that the pdfs for the noise are much narrower than those for the signal, as illustrated in Fig. 4.5. Note that the narrower noise pdf is associated with the higher resolution, higher amplitude signal pdf.

Figure 4.6 gives corresponding results for sources with the redshift distribution appropriate to a space-based galaxy lensing survey. Note that the scale has changed from Fig. 4.5, reflecting the substantially lower amplitude of fluctuations in κ in this case. For reconstructions with a beam of width $\lambda = 1\,$arcmin, the noise expected in such a survey has a strong effect on pdf(κ). The low κ tail of the observed distribution is practically all due to noise, and the shape of distribution is largely lost. Estimating the skewness or kurtosis of the underlying distribution would clearly require a very good understanding of the properties of the noise.

The corresponding pdfs for the source redshift distribution and noise appropriate to a ground-based galaxy survey are shown in Fig. 4.7. Here the noise destroys almost all of the information in the original pdf. With a large amount of data and with good knowledge of the systematics one can recover the variance accurately, but determination of higher moments would be extremely challenging.

Even when the noise is high compared to the dispersion in κ, it is still possible to measure the number density of very high mass objects. Figure 4.8 illustrates this point by plotting the high κ tails of the cumulative distribution functions of κ. The noise has relatively little effect on these distributions for $\kappa \gtrsim 0.1$, even for the ground-based galaxy survey case. Such high values have a probability of around $\sim 10^{-3}$ corresponding to of order one object per square degree on the sky. For our space-based survey parameters, the noise becomes unimportant for $\kappa \gtrsim 0.05$, corresponding to roughly 100 objects per square degree.

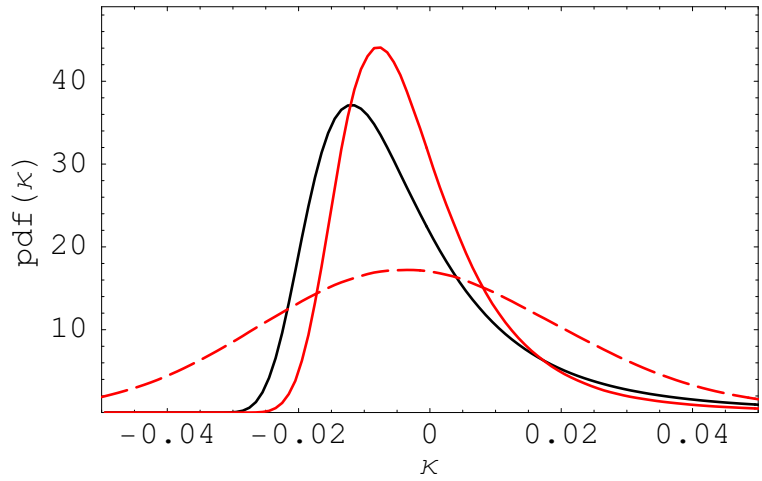

Figure 4.7: The probability density function $\mathrm{pdf}(\kappa)$ of the convergence for an optimistic ground-based galaxy lensing survey (median redshift $z_{\mathrm{med}} = 0.9$). The unsmoothed, noiseless case is shown in black. The red curves are for Gaussian smoothing of width $\lambda = 1\,\mathrm{arcmin}$. The dashed and solid curves are with and without noise respectively. The assumed source density is $35\,\mathrm{arcmin}^{-2}$.

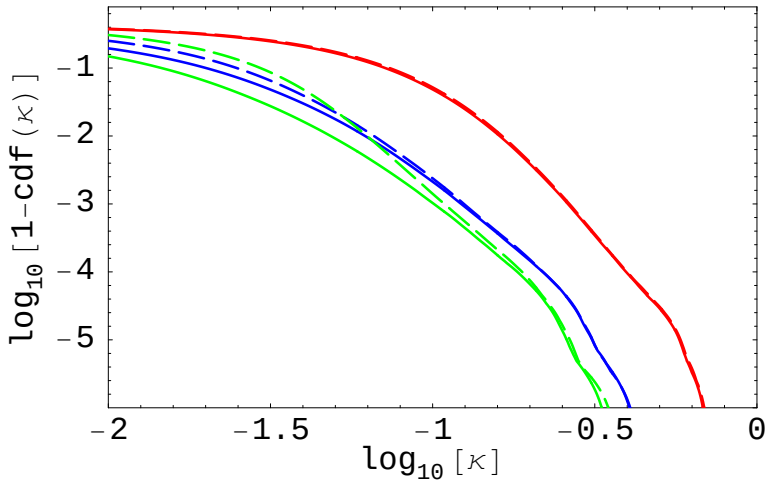

Figure 4.8: The cumulative distribution function $\mathrm{cdf}(\kappa)$ of the convergence for HI at $z \sim 12$ (red curves), for an optimistic space-based galaxy lensing survey (blue curves), and for an optimistic ground-based galaxy lensing survey (green curves). The solid curves represent the distribution with a Gaussian smoothing of width $\lambda = 1\,\mathrm{arcmin}$ and with no noise. The dashed curves are the same but with noise included.

4.5 Conclusion

The noise in a mass map constructed using gravitational lensing of the high-redshift HI distribution is expected to be much smaller than the signal. In addition, the signal-to-noise *increases* with the resolution of the map. It should thus be possible to make high-resolution, high-fidelity images of the dark matter distribution in which the dark halos of individual galaxies and galaxy groups are visible. For example, a very large

Table 4.1: The expected distribution of the convergence κ for future pregalactic HI, space- and ground-based galaxy surveys. For various beam sizes λ and noise levels $\sigma_{\rm N}$, we give the standard deviation σ_κ, the skewness S_3, the 25% quantile $\kappa_{25\%}$, and the 75% quantile $\kappa_{75\%}$ of the convergence distribution. (The mean of κ is zero by definition.)

Survey	λ	$\sigma_{\rm N}$	σ_κ	S_3	$\kappa_{25\%}$	$\kappa_{75\%}$
21-cm,	1 arcsec	–	0.11	1.73	−0.079	0.049
$z_0 = 12$	6 arcsec	–	0.098	1.35	−0.071	0.046
	6 arcsec	0.0042	0.098	1.34	−0.071	0.046
	1 arcmin	–	0.058	0.52	−0.044	0.031
	1 arcmin	0.014	0.060	0.47	−0.045	0.032
space-based,	1 arcsec	–	0.030	3.95	−0.020	0.007
$z_{\rm med} = 1.23$,	1 arcmin	–	0.018	1.99	−0.014	0.006
$n_{\rm g} = 100\,{\rm arcmin}^{-2}$	1 arcmin	0.012	0.022	1.09	−0.017	0.010
ground-based,	1 arcsec	–	0.021	4.61	−0.014	0.005
$z_{\rm med} = 0.9$,	1 arcmin	–	0.014	2.49	−0.011	0.004
$n_{\rm g} = 35\,{\rm arcmin}^{-2}$	1 arcmin	0.02	0.024	0.31	−0.018	0.014

future telescope with baselines $\sim 100\,{\rm km}$ may eventually allow us to detect halos with virial masses $M_{200} \sim 10^{11} h^{-1}\,{\rm M}_\odot$ out to redshift $z \sim 10$ (Metcalf and White 2007). Such detailed observations will provide a very direct and accurate test for structure-formation models. Even with an SKA-like telescope, halos with $M_{200} \gtrsim 10^{13} h^{-1}\,{\rm M}_\odot$ should be clearly detected out to high redshift. This contrasts strongly with mass maps constructed using gravitational lensing of distant galaxies, where high fidelity is only achievable for angular smoothings so large that all but the nearest and most massive individual objects are lost.

Our estimates of the irreducible noise are based on a convergence estimator that is not necessarily optimal. It may therefore be possible to achieve smaller 'irreducible' noise levels than we quote. In practice, however, it is likely that other sources of error will dominate the overall budget, for example, the error introduced by incomplete foreground subtraction (see Furlanetto et al. 2006, for a review). For most purposes, imaging the surface density does not require reaching the irreducible noise limit; the predicted signal is large enough to accommodate a noise level many times the irreducible value. In addition, the noise within a patch of area A goes down like $A^{-1/2}$ while the density fluctuations go down roughly like $A^{-0.15}$, so even if the noise is too large to map the surface density on the scale of a single beam, a high-fidelity map with larger smoothing can still be constructed (as in the galaxy lensing case). The Square Kilometer Array in its currently proposed configuration should be able to map the mass distribution on arcminute scales with moderate to high fidelity if reionisation is not completed too early (Metcalf and White 2007). The optimal bandwidth for observing lensing is $\sim 0.05\,{\rm MHz}$ while the signal-to-noise for mapping the pregalactic HI at the same angular scales is maximal at larger bandwidths $\sim 0.5\,{\rm MHz}$. Lensing benefits from the stacking of many narrow redshift slices even if they are individually noise dominated while the temperature fluctuations themselves get diluted (Metcalf and White 2007). To reach scales of a few

arcseconds as discussed here will require a larger telescope with dense sampling. Given the narrower science goals, this may be achievable with simpler and cheaper antennas.

While high-resolution images of the cosmic mass distribution would be a unique product of observations of 21-cm lensing, they are not the only reason to carry out such studies. If enough of the sky can be surveyed, cosmological parameters such as the density of dark energy and its evolution with redshift can be measured with much higher accuracy by a combination of 21-cm lensing with galaxy lensing than they can by galaxy lensing alone or indeed by any other method proposed so far (Metcalf and White 2007). The baseline configuration of SKA may be powerful enough to achieve much of this improvement if problems with foregrounds can be overcome.

5 Summary and outlook

5.1 Summary

The now widely accepted ΛCDM model of cosmic structure formation provides a consistent explanation for a wide variety of astronomical observations, ranging from the abundance of light elements in our solar system to the temperature fluctuations in the cosmic microwave background radiation. Thanks to ongoing improvements in observational techniques, measurements of gravitational-lensing effects are playing an increasingly important role for testing the model and further constraining its parameters.

The improvements in lensing observations need to be matched by a comparable improvement in the theoretical predictions. Reliable predictions for the lensing properties of the ΛCDM model require detailed numerical simulation. In this thesis, I investigated gravitational lensing in the concordance ΛCDM cosmology by carrying out ray-tracing along past light cones through the Millennium Simulation (Springel et al. 2005). This very large N-body simulation of cosmic structure formation provides excellent statistical predictions for the matter distribution on scales ranging from individual dark-matter halos of galaxies to the large-scale structure. In order to take full advantage of the large volume and the high spatial and mass resolution offered by the simulation, I developed a ray-tracing code that substantially extends previous light-ray-tracing methods, and thereby allows more precise statements about model expectations than has previously been possible.

5.1.1 The magnification distribution and strong-lensing optical depths

In Chapter 2, I discussed the statistical distribution of the distortion of images of distant sources due to gravitational lensing. The results were obtained by tracing random light rays through the Millennium Simulation. The ray distortions induced by the matter in the simulation were calculated by the ray-tracing algorithm as follows: First, the matter distribution on the past light cone of a fiducial observer is constructed from the particle distribution of the simulation. Then, the past light cone is partitioned into a series of redshift slices, and the content of each slice is projected onto a lens plane. Finally, the Multiple-Lens-Plane approximation is used to trace back light rays from the observer through the series of lens planes to the sources.

As a first application of the algorithm, the statistical distribution of the magnification of distant point sources was calculated. The distribution is skewed with a tail toward high magnification and a peak at magnifications below unity, which broadens and moves to lower magnifications with increasing source redshift. The magnification distribution affects the observed luminosity distribution of astronomical standard candles, e.g. type

Ia supernovae. Although magnification effects on the observed luminosity distribution are still small compared to other effects for current samples, they may cause significant systematic errors in future high-redshift, high-precision surveys. So it will be necessary to detect them and to correct for them.

A large part of Chapter 2 was devoted to the study of the statistics of strong-lensing events in the ΛCDM cosmology. In particular, the optical depths for images of sufficiently small sources that are highly magnified, have a large length-to-width ratio, or belong to multiply imaged sources were considered. All these optical depths increase strongly with increasing redshift. It was shown that strong lensing events are almost always caused by a single dominant lensing object, and the mass and redshift distribution of these primary lenses was studied. The observed lens mass range extends to lower masses than those found in earlier studies, which were based on simulations with lower spatial and mass resolution. Furthermore, the effect of material in front of or behind the primary lens was investigated. Although strong-lensing lines-of-sight are indeed biased towards higher than average mean densities, the additional matter typically contributes only a few percent of the total mass along the light path.

5.1.2 The influence of the stellar mass in galaxies

The methods discussed in Chapter 2 were extended in Chapter 3 to investigate how the stellar components of galaxies affect predictions for gravitational lensing in the concordance ΛCDM cosmology. The dark-matter component of the lensing matter was constructed directly from the dark-matter particle distribution of the simulation, while the luminous component was obtained from the semi-analytic galaxy formation models of De Lucia and Blaizot (2007), which were run on stored merger trees from the simulation.

Since the stellar mass is much more concentrated than the dark matter, its inclusion leads to higher mass densities in the very centres of galaxies, and thus may increase strong-lensing cross-sections in these regions. Indeed, it was found that the inclusion of the stellar components greatly enhances the probability for strong lensing compared to a 'dark matter only' universe. The identification of the 'lenses' associated with strong-lensing events reveals that the increase is partly due to a significant enhancement of the strong-lensing cross-section of group and cluster halos. In addition, the stellar matter leads to significant strong lensing in smaller halos, which would not cause noticeable strong lensing otherwise. Apparently, the large abundance of these halos outweighs their small individual cross-sections.

The optical depths for lensing by both the dark and luminous matter are much larger than for lensing by dark matter alone. For images formed at larger distance from the lens centre, however, they become more similar. For images at radii $\geq 5\,\mathrm{arcsec}$, which correspond to image splittings $\gtrsim 10\,\mathrm{arcsec}$, the optical depths differ by at most a factor of two. For radii $\gtrsim 10\,\mathrm{arcsec}$, there is almost no enhancement due to the galaxies in agreement with earlier studies.

The results for strong lensing are consistent with the observed radial distribution of multiply imaged quasars with splittings $\geq 1\,\mathrm{arcsec}$ in the recent SDSS quasar sample of Inada et al. (2008) only if the effect of the galaxies is taken into account. However, the

predicted total number of lensed quasars is still low compared to the observed number, even if the luminous matter is included in the lensings. This may indicate a need to include the effects of baryonic dissipation on the dark matter distribution in order to explain the data fully.

5.1.3 Imaging the cosmic matter distribution

In Chapter 4, I discussed the potential capabilities of future radio telescopes for imaging the cosmic matter distribution. During the epoch of reionization, structure in the pregalactic hydrogen is expected down to kilo-parsec scales, and at each point on the sky there will be ~ 1000 statistically independent regions at different redshifts. These structures could in principle be observed by measuring the 21-cm emission at the corresponding frequencies with a large radio telescope. Gravitational lensing coherently distorts the 21-cm brightness temperature maps at these frequencies and thereby reveals the matter distribution between us and the emitting gas.

I used the Millennium Simulation to simulate large-area maps of the lensing convergence with the noise, resolution and redshift-weighting achievable with a variety of idealised observation programmes. It was found that by measuring lensing effects on the observed image of 21-cm emission during reionization with a sufficiently large radio telescope, an image of the matter distribution could be obtained whose signal-to-noise far exceeds that of any map made using galaxy lensing. These mass images would allow the dark-matter halos of individual galaxies to be viewed directly, giving a wealth of statistical and morphological information about the relative distributions of mass and light. For telescopes like the planned Square Kilometre Array, mass imaging may be possible near the resolution limit of the core array of the telescope. The resulting maps could have a resolution as high as 1 arcmin, and their signal-to-noise ratio could be about four times larger than the ratio of a map with similar resolution obtained using an ambitious space-based galaxy lensing survey.

There is another good reason to use lensing of 21-cm emission from pregalactic hydrogen for mass imaging. There are not many galaxies at high redshift that can be used as sources in lensing surveys. Thus galaxy-lensing surveys are only sensitive to matter structures at low redshift. In contrast, the much higher redshift of the 21-cm emission during reionization allows the detection of structures at redshifts well above unity in 21-cm lensing surveys.

5.2 Outlook

The work presented in this thesis addresses only a small fraction of the problems that could be investigated by ray-tracing through the Millennium Simulation. An obvious extension of the work presented here will be ray-tracing over finite fields to study the effects of lensing on sources with finite extent. With a realistic distribution of source properties, the results could be compared directly with observations of massive galaxy clusters, where many distorted images and multi-image systems have been studied (Broadhurst et al. 2005; Halkola et al. 2006). Such a direct comparison will certainly help to answer

the question whether or not the observed number of giant arcs is consistent with predictions based on the concordance ΛCDM cosmology. When galaxy properties from galaxy formation modelling within the Millennium Simulation (e.g. De Lucia and Blaizot 2007) are combined with such ray-tracing analyses, it will be possible to study whether the dark-halo masses of individual cluster galaxies are consistent with observation, providing an additional observational test of the hierarchical build-up of structure predicted by the standard ΛCDM model.

So far, only the stellar mass and the size information from the semi-analytic galaxy formation models was used. In future work, the morphology and luminosity information could be added to simulate galaxy-galaxy lensing surveys with given selection functions. With improved models of the galaxies, in particular by assuming realistic elliptical mass profiles for the stellar components, such simulated surveys will provide detailed predictions for galaxy-galaxy lensing. For example, ray-tracing over finite fields could then be used to study how well present and future galaxy-galaxy lensing surveys can constrain the mean mass profile and shape of galaxy halos. Furthermore, one could investigate the abilities of weak-lensing surveys to constrain the relation between the large-scale matter and galaxy distributions as characterised by correlation functions and bias factors.

Several physical processes that influence the lensing properties of galaxies and clusters have not been taken into account in this thesis. For example, baryon condensation increases the dark-matter density in the inner parts of halos, and so affects their dark-matter lensing properties (Puchwein et al. 2005; Jing et al. 2006; Rozo et al. 2006). The semi-analytic models used here do not yet describe these processes, but they should be included in future work aiming at higher precision.

There are, of course, questions concerning gravitational lensing that cannot be answered by ray-tracing through the Millennium Simulation. Obviously, predictions for different cosmologies – e.g. ΛCDM models with different parameters, CDM models with an evolving dark energy (Bartelmann et al. 2006), or models with coupled dark matter and dark energy (Farrar and Peebles 2004) – require different structure-formation simulations. However, the methods developed for studying gravitational lensing by ray-tracing through the Millennium Simulation will also be applicable, with the appropriate modifications, to other large N-body and hydrodynamical simulations.

Acknowledgements

First of all, I would like to thank my supervisor Simon White very much for his guidance and support throughout my PhD. I would like to thank Ben Metcalf, Jan Hartlap, and Peter Schneider for our very fruitful collaboration. We are all indebted to the VIRGO people for the Millennium Simulation, without which this work would not have been possible. In particular, I am grateful to Volker Springel for his help, advice, and patience.

I would like to thank Jérémy Blaizot, Gabriella De Lucia, Klaus Dolag, Dimitri Gadotti, Dimitrios Giannios, Eric Hayashi, Manfred Kitzbichler, Gao Liang, Ole Möller, Håvard Sandvik, Björn Malte Schäfer, Anja von der Linden, and all the other people at MPA who helped me in many ways. I would like to thank my colleague and friend Jörn Dunkel, who was always willing to discuss problems related to this work as well as many other interesting scientific problems. Special thanks go to Jens Chluba for giving me so much insight into problems I would have never considered without him.

I would like to thank Matthias Bartelmann, who initiated my interest in gravitational lensing and encouraged me to work in that area of research. Furthermore, I would like thank Guoliang Li, Shude Mao, and Joachim Wambsganss for helpful discussions. I would also like to thank the AIfA people for their hospitality during my visits in Bonn, and for the exciting table tennis matches.

I am grateful for financial support from the MPA and the DFG within the Priority Programme 1177.

Außerdem möchte ich meiner Familie und meinen Freunden danken, die mich all die Jahre nicht nur moralisch und emotional, sondern auch in vielen praktischen Dingen untersützt haben.

Bibliography

Amanullah, R., Mörtsell, E., and Goobar, A., 2003: *Correcting for lensing bias in the Hubble diagram.* A&A, 397, 819

Amara, A., Metcalf, R. B., Cox, T. J., and Ostriker, J. P., 2006: *Simulations of strong gravitational lensing with substructure.* MNRAS, 367, 1367

Bacon, D. J., Refregier, A. R., and Ellis, R. S., 2000: *Detection of weak gravitational lensing by large-scale structure.* MNRAS, 318, 625

Barnes, J. and White, S. D. M., 1984: *The response of a spheroid to a disc field or were bulges ever ellipticals?* MNRAS, 211, 753

Barris, B. J., Tonry, J. L., Blondin, S., Challis, P., Chornock, R., Clocchiatti, A., Filippenko, A. V., Garnavich, P., Holland, S. T., Jha, S., Kirshner, R. P., Krisciunas, K., Leibundgut, B., Li, W., Matheson, T., Miknaitis, G., Riess, A. G., Schmidt, B. P., Smith, R. C., Sollerman, J., Spyromilio, J., Stubbs, C. W., Suntzeff, N. B., Aussel, H., Chambers, K. C., Connelley, M. S., Donovan, D., Henry, J. P., Kaiser, N., Liu, M. C., Martín, E. L., and Wainscoat, R. J., 2004: *Twenty-Three High-Redshift Supernovae from the Institute for Astronomy Deep Survey: Doubling the Supernova Sample at* $z > 0.7$. ApJ, 602, 571

Bartelmann, M. and Weiss, A., 1994: *Arc statistics with realistic cluster potentials. 1: Method and first results.* A&A, 287, 1

Bartelmann, M., Huss, A., Colberg, J. M., Jenkins, A., and Pearce, F. R., 1998: *Arc statistics with realistic cluster potentials. IV. Clusters in different cosmologies.* A&A, 330, 1

Bartelmann, M., Doran, M., and Wetterich, C., 2006: *Non-linear structure formation in cosmologies with early dark energy.* A&A, 454, 27

Beaulieu, J.-P., Bennett, D. P., Fouqué, P., Williams, A., Dominik, M., Jorgensen, U. G., Kubas, D., Cassan, A., Coutures, C., Greenhill, J., Hill, K., Menzies, J., Sackett, P. D., Albrow, M., Brillant, S., Caldwell, J. A. R., Calitz, J. J., Cook, K. H., Corrales, E., Desort, M., Dieters, S., Dominis, D., Donatowicz, J., Hoffman, M., Kane, S., Marquette, J.-B., Martin, R., Meintjes, P., Pollard, K., Sahu, K., Vinter, C., Wambsganss, J., Woller, K., Horne, K., Steele, I., Bramich, D. M., Burgdorf, M., Snodgrass, C., Bode, M., Udalski, A., Szymański, M. K., Kubiak, M., Więckowski, T., Pietrzyński, G., Soszyński, I., Szewczyk, O., Wyrzykowski, Ł., Paczyński, B., Abe,

F., Bond, I. A., Britton, T. R., Gilmore, A. C., Hearnshaw, J. B., Itow, Y., Kamiya, K., Kilmartin, P. M., Korpela, A. V., Masuda, K., Matsubara, Y., Motomura, M., Muraki, Y., Nakamura, S., Okada, C., Ohnishi, K., Rattenbury, N. J., Sako, T., Sato, S., Sasaki, M., Sekiguchi, T., Sullivan, D. J., Tristram, P. J., Yock, P. C. M., and Yoshioka, T., 2006: *Discovery of a cool planet of 5.5 Earth masses through gravitational microlensing.* Nature, 439, 437

Benjamin, J., Heymans, C., Semboloni, E., van Waerbeke, L., Hoekstra, H., Erben, T., Gladders, M. D., Hetterscheidt, M., Mellier, Y., and Yee, H. K. C., 2007: *Cosmological constraints from the 100 deg^2 weak-lensing survey.* MNRAS, 381, 702

Bertschinger, E., 1998: *Simulations of Structure Formation in the Universe.* ARA&A, 36, 599

Blandford, R. and Narayan, R., 1986: *Fermat's principle, caustics, and the classification of gravitational lens images.* ApJ, 310, 568

Blandford, R. D., Saust, A. B., Brainerd, T. G., and Villumsen, J. V., 1991: *The distortion of distant galaxy images by large-scale structure.* MNRAS, 251, 600

Blumenthal, G. R., Faber, S. M., Flores, R., and Primack, J. R., 1986: *Contraction of dark matter galactic halos due to baryonic infall.* ApJ, 301, 27

Bolton, A. S., Burles, S., Koopmans, L. V. E., Treu, T., and Moustakas, L. A., 2006: *The Sloan Lens ACS Survey. I. A Large Spectroscopically Selected Sample of Massive Early-Type Lens Galaxies.* ApJ, 638, 703

Bond, I. A., Udalski, A., Jaroszyński, M., Rattenbury, N. J., Paczyński, B., Soszyński, I., Wyrzykowski, L., Szymański, M. K., Kubiak, M., Szewczyk, O., Żebruń, K., Pietrzyński, G., Abe, F., Bennett, D. P., Eguchi, S., Furuta, Y., Hearnshaw, J. B., Kamiya, K., Kilmartin, P. M., Kurata, Y., Masuda, K., Matsubara, Y., Muraki, Y., Noda, S., Okajima, K., Sako, T., Sekiguchi, T., Sullivan, D. J., Sumi, T., Tristram, P. J., Yanagisawa, T., and Yock, P. C. M., 2004: *OGLE 2003-BLG-235/MOA 2003-BLG-53: A Planetary Microlensing Event.* ApJ, 606, L155

Bourassa, R. R. and Kantowski, R., 1975: *The theory of transparent gravitational lenses.* ApJ, 195, 13

Bower, R. G., Benson, A. J., Malbon, R., Helly, J. C., Frenk, C. S., Baugh, C. M., Cole, S., and Lacey, C. G., 2006: *Breaking the hierarchy of galaxy formation.* MNRAS, 370, 645

Bradač, M., Schneider, P., Lombardi, M., Steinmetz, M., Koopmans, L. V. E., and Navarro, J. F., 2004: *The signature of substructure on gravitational lensing in the ΛCDM cosmological model.* A&A, 423, 797

Bradač, M., Schneider, P., Lombardi, M., and Erben, T., 2005: *Strong and weak lensing united.* A&A, 437, 39

Brainerd, T. G., Blandford, R. D., and Smail, I., 1996: *Weak Gravitational Lensing by Galaxies.* ApJ, 466, 623

Broadhurst, T., Benítez, N., Coe, D., Sharon, K., Zekser, K., White, R., Ford, H., Bouwens, R., Blakeslee, J., Clampin, M., Cross, N., Franx, M., Frye, B., Hartig, G., Illingworth, G., Infante, L., Menanteau, F., Meurer, G., Postman, M., Ardila, D. R., Bartko, F., Brown, R. A., Burrows, C. J., Cheng, E. S., Feldman, P. D., Golimowski, D. A., Goto, T., Gronwall, C., Herranz, D., Holden, B., Homeier, N., Krist, J. E., Lesser, M. P., Martel, A. R., Miley, G. K., Rosati, P., Sirianni, M., Sparks, W. B., Steindling, S., Tran, H. D., Tsvetanov, Z. I., and Zheng, W., 2005: *Strong-Lensing Analysis of A1689 from Deep Advanced Camera Images.* ApJ, 621, 53

Cabanac, R. A., Alard, C., Dantel-Fort, M., Fort, B., Gavazzi, R., Gomez, P., Kneib, J. P., Le Fèvre, O., Mellier, Y., Pello, R., Soucail, G., Sygnet, J. F., and Valls-Gabaud, D., 2007: *The CFHTLS strong lensing legacy survey. I. Survey overview and T0002 release sample.* A&A, 461, 813

Cardone, V. F., 2004: *The lensing properties of the Sersic model.* A&A, 415, 839

Cavendish, H., ca. 1784: unpublished (see Thorpe et al. 1921)

Chae, K.-H., 2007: *Cosmological Parameters from the SDSS DR5 Velocity Dispersion Function of Early-Type Galaxies through Radio-selected Lens Statistics.* ApJ, 658, L71

Chang, K. and Refsdal, S., 1979: *Flux variations of QSO 0957+561 A, B and image splitting by stars near the light path.* Nature, 282, 561

Chang, K. and Refsdal, S., 1984: *Star disturbances in gravitational lens galaxies.* A&A, 132, 168

Chwolson, O., 1924: *Über eine mögliche Form fiktiver Doppelsterne.* Astronomische Nachrichten, 221(20), 329

Clowe, D., Bradač, M., Gonzalez, A. H., Markevitch, M., Randall, S. W., Jones, C., and Zaritsky, D., 2006: *A Direct Empirical Proof of the Existence of Dark Matter.* ApJ, 648, L109

Comerford, J. M., Meneghetti, M., Bartelmann, M., and Schirmer, M., 2006: *Mass Distributions of Hubble Space Telescope Galaxy Clusters from Gravitational Arcs.* ApJ, 642, 39

Cooley, J. W. and Tukey, J. W., 1965: *An Algorithm for the Machine Calculation of Complex Fourier Series.* Math. Comput., 19(90), 297

Croom, S. M., Smith, R. J., Boyle, B. J., Shanks, T., Miller, L., Outram, P. J., and Loaring, N. S., 2004: *The 2dF QSO Redshift Survey - XII. The spectroscopic catalogue and luminosity function.* MNRAS, 349, 1397

Croton, D. J., Springel, V., White, S. D. M., De Lucia, G., Frenk, C. S., Gao, L., Jenkins, A., Kauffmann, G., Navarro, J. F., and Yoshida, N., 2006: *The many lives of active galactic nuclei: cooling flows, black holes and the luminosities and colours of galaxies.* MNRAS, 365, 11

Dalal, N. and Kochanek, C. S., 2002: *Direct Detection of Cold Dark Matter Substructure.* ApJ, 572, 25

Dalal, N., Holder, G., and Hennawi, J. F., 2004: *Statistics of Giant Arcs in Galaxy Clusters.* ApJ, 609, 50

Dashevskii, V. M. and Slysh, V. I., 1965: *On the Propagation of Light in a Nonhomogeneous Universe.* AZh, 42, 863. (English translation in Dashevskii and Slysh 1966)

Dashevskii, V. M. and Slysh, V. I., 1966: *On the Propagation of Light in a Nonhomogeneous Universe.* Soviet Astronomy, 9, 671. (English translation of Dashevskii and Slysh 1965)

Dashevskii, V. M. and Zel'Dovich, Y. B., 1964: *Propagation of Light in a Nonhomogeneous Nonflat Universe II.* AZh, 41, 1071. (English translation in Dashevskii and Zel'Dovich 1965)

Dashevskii, V. M. and Zel'Dovich, Y. B., 1965: *Propagation of Light in a Nonhomogeneous Nonflat Universe II.* Soviet Astronomy, 8, 854. (English translation of Dashevskii and Zel'Dovich 1964)

De Lucia, G. and Blaizot, J., 2007: *The hierarchical formation of the brightest cluster galaxies.* MNRAS, 375, 2

De Lucia, G., Springel, V., White, S. D. M., Croton, D., and Kauffmann, G., 2006: *The formation history of elliptical galaxies.* MNRAS, 366, 499

de Vaucouleurs, G., 1948: *Recherches sur les Nebuleuses Extragalactiques.* Annales d'Astrophysique, 11, 247

Dodelson, S. and Vallinotto, A., 2006: *Learning from the scatter in type Ia supernovae.* Phys. Rev. D, 74(6), 063515

Dolag, K., Bartelmann, M., Perrotta, F., Baccigalupi, C., Moscardini, L., Meneghetti, M., and Tormen, G., 2004: *Numerical study of halo concentrations in dark-energy cosmologies.* A&A, 416, 853

Dyer, C. C. and Roeder, R. C., 1972: *The Distance-Redshift Relation for Universes with no Intergalactic Medium.* ApJ, 174, L115

Dyer, C. C. and Roeder, R. C., 1973: *Distance-Redshift Relations for Universes with Some Intergalactic Medium.* ApJ, 180, L31

Dyer, C. C. and Roeder, R. C., 1974: *Observations in Locally Inhomogeneous Cosmological Models.* ApJ, 189, 167

Dyson, F. W., Eddington, A. S., and Davidson, C., 1920: *A Determination of the Deflection of Light by the Sun's Gravitational Field, from Observations Made at the Total Eclipse of May 29, 1919.* Philos. Trans. R. Soc. A, 220, 291

Eddington, A. S., 1920: *Space, time and gravitation. an outline of the general relativity theory.* Cambridge Science Classics, Cambridge: University Press, 1920

Egami, E., Kneib, J.-P., Rieke, G. H., Ellis, R. S., Richard, J., Rigby, J., Papovich, C., Stark, D., Santos, M. R., Huang, J.-S., Dole, H., Le Floc'h, E., and Pérez-González, P. G., 2005: *Spitzer and Hubble Space Telescope Constraints on the Physical Properties of the z˜7 Galaxy Strongly Lensed by A2218.* ApJ, 618, L5

Einstein, A., 1911: *Über den Einfluß der Schwerkraft auf die Ausbreitung des Lichtes.* Annalen der Physik, 340, 898

Einstein, A., 1915: *Erklärung der Perihelbewegung des Merkur aus der allgemeinen Relativitätstheorie.* Sitzungsberichte der Königlich Preußischen Akademie der Wissenschaften (Berlin), pp. 831–839. (see also Einstein 1916)

Einstein, A., 1916: *Die Grundlage der allgemeinen Relativitätstheorie.* Annalen der Physik, 354, 769

Einstein, A., 1936: *Lens-Like Action of a Star by the Deviation of Light in the Gravitational Field.* Science, 84, 506

Evans, N. W. and Witt, H. J., 2003: *Fitting gravitational lenses: truth or delusion.* MNRAS, 345, 1351

Farrar, G. R. and Peebles, P. J. E., 2004: *Interacting Dark Matter and Dark Energy.* ApJ, 604, 1

Fedeli, C., Bartelmann, M., Meneghetti, M., and Moscardini, L., 2007: *Effects of the halo concentration distribution on strong-lensing optical depth and X-ray emission.* A&A, 473, 715

Fluke, C. J., Webster, R. L., and Mortlock, D. J., 2002: *Investigating cosmological weak lensing with the ray-bundle method.* MNRAS, 331, 180

Fomalont, E. B. and Sramek, R. A., 1976: *Measurements of the solar gravitational deflection of radio waves in agreement with general relativity.* Physical Review Letters, 36, 1475

Franx, M., Illingworth, G. D., Kelson, D. D., van Dokkum, P. G., and Tran, K.-V., 1997: *A Pair of Lensed Galaxies at z=4.92 in the Field of CL 1358+62.* ApJ, 486, L75

Frenk, C. S., White, S. D. M., Bode, P., Bond, J. R., Bryan, G. L., Cen, R., Couchman, H. M. P., Evrard, A. E., Gnedin, N., Jenkins, A., Khokhlov, A. M., Klypin, A., Navarro, J. F., Norman, M. L., Ostriker, J. P., Owen, J. M., Pearce, F. R., Pen, U.-L., Steinmetz, M., Thomas, P. A., Villumsen, J. V., Wadsley, J. W., Warren, M. S.,

Xu, G., and Yepes, G., 1999: *The Santa Barbara Cluster Comparison Project: A Comparison of Cosmological Hydrodynamics Solutions.* ApJ, 525, 554

Frigo, M. and Johnson, S. G., 2005: *The Design and Implementation of FFTW3.* Proc. IEEE, 93(2), 216

Furlanetto, S. R., Oh, S. P., and Briggs, F. H., 2006: *Cosmology at low frequencies: The 21 cm transition and the high-redshift Universe.* Phys. Rep., 433, 181

Gao, L., Springel, V., and White, S. D. M., 2005: *The age dependence of halo clustering.* MNRAS, 363, L66

Gaudi, B. S., 2007: *Microlensing Searches for Planets: Results and Future Prospects.* ArXiv e-prints, 711.1614

Gladders, M. D., Hoekstra, H., Yee, H. K. C., Hall, P. B., and Barrientos, L. F., 2003: *The Incidence of Strong-Lensing Clusters in the Red-Sequence Cluster Survey.* ApJ, 593, 48

Gnedin, O. Y., Kravtsov, A. V., Klypin, A. A., and Nagai, D., 2004: *Response of Dark Matter Halos to Condensation of Baryons: Cosmological Simulations and Improved Adiabatic Contraction Model.* ApJ, 616, 16

Gott, J. R., III, 1981: *Are heavy halos made of low mass stars - A gravitational lens test.* ApJ, 243, 140

Gould, A., Udalski, A., An, D., Bennett, D. P., Zhou, A.-Y., Dong, S., Rattenbury, N. J., Gaudi, B. S., Yock, P. C. M., Bond, I. A., Christie, G. W., Horne, K., Anderson, J., Stanek, K. Z., DePoy, D. L., Han, C., McCormick, J., Park, B.-G., Pogge, R. W., Poindexter, S. D., Soszyński, I., Szymański, M. K., Kubiak, M., Pietrzyński, G., Szewczyk, O., Wyrzykowski, Ł., Ulaczyk, K., Paczyński, B., Bramich, D. M., Snodgrass, C., Steele, I. A., Burgdorf, M. J., Bode, M. F., Botzler, C. S., Mao, S., and Swaving, S. C., 2006: *Microlens OGLE-2005-BLG-169 Implies That Cool Neptune-like Planets Are Common.* ApJ, 644, L37

Gunn, J. E., 1967a: *A Fundamental Limitation on the Accuracy of Angular Measurements in Observational Cosmology.* ApJ, 147, 61

Gunn, J. E., 1967b: *On the Propagation of Light in Inhomogeneous Cosmologies. I. Mean Effects.* ApJ, 150, 737

Halkola, A., Seitz, S., and Pannella, M., 2006: *Parametric strong gravitational lensing analysis of Abell 1689.* MNRAS, 372, 1425

Hennawi, J. F., Dalal, N., and Bode, P., 2007a: *Statistics of Quasars Multiply Imaged by Galaxy Clusters.* ApJ, 654, 93

Hennawi, J. F., Dalal, N., Bode, P., and Ostriker, J. P., 2007b: *Characterizing the Cluster Lens Population.* ApJ, 654, 714

Hernquist, L., 1990: *An analytical model for spherical galaxies and bulges.* ApJ, 356, 359

Hetterscheidt, M., Simon, P., Schirmer, M., Hildebrandt, H., Schrabback, T., Erben, T., and Schneider, P., 2007: *GaBoDS: The Garching-Bonn deep survey. VII. Cosmic shear analysis.* A&A, 468, 859

Hewitt, J. N., Turner, E. L., Schneider, D. P., Burke, B. F., and Langston, G. I., 1988: *Unusual radio source MG1131+0456 - A possible Einstein ring.* Nature, 333, 537

Hilbert, S., Metcalf, R. B., and White, S. D. M., 2007a: *Imaging the cosmic matter distribution using gravitational lensing of pre-galactic HI.* MNRAS, 382, 1494

Hilbert, S., White, S. D. M., Hartlap, J., and Schneider, P., 2007b: *Strong lensing optical depths in a ΛCDM universe.* MNRAS, 382, 121

Hilbert, S., White, S. D. M., Hartlap, J., and Schneider, P., 2008: *Strong lensing optical depths in a ΛCDM universe II: The influence of the stellar mass in galaxies.* MNRAS. (in press)

Hoekstra, H., van Waerbeke, L., Gladders, M. D., Mellier, Y., and Yee, H. K. C., 2002: *Weak Lensing Study of Galaxy Biasing.* ApJ, 577, 604

Hoekstra, H., Mellier, Y., van Waerbeke, L., Semboloni, E., Fu, L., Hudson, M. J., Parker, L. C., Tereno, I., and Benabed, K., 2006: *First Cosmic Shear Results from the Canada-France-Hawaii Telescope Wide Synoptic Legacy Survey.* ApJ, 647, 116

Holz, D. E., 1998: *Lensing and High-z Supernova Surveys.* ApJ, 506, L1

Horesh, A., Ofek, E. O., Maoz, D., Bartelmann, M., Meneghetti, M., and Rix, H.-W., 2005: *The Lensed Arc Production Efficiency of Galaxy Clusters: A Comparison of Matched Observed and Simulated Samples.* ApJ, 633, 768

Hubble, E., 1929: *A Relation between Distance and Radial Velocity among Extra-Galactic Nebulae.* Proceedings of the National Academy of Science, 15, 168

Huterer, D., Keeton, C. R., and Ma, C.-P., 2005: *Effects of Ellipticity and Shear on Gravitational Lens Statistics.* ApJ, 624, 34

Inada, N., Oguri, M., Becker, R. H., Shin, M.-S., Richards, G. T., Hennawi, J. F., White, R. L., Pindor, B., Strauss, M. A., Kochanek, C. S., Johnston, D. E., Gregg, M. D., Kayo, I., Eisenstein, D., Hall, P. B., Castander, F. J., Clocchiatti, A., Anderson, S. F., Schneider, D. P., York, D. G., Lupton, R., Chiu, K., Kawano, Y., Scranton, R., Frieman, J. A., Keeton, C. R., Morokuma, T., Rix, H.-W., Turner, E. L., Burles, S., Brunner, R. J., Sheldon, E. S., Bahcall, N. A., and Masataka, F., 2008: *The Sloan Digital Sky Survey Quasar Lens Search. II. Statistical Lens Sample from the Third Data Release.* AJ, 135, 496

Irwin, M. J., Webster, R. L., Hewett, P. C., Corrigan, R. T., and Jedrzejewski, R. I., 1989: *Photometric variations in the Q2237 + 0305 system - First detection of a microlensing event.* AJ, 98, 1989

Jain, B., Seljak, U., and White, S., 2000: *Ray-tracing Simulations of Weak Lensing by Large-Scale Structure.* ApJ, 530, 547

Jaki, S. L., 1978: *Johann Georg von Soldner and the gravitational bending of light, with an English translation of his essay on it published in 1801.* Foundations of Physics, 8, 927

Jing, Y. P., Zhang, P., Lin, W. P., Gao, L., and Springel, V., 2006: *The Influence of Baryons on the Clustering of Matter and Weak-Lensing Surveys.* ApJ, 640, L119

Jönsson, J., Dahlén, T., Goobar, A., Gunnarsson, C., Mörtsell, E., and Lee, K., 2006: *Lensing Magnification of Supernovae in the GOODS Fields.* ApJ, 639, 991

Kaiser, N. and Squires, G., 1993: *Mapping the dark matter with weak gravitational lensing.* ApJ, 404, 441

Kaiser, N., Squires, G., and Broadhurst, T., 1995: *A Method for Weak Lensing Observations.* ApJ, 449, 460

Kaiser, N., Wilson, G., and Luppino, G. A., 2000: *Large-Scale Cosmic Shear Measurements.* ArXiv Astrophysics e-prints, astro-ph/0003338

Kantowski, R., 1969: *Corrections in the Luminosity-Redshift Relations of the Homogeneous Friedmann Models.* ApJ, 155, 89

Kayser, R., Refsdal, S., and Stabell, R., 1986: *Astrophysical applications of gravitational micro-lensing.* A&A, 166, 36

Keeton, C. R., 2003: *Analytic Cross Sections for Substructure Lensing.* ApJ, 584, 664

Klimov, Y. G., 1963: *Occulted Galaxies and an Experimental Verification of the General Theory of Relativity.* AZh, 40, 874. (English translation in Klimov 1964)

Klimov, Y. G., 1964: *Occulted Galaxies and an Experimental Verification of the General Theory of Relativity.* Soviet Astronomy, 7, 664. (English translation of Klimov 1963)

Kneib, J.-P., Ellis, R. S., Smail, I., Couch, W. J., and Sharples, R. M., 1996: *Hubble Space Telescope Observations of the Lensing Cluster Abell 2218.* ApJ, 471, 643

Knop, R. A., Aldering, G., Amanullah, R., Astier, P., Blanc, G., Burns, M. S., Conley, A., Deustua, S. E., Doi, M., Ellis, R., Fabbro, S., Folatelli, G., Fruchter, A. S., Garavini, G., Garmond, S., Garton, K., Gibbons, R., Goldhaber, G., Goobar, A., Groom, D. E., Hardin, D., Hook, I., Howell, D. A., Kim, A. G., Lee, B. C., Lidman, C., Mendez, J., Nobili, S., Nugent, P. E., Pain, R., Panagia, N., Pennypacker, C. R., Perlmutter, S., Quimby, R., Raux, J., Regnault, N., Ruiz-Lapuente, P., Sainton, G., Schaefer, B., Schahmaneche, K., Smith, E., Spadafora, A. L., Stanishev, V., Sullivan, M., Walton, N. A., Wang, L., Wood-Vasey, W. M., and Yasuda, N., 2003: *New Constraints on $\Omega_{\rm M}$, Ω_Λ, and w from an Independent Set of 11 High-Redshift Supernovae Observed with the Hubble Space Telescope.* ApJ, 598, 102

Kochanek, C. S., 2006: *Part 2: Strong gravitational lensing.* In: Meylan, G., Jetzer, P., North, P., Schneider, P., Kochanek, C. S., and Wambsganss, J. (eds.), *Saas-Fee Advanced Course 33: Gravitational Lensing: Strong, Weak and Micro*, pp. 91–268. Springer, Berlin

Langston, G. I., Schneider, D. P., Conner, S., Carilli, C. L., Lehar, J., Burke, B. F., Turner, E. L., Gunn, J. E., Hewitt, J. N., and Schmidt, M., 1989: *MG 1654+1346 - an Einstein Ring image of a quasar radio lobe.* AJ, 97, 1283

Lemson, G. and the Virgo Consortium, 2006: *Halo and Galaxy Formation Histories from the Millennium Simulation: Public release of a VO-oriented and SQL-queryable database for studying the evolution of galaxies in the LambdaCDM cosmogony.* ArXiv Astrophysics e-prints, astro-ph/0608019

Li, G.-L., Mao, S., Jing, Y. P., Bartelmann, M., Kang, X., and Meneghetti, M., 2005: *Is the Number of Giant Arcs in ΛCDM Consistent with Observations?* ApJ, 635, 795

Li, G. L., Mao, S., Jing, Y. P., Mo, H. J., Gao, L., and Lin, W. P., 2006: *The giant arc statistics in the three-year Wilkinson Microwave Anisotropy Probe cosmological model.* MNRAS, 372, L73

Liebes, S., 1964: *Gravitational lenses.* Phys. Rev., 133(3B), B835

Limousin, M., Richard, J., Jullo, E., Kneib, J.-P., Fort, B., Soucail, G., Elíasdóttir, Á., Natarajan, P., Ellis, R. S., Smail, I., Czoske, O., Smith, G. P., Hudelot, P., Bardeau, S., Ebeling, H., Egami, E., and Knudsen, K. K., 2007: *Combining Strong and Weak Gravitational Lensing in Abell 1689.* ApJ, 668, 643

Logdge, O. J., 1919: *"gravitation and light".* Nature, 104, 354

Luppino, G. A., Gioia, I. M., Hammer, F., Le Fèvre, O., and Annis, J. A., 1999: *A search for gravitational lensing in 38 X-ray selected clusters of galaxies.* A&AS, 136, 117

Lynds, R. and Petrosian, V., 1986: *Giant Luminous Arcs in Galaxy Clusters.* Bulletin of the American Astronomical Society, 18, 1014

Macciò, A. V., Moore, B., Stadel, J., and Diemand, J., 2006: *Radial distribution and strong lensing statistics of satellite galaxies and substructure using high-resolution ΛCDM hydrodynamical simulations.* MNRAS, 366, 1529

Mandelbaum, R., Seljak, U., Cool, R. J., Blanton, M., Hirata, C. M., and Brinkmann, J., 2006a: *Density profiles of galaxy groups and clusters from SDSS galaxy-galaxy weak lensing.* MNRAS, 372, 758

Mandelbaum, R., Seljak, U., Kauffmann, G., Hirata, C. M., and Brinkmann, J., 2006b: *Galaxy halo masses and satellite fractions from galaxy-galaxy lensing in the Sloan Digital Sky Survey: stellar mass, luminosity, morphology and environment dependencies.* MNRAS, 368, 715

Mao, S. and Paczynski, B., 1991: *Gravitational microlensing by double stars and planetary systems.* ApJ, 374, L37

Mao, S. and Schneider, P., 1998: *Evidence for substructure in lens galaxies?* MNRAS, 295, 587

Maoz, D. and Rix, H.-W., 1993: *Early-Type Galaxies, Dark Halos, and Gravitational Lensing Statistics.* ApJ, 416, 425

Massey, R., Rhodes, J., Ellis, R., Scoville, N., Leauthaud, A., Finoguenov, A., Capak, P., Bacon, D., Aussel, H., Kneib, J.-P., Koekemoer, A., McCracken, H., Mobasher, B., Pires, S., Refregier, A., Sasaki, S., Starck, J.-L., Taniguchi, Y., Taylor, A., and Taylor, J., 2007a: *Dark matter maps reveal cosmic scaffolding.* Nature, 445, 286

Massey, R., Rhodes, J., Leauthaud, A., Capak, P., Ellis, R., Koekemoer, A., Réfrégier, A., Scoville, N., Taylor, J. E., Albert, J., Bergé, J., Heymans, C., Johnston, D., Kneib, J.-P., Mellier, Y., Mobasher, B., Semboloni, E., Shopbell, P., Tasca, L., and Van Waerbeke, L., 2007b: *COSMOS: Three-dimensional Weak Lensing and the Growth of Structure.* ApJS, 172, 239

Meneghetti, M., Bolzonella, M., Bartelmann, M., Moscardini, L., and Tormen, G., 2000: *Effects of cluster galaxies on arc statistics.* MNRAS, 314, 338

Meneghetti, M., Bartelmann, M., and Moscardini, L., 2003: *cD galaxy contribution to the strong lensing cross-sections of galaxy clusters.* MNRAS, 346, 67

Meneghetti, M., Jain, B., Bartelmann, M., and Dolag, K., 2005: *Constraints on dark energy models from galaxy clusters with multiple arcs.* MNRAS, 362, 1301

Meneghetti, M., Argazzi, R., Pace, F., Moscardini, L., Dolag, K., Bartelmann, M., Li, G., and Oguri, M., 2007: *Arc sensitivity to cluster ellipticity, asymmetries, and substructures.* A&A, 461, 25

Metcalf, R. B., 1999: *Gravitational lensing of high-redshift Type IA supernovae: a probe of medium-scale structure.* MNRAS, 305, 746

Metcalf, R. B. and Silk, J., 1999: *A Fundamental Test of the Nature of Dark Matter.* ApJ, 519, L1

Metcalf, R. B. and White, S. D. M., 2007: *High-resolution imaging of the cosmic mass distribution from gravitational lensing of pre-galactic HI.* MNRAS, 381, 447

Metcalf, R. B. and Zhao, H., 2002: *Flux Ratios as a Probe of Dark Substructures in Quadruple-Image Gravitational Lenses.* ApJ, 567, L5

Minty, E. M., Heavens, A. F., and Hawkins, M. R. S., 2002: *Testing dark matter with high-redshift supernovae.* MNRAS, 330, 378

Möller, O. and Blain, A. W., 1998: *Strong gravitational lensing by spiral galaxies.* MNRAS, 299, 845

Möller, O. and Blain, A. W., 2001: *Strong gravitational lensing by multiple galaxies.* MNRAS, 327, 339

Möller, O., Kitzbichler, M., and Natarajan, P., 2007: *Strong lensing statistics in large, $z \lesssim 0.2$, surveys: bias in the lens galaxy population.* MNRAS, 379, 1195

Munshi, D. and Valageas, P., 2006: *How many SNeIa do we need to detect the effect of weak lensing ?* ArXiv Astrophysics e-prints, astro-ph/0601683

Myers, S. T., Jackson, N. J., Browne, I. W. A., de Bruyn, A. G., Pearson, T. J., Readhead, A. C. S., Wilkinson, P. N., Biggs, A. D., Blandford, R. D., Fassnacht, C. D., Koopmans, L. V. E., Marlow, D. R., McKean, J. P., Norbury, M. A., Phillips, P. M., Rusin, D., Shepherd, M. C., and Sykes, C. M., 2003: *The Cosmic Lens All-Sky Survey - I. Source selection and observations.* MNRAS, 341, 1

Narayan, R. and White, S. D. M., 1988: *Gravitational lensing in a cold dark matter universe.* MNRAS, 231, 97P

Natarajan, P., De Lucia, G., and Springel, V., 2007: *Substructure in lensing clusters and simulations.* MNRAS, 376, 180

Navarro, J. F., Frenk, C. S., and White, S. D. M., 1997: *A Universal Density Profile from Hierarchical Clustering.* ApJ, 490, 493

Newton, I., 1704: *Opticks: Or, a Treatise of the Reflections, Refractions, Inflections and Colours of Light. Also Two Treatises of the Species and Magnitude of Curvilinear Figures.* Printed for Sam. Smith. and Benj. Walford, Printers to the Royal Society, at the Prince's Arms of St. Pauls Curch-yard, London, 1st edn.

Nityananda, R. and Ostriker, J. P., 1984: *Gravitational lensing by stars in a galaxy halo - Theory of combined weak and strong scattering.* Journal of Astrophysics and Astronomy, 5, 235

Norman, M. L., Bryan, G. L., Harkness, R., Bordner, J., Reynolds, D., O'Shea, B., and Wagner, R., 2007: *Simulating Cosmological Evolution with Enzo.* ArXiv e-prints, 705.1556

Oguri, M., 2006: *The image separation distribution of strong lenses: halo versus subhalo populations.* MNRAS, 367, 1241

Oguri, M., Lee, J., and Suto, Y., 2003: *Arc Statistics in Triaxial Dark Matter Halos: Testing the Collisionless Cold Dark Matter Paradigm.* ApJ, 599, 7

Oguri, M., Inada, N., Pindor, B., Strauss, M. A., Richards, G. T., Hennawi, J. F., Turner, E. L., Lupton, R. H., Schneider, D. P., Fukugita, M., and Brinkmann, J., 2006: *The Sloan Digital Sky Survey Quasar Lens Search. I. Candidate Selection Algorithm.* AJ, 132, 999

Oguri, M., Inada, N., Strauss, M. A., Kochanek, C. S., Richards, G. T., Schneider, D. P., Becker, R. H., Fukugita, M., Gregg, M. D., Hall, P. B., Hennawi, J. F., Johnston, D. E., Kayo, I., Keeton, C. R., Pindor, B., Shin, M.-S., Turner, E. L., White, R. L., York, D. G., Anderson, S. F., Bahcall, N. A., Brunner, R. J., Burles, S., Castander, F. J., Chiu, K., Clocchiatti, A., Eisenstein, D., Frieman, J. A., Kawano, Y., Lupton, R., Morokuma, T., Rix, H.-W., Scranton, R., and Sheldon, E. S., 2008: *The Sloan Digital Sky Survey Quasar Lens Search. III. Constraints on Dark Energy from the Third Data Release Quasar Lens Catalog.* AJ, 135, 512

Paczynski, B., 1986a: *Gravitational microlensing at large optical depth.* ApJ, 301, 503

Paczynski, B., 1986b: *Gravitational microlensing by the galactic halo.* ApJ, 304, 1

Perlmutter, S., Aldering, G., Goldhaber, G., Knop, R. A., Nugent, P., Castro, P. G., Deustua, S., Fabbro, S., Goobar, A., Groom, D. E., Hook, I. M., Kim, A. G., Kim, M. Y., Lee, J. C., Nunes, N. J., Pain, R., Pennypacker, C. R., Quimby, R., Lidman, C., Ellis, R. S., Irwin, M., McMahon, R. G., Ruiz-Lapuente, P., Walton, N., Schaefer, B., Boyle, B. J., Filippenko, A. V., Matheson, T., Fruchter, A. S., Panagia, N., Newberg, H. J. M., Couch, W. J., and The Supernova Cosmology Project, 1999: *Measurements of Omega and Lambda from 42 High-Redshift Supernovae.* ApJ, 517, 565

Power, C., Navarro, J. F., Jenkins, A., Frenk, C. S., White, S. D. M., Springel, V., Stadel, J., and Quinn, T., 2003: *The inner structure of ΛCDM haloes - I. A numerical convergence study.* MNRAS, 338, 14

Puchwein, E., Bartelmann, M., Dolag, K., and Meneghetti, M., 2005: *The impact of gas physics on strong cluster lensing.* A&A, 442, 405

Refsdal, S., 1964a: *On the possibility of determining Hubble's parameter and the masses of galaxies from the gravitational lens effect.* MNRAS, 128, 307

Refsdal, S., 1964b: *The gravitational lens effect.* MNRAS, 128, 295

Richards, G. T., Croom, S. M., Anderson, S. F., Bland-Hawthorn, J., Boyle, B. J., De Propris, R., Drinkwater, M. J., Fan, X., Gunn, J. E., Ivezić, Ž., Jester, S., Loveday, J., Meiksin, A., Miller, L., Myers, A., Nichol, R. C., Outram, P. J., Pimbblet, K. A., Roseboom, I. G., Ross, N., Schneider, D. P., Shanks, T., Sharp, R. G., Stoughton, C., Strauss, M. A., Szalay, A. S., Vanden Berk, D. E., and York, D. G., 2005: *The 2dF-SDSS LRG and QSO (2SLAQ) Survey: the $z < 2.1$ quasar luminosity function from 5645 quasars to $g = 21.85$.* MNRAS, 360, 839

Richards, G. T., Strauss, M. A., Fan, X., Hall, P. B., Jester, S., Schneider, D. P., Vanden Berk, D. E., Stoughton, C., Anderson, S. F., Brunner, R. J., Gray, J., Gunn, J. E., Ivezić, Ž., Kirkland, M. K., Knapp, G. R., Loveday, J., Meiksin, A., Pope, A., Szalay, A. S., Thakar, A. R., Yanny, B., York, D. G., Barentine, J. C., Brewington, H. J., Brinkmann, J., Fukugita, M., Harvanek, M., Kent, S. M., Kleinman, S. J., Krzesiński, J., Long, D. C., Lupton, R. H., Nash, T., Neilsen, E. H., Jr., Nitta, A., Schlegel, D. J., and Snedden, S. A., 2006: *The Sloan Digital Sky Survey Quasar Survey: Quasar Luminosity Function from Data Release 3.* AJ, 131, 2766

Riess, A. G., Filippenko, A. V., Challis, P., Clocchiatti, A., Diercks, A., Garnavich, P. M., Gilliland, R. L., Hogan, C. J., Jha, S., Kirshner, R. P., Leibundgut, B., Phillips, M. M., Reiss, D., Schmidt, B. P., Schommer, R. A., Smith, R. C., Spyromilio, J., Stubbs, C., Suntzeff, N. B., and Tonry, J., 1998: *Observational Evidence from Supernovae for an Accelerating Universe and a Cosmological Constant.* AJ, 116, 1009

Riess, A. G., Strolger, L.-G., Tonry, J., Casertano, S., Ferguson, H. C., Mobasher, B., Challis, P., Filippenko, A. V., Jha, S., Li, W., Chornock, R., Kirshner, R. P., Leibundgut, B., Dickinson, M., Livio, M., Giavalisco, M., Steidel, C. C., Benítez, T., and Tsvetanov, Z., 2004: *Type Ia Supernova Discoveries at $z > 1$ from the Hubble Space Telescope: Evidence for Past Deceleration and Constraints on Dark Energy Evolution.* ApJ, 607, 665

Rozo, E., Nagai, D., Keeton, C., and Kravtsov, A., 2006: *The Impact of Baryonic Cooling on Giant Arc Abundances.* ArXiv Astrophysics e-prints, astro-ph/0609621

Schneider, P., 2006a: *Part 1: Introduction to gravitational lensing and cosmology.* In: Meylan, G., Jetzer, P., North, P., Schneider, P., Kochanek, C. S., and Wambsganss, J. (eds.), *Saas-Fee Advanced Course 33: Gravitational Lensing: Strong, Weak and Micro*, pp. 1–89. Springer, Berlin

Schneider, P., 2006b: *Part 3: Weak gravitational lensing.* In: Meylan, G., Jetzer, P., North, P., Schneider, P., Kochanek, C. S., and Wambsganss, J. (eds.), *Saas-Fee Advanced Course 33: Gravitational Lensing: Strong, Weak and Micro*, pp. 269–451. Springer, Berlin

Schneider, P. and Weiss, A., 1987: *A gravitational lens origin for AGN-variability? Consequences of micro-lensing.* A&A, 171, 49

Schneider, P., Ehlers, J., and Falco, E. E., 1992: *Gravitational Lenses.* Springer-Verlag, Berlin Heidelberg New York

Schneider, P., Kochanek, C., and Wambsganss, J., 2006: *Gravitational Lensing: Strong, Weak and Micro.* Saas-Fee Advanced Course 33. Springer, Berlin

Seitz, S. and Schneider, P., 1992: *Two theorems in multiple deflection gravitational lens theory.* A&A, 265, 1

Seitz, S., Schneider, P., and Ehlers, J., 1994: *Light propagation in arbitrary spacetimes and the gravitational lens approximation.* Classical and Quantum Gravity, 11, 2345

Seljak, U., Makarov, A., Mandelbaum, R., Hirata, C. M., Padmanabhan, N., McDonald, P., Blanton, M. R., Tegmark, M., Bahcall, N. A., and Brinkmann, J., 2005: *SDSS galaxy bias from halo mass-bias relation and its cosmological implications.* Phys. Rev. D, 71(4), 043511

Semboloni, E., Mellier, Y., van Waerbeke, L., Hoekstra, H., Tereno, I., Benabed, K., Gwyn, S. D. J., Fu, L., Hudson, M. J., Maoli, R., and Parker, L. C., 2006: *Cosmic shear analysis with CFHTLS deep data.* A&A, 452, 51

Shen, B. S., Mo, H. J., White, S. D. M., Blanton, M. R., Kauffmann, G., Voges, W., Brinkmann, J., and Csabai, I., 2007: *Erratum: The size distribution of galaxies in the Sloan Digital Sky Survey.* MNRAS, 379, 400

Shen, S., Mo, H. J., White, S. D. M., Blanton, M. R., Kauffmann, G., Voges, W., Brinkmann, J., and Csabai, I., 2003: *The size distribution of galaxies in the Sloan Digital Sky Survey.* MNRAS, 343, 978

Simon, P., Hetterscheidt, M., Schirmer, M., Erben, T., Schneider, P., Wolf, C., and Meisenheimer, K., 2007: *GaBoDS: The Garching-Bonn Deep Survey. VI. Probing galaxy bias using weak gravitational lensing.* A&A, 461, 861

Smail, I., Ellis, R. S., and Fitchett, M. J., 1994: *Gravitational Lensing of Distant Field Galaxies by Rich Clusters - Part One - Faint Galaxy Redshift Distributions.* MNRAS, 270, 245

Soldner, J. G., 1801: *Über die Ablenkung eines Lichtstrahls von seiner geradlinigen Bewegung durch die Attraktion eines Weltkörpers, an welchem er nahe vorbeigeht.* In: *Astronomisches Jahrbuch für das Jahr 1804*, p. 161. J. E. Bode (Königl. Akademie der Wissenschaften) and G. A. Lange, Berlin. (English translation in Jaki 1978)

Soucail, G., Mellier, Y., Fort, B., Mathez, G., and Hammer, F., 1987: *Further data on the blue ring-like structure in A 370.* A&A, 184, L7

Spergel, D. N., Bean, R., Doré, O., Nolta, M. R., Bennett, C. L., Dunkley, J., Hinshaw, G., Jarosik, N., Komatsu, E., Page, L., Peiris, H. V., Verde, L., Halpern, M., Hill, R. S., Kogut, A., Limon, M., Meyer, S. S., Odegard, N., Tucker, G. S., Weiland, J. L., Wollack, E., and Wright, E. L., 2007: *Three-Year Wilkinson Microwave Anisotropy Probe (WMAP) Observations: Implications for Cosmology.* ApJS, 170, 377

Springel, V., 2005: *The cosmological simulation code GADGET-2.* MNRAS, 364, 1105

Springel, V., White, S. D. M., Tormen, G., and Kauffmann, G., 2001: *Populating a cluster of galaxies - I. Results at z=0.* MNRAS, 328, 726

Springel, V., White, S. D. M., Jenkins, A., Frenk, C. S., Yoshida, N., Gao, L., Navarro, J., Thacker, R., Croton, D., Helly, J., Peacock, J. A., Cole, S., Thomas, P., Couchman, H., Evrard, A., Colberg, J., and Pearce, F., 2005: *Simulations of the formation, evolution and clustering of galaxies and quasars.* Nature, 435, 629

Springel, V., Frenk, C. S., and White, S. D. M., 2006: *The large-scale structure of the Universe.* Nature, 440, 1137

Subramanian, K., Rees, M. J., and Chitre, S. M., 1987: *Gravitational lensing by dark galactic haloes.* MNRAS, 224, 283

Sugai, H., Kawai, A., Shimono, A., Hattori, T., Kosugi, G., Kashikawa, N., Inoue, K. T., and Chiba, M., 2007: *Integral Field Spectroscopy of the Quadruply Lensed Quasar 1RXS J1131-1231: New Light on Lens Substructures.* ApJ, 660, 1016

Thorpe, E. et al. (eds.), 1921: *The Scientific Papers of the Honourable Henry Cavendish, F.R.S., Vol. II: Chemical and Dynamical.* Cambridge Univerity Press, London

Tisserand, P., Le Guillou, L., Afonso, C., Albert, J. N., Andersen, J., Ansari, R., Aubourg, É., Bareyre, P., Beaulieu, J. P., Charlot, X., Coutures, C., Ferlet, R., Fouqué, P., Glicenstein, J. F., Goldman, B., Gould, A., Graff, D., Gros, M., Haissinski, J., Hamadache, C., de Kat, J., Lasserre, T., Lesquoy, É., Loup, C., Magneville, C., Marquette, J. B., Maurice, É., Maury, A., Milsztajn, A., Moniez, M., Palanque-Delabrouille, N., Perdereau, O., Rahal, Y. R., Rich, J., Spiro, M., Vidal-Madjar, A., Vigroux, L., Zylberajch, S., and The EROS-2 Collaboration, 2007: *Limits on the Macho content of the Galactic Halo from the EROS-2 Survey of the Magellanic Clouds.* A&A, 469, 387

Trujillo, I., Förster Schreiber, N. M., Rudnick, G., Barden, M., Franx, M., Rix, H.-W., Caldwell, J. A. R., McIntosh, D. H., Toft, S., Häussler, B., Zirm, A., van Dokkum, P. G., Labbé, I., Moorwood, A., Röttgering, H., van der Wel, A., van der Werf, P., and van Starkenburg, L., 2006: *The Size Evolution of Galaxies since z* 3*: Combining SDSS, GEMS, and FIRES.* ApJ, 650, 18

Trujillo, I., Conselice, C. J., Bundy, K., Cooper, M. C., Eisenhardt, P., and Ellis, R. S., 2007: *Strong size evolution of the most massive galaxies since* $z \sim 2$. MNRAS, 382, 109

Turner, E. L., Ostriker, J. P., and Gott, J. R., III, 1984: *The statistics of gravitational lenses - The distributions of image angular separations and lens redshifts.* ApJ, 284, 1

Tyson, J. A., Wenk, R. A., and Valdes, F., 1990: *Detection of systematic gravitational lens galaxy image alignments - Mapping dark matter in galaxy clusters.* ApJ, 349, L1

Udalski, A., Jaroszyński, M., Paczyński, B., Kubiak, M., Szymański, M. K., Soszyński, I., Pietrzyński, G., Ulaczyk, K., Szewczyk, O., Wyrzykowski, Ł., Christie, G. W., DePoy, D. L., Dong, S., Gal-Yam, A., Gaudi, B. S., Gould, A., Han, C., Lépine, S., McCormick, J., Park, B.-G., Pogge, R. W., Bennett, D. P., Bond, I. A., Muraki, Y., Tristram, P. J., Yock, P. C. M., Beaulieu, J.-P., Bramich, D. M., Dieters, S. W., Greenhill, J., Hill, K., Horne, K., and Kubas, D., 2005: *A Jovian-Mass Planet in Microlensing Event OGLE-2005-BLG-071.* ApJ, 628, L109

Valageas, P., 2000: *Weak gravitational lensing effects on the determination of* Ω_m *and* Ω_Λ *from SNeIa.* A&A, 354, 767

Vale, C. and White, M., 2003: *Simulating Weak Lensing by Large-Scale Structure.* ApJ, 592, 699

van Waerbeke, L., 2000: *Noise properties of gravitational lens mass reconstruction.* MNRAS, 313, 524

Van Waerbeke, L., Mellier, Y., Erben, T., Cuillandre, J. C., Bernardeau, F., Maoli, R., Bertin, E., Mc Cracken, H. J., Le Fèvre, O., Fort, B., Dantel-Fort, M., Jain, B., and

Schneider, P., 2000: *Detection of correlated galaxy ellipticities from CFHT data: first evidence for gravitational lensing by large-scale structures.* A&A, 358, 30

Vanderriest, C., Schneider, J., Herpe, G., Chevreton, M., Moles, M., and Wlerick, G., 1989: *The value of the time delay Delta t(A, B) for the 'double' quasar 0957+561 from optical photometric monitoring.* A&A, 215, 1

Vietri, M. and Ostriker, J. P., 1983: *The statistics of gravitational lenses - Appaarent changes in the luminosity function of distant sources due to passage of light through a single galaxy.* ApJ, 267, 488

Voit, G. M., 2005: *Tracing cosmic evolution with clusters of galaxies.* Reviews of Modern Physics, 77, 207

Walsh, D., Carswell, R. F., and Weymann, R. J., 1979: *0957 + 561 A, B - Twin quasistellar objects or gravitational lens.* Nature, 279, 381

Wambsganss, J., Cen, R., Xu, G., and Ostriker, J. P., 1997: *Effects of Weak Gravitational Lensing from Large-Scale Structure of the Determination of Q 0.* ApJ, 475, L81

Wambsganss, J., Bode, P., and Ostriker, J. P., 2004: *Giant Arc Statistics in Concord with a Concordance Lambda Cold Dark Matter Universe.* ApJ, 606, L93

Wambsganss, J., Bode, P., and Ostriker, J. P., 2005: *Gravitational Lensing in a Concordance ΛCDM Universe: The Importance of Secondary Matter along the Line of Sight.* ApJ, 635, L1

Wambsganss, J., Ostriker, J. P., and Bode, P., 2008: *The Effect of Baryon Cooling on the Statistics of Giant Arcs and Multiple Quasars.* ApJ, 676, 753

Wang, Y., 2005: *Observational signatures of the weak lensing magnification of supernovae.* Journal of Cosmology and Astroparticle Physics, 2005(03), 005

Wang, Y. and Turner, E. L., 1997: *Caustics, critical curves and cross-sections for gravitational lensing by disc galaxies.* MNRAS, 292, 863

Weymann, R. J., Latham, D., Roger, J., Angel, P., Green, R. F., Liebert, J. W., Turnshek, D. A., Turnshek, D. E., and Tyson, J. A., 1980: *The triple QSO PG1115+08 - Another probable gravitational lens.* Nature, 285, 641

Willis, J. P., Hewett, P. C., Warren, S. J., Dye, S., and Maddox, N., 2006: *The OLS-lens survey: the discovery of five new galaxy-galaxy strong lenses from the SDSS.* MNRAS, 369, 1521

Wittman, D. M., Tyson, J. A., Kirkman, D., Dell'Antonio, I., and Bernstein, G., 2000: *Detection of weak gravitational lensing distortions of distant galaxies by cosmic dark matter at large scales.* Nature, 405, 143

Wu, J. M. and Chiueh, T., 2006: *Strong Lensing on High-Redshift Galaxies.* ApJ, 639, 695

Xu, G., 1995: *A New Parallel N-Body Gravity Solver: TPM.* ApJS, 98, 355

Young, P., 1981: *Q0957+561 - Effects of random stars on the gravitational lens.* ApJ, 244, 756

Zahn, O. and Zaldarriaga, M., 2006: *Lensing Reconstruction Using Redshifted 21 Centimeter Fluctuations.* ApJ, 653, 922

Zaldarriaga, M., Furlanetto, S. R., and Hernquist, L., 2004: *21 Centimeter Fluctuations from Cosmic Gas at High Redshifts.* ApJ, 608, 622

Zaritsky, D. and Gonzalez, A. H., 2003: *On the Incidence of Strong Gravitational Lensing by Clusters in the Las Campanas Distant Cluster Survey.* ApJ, 584, 691

Zel'Dovich, Y. B., 1964a: *Observations in a Universe Homogeneous in the Mean.* AZh, 41, 19. (English translation in Zel'Dovich 1964b)

Zel'Dovich, Y. B., 1964b: *Observations in a Universe Homogeneous in the Mean.* Soviet Astronomy, 8, 13. (English translation of Zel'Dovich 1964a)

Zwicky, F., 1933: *Die Rotverschiebung von extragalaktischen Nebeln.* Helvetica Physica Acta, 6, 110

Zwicky, F., 1937a: *Nebulae as gravitational lenses.* Phys. Rev., 51(4), 290

Zwicky, F., 1937b: *On the probability of detecting nebulae which act as gravitational lenses.* Phys. Rev., 51(8), 679